

NUREG/CR-2866

LA-9478-MS

Los Alamos National Laboratory is operated by the University of California for the United States Department of Energy under contract W-7405-ENG-36

*A Simulant-Material Experimental Investigation
of Flow Dynamics in the
CRBR Upper Core Structure*

Los Alamos Los Alamos National Laboratory
Los Alamos, New Mexico 87545

8212130157 821130
PDR ADECK 85000537
A PDR

An Affirmative Action/Equal Opportunity Employer

NOTICE

This report was prepared as an account of work sponsored by an agency of the United States Government. Neither the United States Government nor any agency thereof, or any of their employees, makes any warranty, expressed or implied, or assumes any legal liability or responsibility for any third party's use, or the results of such use, of any information, apparatus, product or process disclosed in this report, or represents that its use by such third party would not infringe privately owned rights.

NUREG/CR-2866
LA-9478-MS

R7

A Simulant-Material Experimental Investigation of Flow Dynamics in the CRBR Upper Core Structure

D. Wilhelm*
V. S. Starkovich**
E. J. Chapyak

Manuscript submitted: July 1982
Date published: September 1982

Prepared for
Division of Accident Evaluation
Office of Nuclear Regulatory Research
US Nuclear Regulatory Commission
Washington, DC 20555

NRC FIN No. A7235

*Guest Scientist. Kernforschungszentrum Karlsruhe, INR, Postfach 3640, 7500 Karlsruhe,
FEDERAL REPUBLIC OF GERMANY.

**Boeing Aerospace Company, P. O. Box 3999, MS 42-25, Seattle, WA 98124.

Los Alamos Los Alamos National Laboratory
Los Alamos, New Mexico 87545

CONTENTS

TABLES.....	vi
FIGURES.....	vii
ABSTRACT.....	1
I. INTRODUCTION.....	1
II. SCALING ANALYSIS.....	4
III. EXPERIMENTAL APPARATUS.....	14
IV. EXPERIMENTAL PROCEDURE.....	20
V. ANALYSIS.....	25
A. Introduction.....	25
B. Helium Tests.....	26
C. Propanol Tests.....	31
VI. CONCLUSIONS.....	72
VII. ACKNOWLEDGEMENTS.....	73
REFERENCES.....	73

TABLES

I.	BASIC SCALING PARAMETERS.....	7
II.	PROTOTYPIC AND SIMULANT MATERIAL PARAMETERS.....	12
III.	DESCRIPTION OF COMPONENTS.....	16
IV.	USD EXPERIMENT TEST MATRIX.....	25
V.	PRESSURE DROP AND IMPACT TIME RESULTS.....	64
VI.	MAIN PARAMETER VARIATIONS OF THE PROPANOL TESTS.....	67

FIGURES

1. Schematic of the USD experiment.....	15
2. Overview of the USD experimental apparatus.....	18
3. USD experimental hardware showing sections A, B, C1, and D2.....	19
4. Block diagram of electronics for the USD experiment.....	21
5. The test section C2, a 1:2,5 scaled-down CRBR upper core structure subassembly with 217 wire-wrapped, stainless steel-pins.....	22
6. The test section C2 after assembly.....	23
7. Test 10, lower base pressure.....	28
8. Test 10, spacer pressure.....	29
9. Test 10, lower UCS pressure.....	29
10. Test 10, upper UCS pressure.....	30
11. Test 10, piston displacement.....	30
12. Test 12, moving piston.....	32
13. Test 12, piston stuck in lowest position.....	33
14. Test 12, piston stuck in highest position.....	33
15. Test 12, lower base pressure.....	34
16. Test 12, spacer pressure.....	34
17. Test 12, lower UCS pressure.....	35
18. Test 12, middle UCS pressure.....	35
19. Test 12, upper UCS pressure.....	36
20. Test 12, piston displacement.....	36
21. Test 13, lower base pressure..	37
22. Test 13, lower base pressure.....	37
23. Test 13, lower UCS pressure.....	38
24. Test 13, middle UCS pressure.....	38
25. Test 13, upper UCS pressure.....	39
26. Test 13, piston displacement.....	39
27. Test 12-Test 13, lower UCS pressure.....	40
28. Test 12-Test 13, middle UCS pressure.....	40
29. Test 12-Test 13, upper UCS pressure.....	41
30. Test 14, lower base pressure.....	41
31. Test 14, upper base pressure.....	42
32. Test 14, lower UCS pressure.....	42
33. Test 14, upper UCS pressure.....	43

34.	Test 14, piston displacement.....	43
35.	Test 16, lower base pressure.....	44
36.	Test 16, upper base pressure.....	44
37.	Test 16, spacer pressure.....	45
38.	Test 16, lower UCS pressure.....	45
39.	Test 16, upper UCS pressure.....	46
40.	Test 16, piston displacement.....	46
41.	Test 17, lower base pressure.....	47
42.	Test 17, upper base pressure.....	47
43.	Test 17, spacer pressure.....	48
44.	Test 17, lower UCS pressure.....	48
45.	Test 17, middle UCS pressure.....	49
46.	Test 17, upper UCS pressure.....	49
47.	Test 17, piston displacement.....	49
48.	Test 18, lower base pressure.....	50
49.	Test 18, upper base pressure.....	51
50.	Test 18, spacer pressure.....	51
51.	Test 18, lower UCS pressure.....	52
52.	Test 18, upper UCS pressure.....	52
53.	Test 18, upper UCS pressure.....	53
54.	Test 18, piston displacement.....	53
55.	Test 19, lower base pressure.....	54
56.	Test 19, upper base pressure.....	54
57.	Test 19, spacer pressure.....	55
58.	Test 19, lower UCS pressure.....	55
59.	Test 19, upper UCS pressure.....	56
60.	Test 19, piston displacement.....	56
61.	Test 20, lower base pressure.....	57
62.	Test 20, upper base pressure.....	57
63.	Test 20, spacer pressure.....	58
64.	Test 20, lower UCS pressure.....	58
65.	Test 20, upper UCS pressure.....	59
66.	Test 20, upper UCS pressure.....	59
67.	Test 20, piston displacement.....	60
68.	Upper UCS pressure as a function of piston displacement volume.....	70
69.	USD energy-volume relationships.....	71

A SIMULANT-MATERIAL EXPERIMENTAL INVESTIGATION OF
FLOW DYNAMICS IN THE CRBR UPPER CORE STRUCTURE

by

D. Wilhelm, V. S. Starkovich, and E. J. Chapyak

ABSTRACT

The results of a simulant-material experimental investigation of flow dynamics in the Clinch River Breeder Reactor (CRBR) Upper Core Structure are described. The methodology used to design the experimental apparatus and select test conditions is detailed. Numerous comparisons between experimental data and SIMMER-II Code calculations are presented with both advantages and limitations of the SIMMER modeling features identified.

I. INTRODUCTION

A key feature of liquid-metal fast breeder reactor (LMFBR) hypothetical core disruptive accidents (HCDAs) is the extreme thermophysical environment generated during the postulated accident sequence.¹ Because these harsh environments usually can be generated only in-pile at considerable expense, experiments using simulant materials at modest temperatures and pressures often are used to model accident progressions of interest.^{2,3} The purpose of the Upper Structure Dynamics (USD) experiment is to obtain data that are representative of certain key phenomena in the postdisassembly energetics phase of an HCDA and to compare these experimental results to SIMMER-II calculations with the aim of identifying modeling deficiencies. With the insights obtained from this comparison, we believe that an extrapolation to prototypic conditions can be made with some confidence.

The postdisassembly expansion phase of an HCDA follows neutronic shutdown and begins with a highly disrupted active core region. During this phase, the core is supposed to consist of a multicomponent, multiphase fluid of nearly uniform density in contact with still-intact radial blanket subassemblies and stubs of axial blanket subassemblies. In SIMMER-II, the initial conditions for this type of unprotected loss-of-flow accident usually are specified by pressure and temperature distributions in the core region.

The accident sequence begins with the initial propagation of pressures and intense, rate-controlled exchange processes within the volume of the core. It is probable that, during the expansion, a high-dens. zone is established that is symmetric about the core center. The compressed fluid of the core zone enters the lower end of the upper axial blanket because of the relatively low hydraulic resistance at that point. The leading edge of the expanding source appears as a multicomponent flashing fluid when viewed from the Upper Core Structure (UCS).^{4,5} Above the leading edge, a transient, multicomponent, two-phase flow will pass through the UCS. Because of the large surfaces adjacent to the flow, considerable heat and momentum can be exchanged; condensation, stratification, entrainment, and de-entrainment also can occur, resulting in the ejection of a substantially altered fluid into the liquid sodium pool than that present in the UCS. The rate of this flow determines the build-up of the pressure at the lower interface of the sodium pool because it governs the rate of evaporation of sodium from the pool. Thus, the effective "source" for the sodium pool expansion is the sodium vapor generated at the lower pool interface due to energy transfer from the ejected core debris. The sodium pool is then accelerated into the cover gas plenum where a portion of its kinetic energy is eventually transferred to the internal tank structures and to the main vessel.

While the above scenario should remain the base case for the present experimental program, recent studies⁶ have indicated that the expansion following a prompt burst that occurs at the end of the transition phase may lead to substantially different initial conditions. The transition phase is characterized by a rather mild disintegration of the core leading to a complicated fluid flow of partly liquefied and vaporized core materials within the available volume. It is confined to the lower end of the core by completely plugged subassemblies. During the transition phase, density

variations of the fluid flow may lead to recompaction of fissile material and, hence, to reactivity insertions. Ultimately, a prompt-critical configuration will result in an energetic expansion of the core material into the UCS. Although the flow channels on the UCS may be blocked to some degree before the prompt burst, large uncertainties still remain concerning the nature of these blockages.

Simplified simulation experiments of the vessel energetics problem have been conducted at both SRI International² and Purdue University,³ where a single two-phase component (usually water) is allowed to flash through a simulated UCS. However, the selection of simulant materials and operating conditions in these experiments was made largely without regard for consideration of scaling requirements.

The scaling requirements derived from enforcing similitude, together with the degree to which selected simulant materials actually meet these requirements for the postdisassembly energetics problem, are presented in Ref. 7 (see also Sec. II of this report). With primary emphasis placed on the vaporization characteristics of uranium dioxide and steel, the best simulants identified to date are an n-propyl alcohol, ammonia, and helium system, which is representative of uranium dioxide volatility near the high end of its uncertainty band, and an ethylene glycol, ammonia, and helium system, which is representative of uranium dioxide volatility near the low end of its uncertainty band. These are the main simulants employed in the USD experiment.

The SIMMER-II verification program of Clinch River Breeder Reactor (CRBR)-related accidents has resulted in a number of publications, including experimental work.⁸⁻¹¹ Initial SIMMER-II calculations indicated that there were a number of expansion-phase physical phenomena that were not well understood and that these phenomena could have a major effect on the accuracy and conservativeness of the energetics calculations.¹² For example, while the large throttling effect of the UCS may retain so much fissile material in the core that a recriticality might be possible under some circumstances, the increase of ejected core material into the sodium pool leads to higher driving pressure differences. It was realized¹³ that the following uncertainties had to be investigated:

1. the nature and effect of multicomponent two-phase flow in bundle geometry (ignoring the small amount of still-solid particles in the fluid flow);
2. the dynamics of vaporization in bundle geometry;
3. the liquid-droplet entrainment rate and, eventually, dynamics of liquid films and droplet size; and
4. the dynamics of ablating walls.

The USD experiment is designed to provide data that will quantify some of these uncertainties.* For the SIMMER analysis part of the USD program, it is clear that the influence of the following code input parameters should be ascertained:

1. parameters for defining the heat-transfer coefficients and condensation rates,
2. parameters for defining the friction factors,
3. orifice coefficients, and
4. parameters for defining the interfacial area between fields and components.

By comparing USD experimental results with SIMMER parametric studies, we hope to identify any important modeling deficiencies and assess the importance of mismatches between experimental and prototypic scaling parameters that unavoidably occur with actual simulation experiments.

II. SCALING ANALYSIS

The purpose of the USD experiment is to use simulant materials that are not only easy to handle but also are capable of providing relevant data on the phenomena described in Sec. I. There is no doubt that prototypic materials in a prototypic geometry would provide more straightforward insight into the

*There are at least two reasons why the current USD experiment does not attempt to model any fuel-coolant or steel-coolant thermal interaction phenomena. First, we have not been able to identify a suitable liquid sodium simulant. Second, the inclusion of a liquid steel simulant (such as ammonia) would greatly complicate the experimental program by introducing cryogenic requirements.

physical processes under consideration. Because of a substantial decrease in complexity, however, simulant experiments provide much easier access to measurements and observations.

Basic scaling requirements can be derived by considering the homogeneous part of the governing differential equation--that is, the part that remains after all approximate descriptions of exchange quantities are dropped. These exchange terms depend strongly on the models used in SIMMER and are the subject of additional scaling analyses presented later in this section. The three generic mass, momentum, and energy conservation equations for each field, simplified to a one-dimensional description, are of the form:

$$\frac{\partial}{\partial t} \rho + \frac{\partial}{\partial x} (\rho v) = 0 , \quad (1)$$

$$\frac{\partial}{\partial t} (\rho v) + \frac{\partial}{\partial x} (\rho v v) + \frac{\partial}{\partial x} P + \rho g = 0 , \quad (2)$$

and

$$\frac{\partial}{\partial t} (\rho e) + \frac{\partial}{\partial x} (\rho e v) + P \frac{\partial v}{\partial x} = 0 . \quad (3)$$

Normalization leads to the following nondimensional variables, which are represented by capital letters:

$$R = \frac{\rho h_v}{P_0}, \quad \Theta = \frac{\tau \sqrt{h_v}}{x_0}, \quad V = \frac{v}{\sqrt{h_v}}, \quad L = \frac{x}{x_0}, \quad P = \frac{p}{\rho_0 h_v}, \quad E = \frac{e}{c_v T_0} . \quad (4)$$

The evaporation enthalpy h_v has been chosen as the reducing parameter because phase transition is evidently a major phenomenon during the core expansion.¹⁴ In the mass equation [Eq. (1)] the nondimensional variables can be substituted at once. The momentum equation [Eq. (2)] is transformed into

$$\frac{\partial}{\partial \theta} (RV) + \frac{\partial}{\partial L} (RVV) + \frac{\rho_o h_v}{P_o} \frac{\partial P}{\partial L} + \frac{g^x_o R}{h_v} = 0 \quad (5)$$

The energy equation [Eq. (3)] becomes

$$\frac{\partial}{\partial \theta} (RE) + \frac{\partial}{\partial L} (REV) + \frac{\rho_o h_v^2}{P_o c_v T_o} p \frac{\partial V}{\partial L} = 0 \quad (6)$$

The three dimensionless parameters

$$A_c = \frac{\rho_o h_v}{P_o} ,$$

$$B_c = \frac{g^x_o}{h_v} , \quad (7)$$

and

$$C_c = \frac{c_v T_o}{h_v}$$

are used to set the basic scales.⁷ They also are used to select the appropriate simulant materials. This procedure allows a quick investigation of many materials because the parameters A_c and C_c are combined to yield

$$A_c C_c = \frac{\rho_o}{P_o} c_v T_o = \frac{c_v}{R_c}, \quad (8)$$

where the perfect gas law has been applied. Because the specific gas constant R_c can be expressed as the product of the universal gas constant R_u and the molecular weight, the parameter D_c can be formed, yielding

$$D_c = R_u A_c C_c = c_v m. \quad (9)$$

In Eq. (7), P_o/ρ_o has been replaced in the equation by h_v because, for a gas, $P/\rho = (1 - c_v/c_p)h$. In the case of an incompressible liquid, the last term of Eq. (6) no longer exists nor does the above proportionality of the enthalpy with P/ρ . When we know the representative quantities of A_c , B_c , and C_c for the prototypic material, we can select the values of p_o , x_o , and T_o for the experiment. Table I shows results of scaling calculations using Eqs. (7) and (9), with ρ_o and c_v being liquid-state variables.

TABLE I
BASIC SCALING PARAMETERS

Material	D_c (J/kmol·K)	$(\rho_o h_v)^{-1}$ (Pa ⁻¹)	B/h_v (m ⁻¹)	c_v/h_v (K ⁻¹)	Pressure	Length	Temperature
UO ₂	1.45 × 10 ⁵	6.41 × 10 ⁻¹¹	5.41 × 10 ⁻⁶	2.95 × 10 ⁻⁴	P_p	l_p	T_p
Propyl Alcohol	1.42 × 10 ⁵	1.60 × 10 ⁻⁹	1.26 × 10 ⁻⁵	3.04 × 10 ⁻³	0.040 P_p	0.420 l_p	0.097 T_p
Ethlene Glycol	1.47 × 10 ⁵	1.14 × 10 ⁻⁹	1.23 × 10 ⁻⁵	2.95 × 10 ⁻³	0.056 P_p	0.441 l_p	0.100 T_p

Note that, for the simulants listed, the experimental mockup has to be reduced by ~60% in linear scale relative to the prototypic geometry. For comparison, water as a simulant would need a 1:1 scale and have a $D_c = 7.53 \times 10^4$ (Ref. 7).

In SIMMER-II, Eqs. (1), (2), and (3) are extended by exchange functions. First, in the mass equation a term is added (Γ) that represents the total mass-transfer rate per unit volume. In general, this rate is a function of the evaporation process and can be written as

$$\Gamma = \frac{q}{h_V} , \quad (10)$$

where q is the heat transferred and where the Lewis number is assumed to be unity. In the momentum equation, two terms are added, one of which is again a direct function of Γ . The second term is directly proportional to

$$K = \frac{2f}{D_H} \rho |v| \Phi , \quad (11)$$

where f is the friction factor, D_H is the hydraulic diameter, and Φ is a two-phase friction multiplier.

There are other expressions for K depending upon which flow regime is considered; for example, for droplet flow, K is assumed to be a complex function of the droplet radius

$$K = K(r) , \quad (12)$$

where r is specified by a Weber number criterion. In Eq. (11), the scaling parameters D_H and ρ are already set, but the friction factor f is still a function of the Reynolds number, Re :

$$f \sim Re^{\xi} \text{ for } Re < Re_{\text{limit}} \quad (13)$$

If the Reynolds number is higher than the limit value, f is constant. The generalized energy equation contains q , which is a function of the heat transfer at solid-fluid interfaces and can be written as

$$q \sim A \frac{k}{D_H} Re^{\xi} Pr^{\epsilon} \quad (14)$$

where k is a thermal conductivity and Pr is the Prandtl number.

In case of droplets, q is indirectly proportional to the radius. In addition to q , q_{Γ} and q_k are used to describe energy transport by the mass exchange

$$q_{\Gamma} \sim \Gamma e \quad (15)$$

and viscous heating

$$q_k \sim v^2 \quad (16)$$

There are several boundary conditions between the SIMMER fields that must be met. For example, the total pressure is the sum of the partial pressures, which, for a perfect gas, becomes

$$p = \rho(\gamma-1)c_v T \quad (17)$$

and for a vapor in equilibrium with its liquid is

$$p = p^* \exp \left(-\frac{T^*}{T_V} \right) . \quad (18)$$

The energy of the liquid field is

$$e = c_{VS} T_f + h_f + c_{VL} (T - T_f) , \quad (19)$$

where T_f is the melting temperature and h_f is the latent heat of fusion.

The energy of the vapor field is

$$e = c_{VS} T_f + c_{VL} (T_V - T_f) + h_V - R_C T + c_V (T - T_V) , \quad (20)$$

where T_V is the boiling temperature and h_V is the latent heat of evaporation.

SIMMER-II requires the following correlation for the above terms:

$$R_C T = h_V \frac{T_V}{T^*} . \quad (21)$$

Additionally, SIMMER-II uses the transport theory for gases to calculate thermal conductivity k and viscosity γ . Thus,

$$k \sim \frac{\sqrt{\frac{T}{m}}}{\sigma^2 \Omega} , \quad (22)$$

and

$$\gamma \sim \frac{\sqrt{T_m}}{\sigma^2 \Omega}, \quad (23)$$

where σ and Ω are functions of the molecular weight.

All these features, beginning with Eq. (10), result in a number of dimensionless parameters (for example, Reynolds number) that will allow a comparison between the prototypic and simulant materials. The importance of these parameters differs considerably. An extensive sensitivity study¹⁴ has been performed identifying several parameters to be quite effective in changing the kinetic energy imparted to the sodium pool. Indeed, the most sensitive parameters identified in the study were those associated with the fuel-vapor-pressure representation. This fact motivated our emphasis on vapor-pressure scaling requirements for selection of the USD simulant materials. A discussion of additional scaling requirements is presented below.

Table II shows a list of 13 parameters that have been identified to compare prototypic values (subscript p) with simulant values. Following the order of the basic equations, q_H in Eq. (10) is discussed in Eq. (16). The quantity h_v already has been used as a reducing parameter; in addition, the ratio of the heat of vaporization to the heat of fusion shows how energy is distributed during transients (see Table II, parameter 1). Wherever possible, a range of uncertainty is included in the values for uranium dioxide. In Eq. (11), ρ has been used as a reducing parameter and D_H is subject to geometric scaling. According to Eq. (4), the time is scaled with $t/t_p = x/x_p \sqrt{h_{vp}/h_f}$. For the gas values (subscript 2), the velocities scale with the sonic velocities of a perfect gas. Parameter 2 of Table II shows uniform scaling for all simulants. The friction factor f of Eq. (11) is defined in Eq. (13). In Eq. (12), the Weber number partly governs the droplet flow regime and, thus, is somewhat responsible for the rate of heat and mass transfer between the phases. The simulant Weber numbers are scaled down; that is, the exchange rates are not scaled in the same way as the unit volume. Nevertheless, because the surface tension of the simulants is lower, the exchange rate density of the simulant materials is relatively high in comparison to the prototypic materials. This

TABLE II
PROTOTYPIC AND SIMULANT MATERIAL PARAMETERS

Parameter Number	Parameter	UO ₂	Na ^a	Propyl Alcohol	Ethlene Glycol	H ₂ ^a
1	h_w/h_f	6.1-6.8		9.0	4.4	
2	v	v_{p1}	v_{p2}	$0.656v_{p1}$	$0.664v_{p1}$	$0.674v_{p2}$
3	We	We_p		$0.31 We_p$	$0.21 We_p$	
4	Re_v	Re_p		$0.15 Re_p$	$0.19 Re_p$	
5	Re_L	Re_p		$0.055 Re_p$	$0.089 Re_p$	
6	$ag/h_v^{1.5}$	2.2×10^{-15}		1.2×10^{-15}	1.4×10^{-15}	
7	Pr_v	0.6		0.63	0.63	
8	Pr_L	0.9		28	15	
9	$P/(\rho R_c T)$		T_p			$0.099T_p$
10	$c_v T^*/h_v$	17.4		17.4	17.6	
11	T_f/T^*	0.051-0.057		0.026	0.044	
12	$P^*/(\rho_L h_v)$	11-128		627	38	
13	$m_{coolant}/m_{fuel}$	0.085		0.067	0.064	

^aCoolants.

comparison demonstrates the difficulty encountered in matching all scales once the geometry has been scaled properly.

As long as the geometric scaling is near unity and does not hide important physical phenomena, a comparison of simulant and prototypic performance can be conducted by examining Table II. This is especially true for the exchange phenomena between phases; and, thus, attention has to be paid to the scaling of parameter 3.

In Eq. (13), the proportionality of f with the Reynolds number Re is invalid for high Reynolds numbers (see Table II, parameters 4 and 5). For high Re , the simulant parameters are considerably scaled down. For early times during the transient and in the entrance section of the upper axial blanket, the prototypic Reynolds numbers do not differ greatly from the threshold value of 10^4 . Thus, the simulant Reynolds numbers affect the friction factors in the

sense that these are too low compared with the prototypic values. Fortunately, the dominating vapor values scale better than the liquid values. When liquid films are formed at the walls, the validity of comparisons between simulant results and prototypic results should be considered carefully. For vapor flows with Reynolds numbers higher than 6.7×10^4 , the friction factor is insensitive to the scaling of parameter 4. Additionally, the sensitivity study¹⁴ revealed no unusual importance of the friction factor. In Eq. (14), A and D_H are scaled according to the geometric scaling. Scaling requirements on thermal conductivity can be derived from the thermal diffusivity (see Table II, parameter 6), as ρ and c_v are subject to scaling requirements elsewhere [see Eq. (22)]. Parameters 7 and 8 of Table II give the Prandtl numbers for vapor and liquid. In the case of vapor, the numbers are in excellent agreement. The liquid Prandtl numbers differ considerably. In the case of liquid films on walls, the effect of this discrepancy has to be considered carefully. Equation (15) can be discussed in combination with Eqs. (10) and (19). In Eq. (16), q_k is scaled according to parameter 2 of Table II, but there is evidence that, for the assumed transient, this term is unimportant. The perfect gas equation of Eq. (17) leads to a reduction of gas temperatures once the pressures have been set by Table I. The value is consistent with Table I.

Equation (18) has been identified in the sensitivity analysis as contributing to most of the uncertainties in the kinetic energy released during the transient. This equation is described by parameters 10 and 12 of Table II. Because $T^* = h_{vm}/R_u$, we are led directly to the parameter D_c of Table I by which the appropriate simulants have been chosen. In Eqs. (19) and (20) the ratios of melting and vaporization temperatures are of major importance (see parameter 11 of Table II), whereas the other terms have been either subject to scaling already or were mentioned in Eqs. (21) or (22). Equation (21) leads back to parameter 11, which shows excellent agreement for ethylene glycol. It should be noted here, that propyl alcohol has been chosen primarily because it represents an upper bound to the vapor pressure parameters (parameter 12 of Table II) and, thus, gives a conservative estimation of this predominant value. Because of the exponential variation of the vapor pressure with the temperature in the Clausius-Clapeyron equation, the uncertainties of T^* are magnified considerably and, thus, produce a large variation in the UO_2 value of parameter 12. Ethylene glycol is well within this band of uncertainty but

represents a non-conservative simulation. Equations (22) and (23) lead to parameter 13 of Table II.

III. EXPERIMENTAL APPARATUS

A schematic of the USD experiment is shown in Fig. 1. It represents a 1/2.5 geometrically scaled subassembly, along with a similarly scaled region extending upward to the vessel head. The geometric scale factor was obtained from the same similitude considerations that were used to identify the simulant materials.⁷

Each of the labeled parts is described in Table III. Also shown in Fig. 1 is an end view of a scaled subassembly made up of a hexagonal, wire-wrapped, 217-pin array as well as an equivalent-flow-area UCS structure consisting of a 7-hole array with each hole 1.27 cm in diam. Pressure transducers and thermocouples are placed at different axial locations in the UCS to determine the pressure drop and temperature rise as a function of time. Because of their temperature sensitivity, the strain-gauge-based pressure transducers located above the rupture disk were insulated with 1-mm-thick, silicone-rubber diaphragms, capable of withstanding the high-temperature, rapidly condensing, two-phase flow. A low-pressure helium atmosphere is maintained in the UCS to simulate the presence of sodium vapor, while the movable piston represents the inertial loading of the sodium pool above the expanding, two-phase material ejected through the UCS.

A fast-acting valve or rupture disk^{*} is needed to simulate the rapid expansion of the molten core materials into the UCS. For the helium and propanol simulant tests reported in this paper, prescored, two-petal rupture disks having rupture pressures of 1.4 MPa (200 psig) were used. A rupture-disk breaking mechanism was required to achieve full petaling and to control experiment initiation for better synchronization with high-speed cameras. During the development of the breaking mechanism, approximately 40 USD tests were performed using helium and propanol to examine the performance of different designs under different operating conditions. The tests also

*Manufactured by Fike Industries, Blue Springs, Missouri.

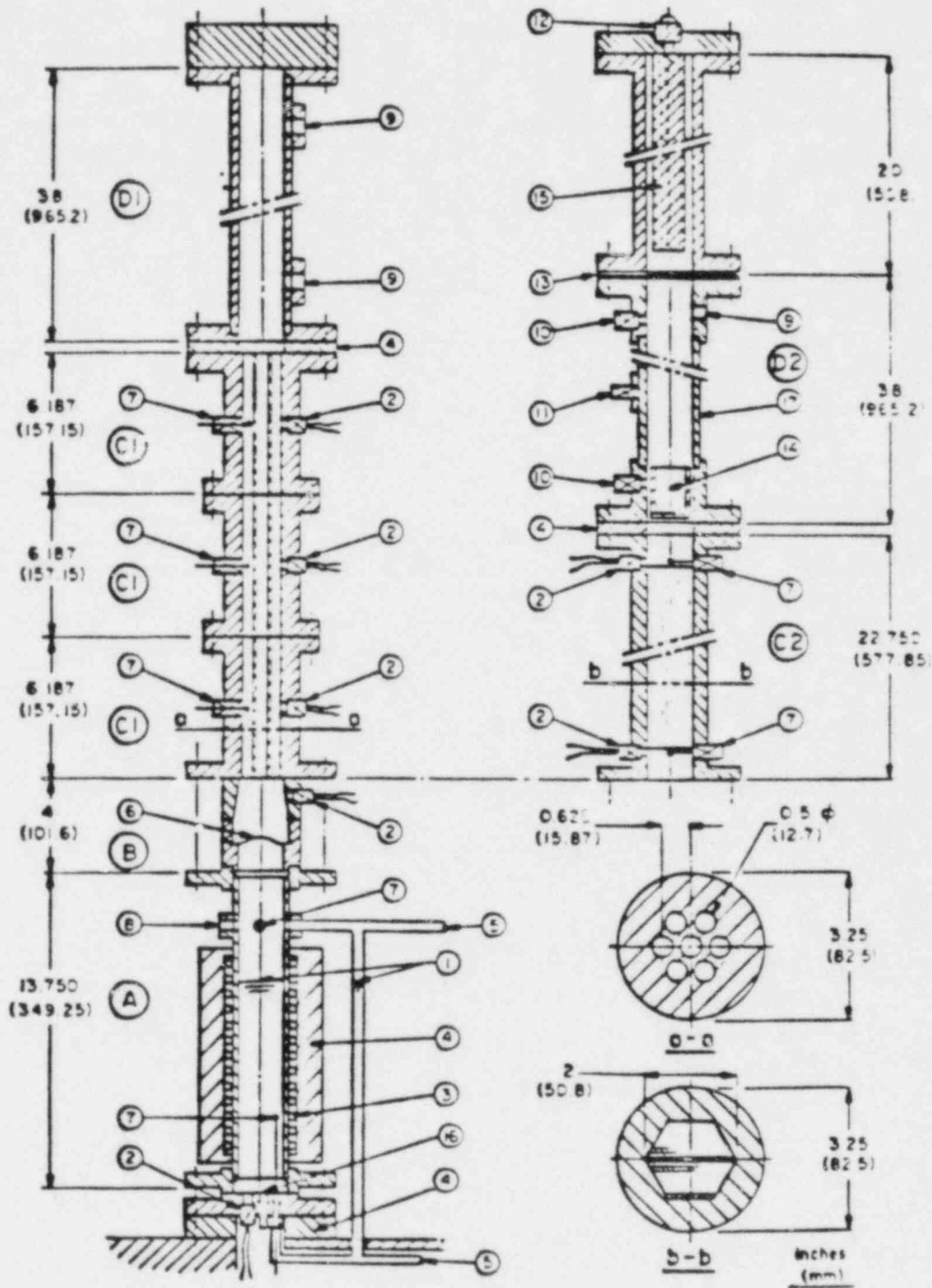


Fig. 1. Schematic of the USD experiment.

TABLE III
DESCRIPTION OF COMPONENTS
SHOWN IN FIG. 1

A	Reactor core 2" i.d.		
B	Rupture-disk holding device		
C1	Test section with 7 holes		
C2	Test section with a 217-pin bundle		
D1	View chamber for preliminary experiments 2" i.d.		
D2	View chamber and piston catcher for multiple use and movable piston 2" i.d.		
	C1 and D2 can be combined.		
1	Fluid level	9	Connection to vacuum holder
2	Pressure transducers	10	Piston speed gauge
3	Clam shell heaters	11	Movable piston speed gauge
4	Insulation	12	Pressure relief valve
5	Connection to drainage and fluid supply tank	13	Thin aluminum foil
6	Rupture disk	14	Aluminum piston
7	Thermocouple	15	Removable aluminum honeycomb
8	Connection to the pressurizer	16	Ultrasonic transducer
		17	Plexiglas tube

provided information for SIMMER-II comparisons. A discussion of these results will be presented in Sec. V.

A rupture-disk test series was necessary to determine the cause of the problems that were experienced initially. The disks would fail in one of two ways; either the disk would break at a pressure considerably less than its design pressure or the disk would fail to petal fully. The problem was particularly acute for low-pressure propanol tests. The results of the test series indicated that a two-petal, prescored, rupture disk would open properly for both helium and propanol under the desired combinations of pressures, temperatures, and void fractions if a mechanical breaking mechanism was used to initiate the rupture. Consequently, several breaking mechanisms were examined to determine their suitability for use on the USD experiment.

Our attempt to use an electrical solenoid was unsuccessful. It was unable to impart enough impulse to the disk petals to make them open properly. The most reliable method was found to be an explosively driven rod impacting the disk from below with sufficiently rapid momentum transfer to ensure full petaling. The mechanism operates by electrical initiation of approximately 300 mg of PETN high explosive. The explosion drives a mechanical rod equipped with a specially rounded fitting of the same radius-of-curvature as the rupture disk into the underside, that is, the pressure side of the rupture disk. A firing set, capable of remote actuation, is used to initiate the explosion. For tests using a high-speed camera, the camera provides the gating pulse to the firing set at a preselected film footage. The explosively driven actuator mechanism has proven to be extremely reliable and has simplified the operation of the USD experiment.

After breaking the rupture disk, the excess energy of the mechanical rod is carefully transformed into deformation energy to minimize the transmission of high-frequency oscillations to the pressure gauge located at the base of the core. Residual high frequencies that are superimposed onto this transducer signal are removed after the data have been recorded by transmitting the signal through a low-pass filter.

Figure 2 is an overall view of the experimental apparatus. As shown in Fig. 3, pressure transducers and thermocouples are placed at different axial locations along two of the 12.7-mm-diam holes or along the 217-pin scaled subassembly to determine the pressure drop and temperature rise at different axial locations along the UCS as a function of time. The portion of the hardware above the UCS represents the Upper Internal Structure (UIS) and sodium pool and is transparent to permit use of a high-speed camera to observe the flow regime emanating from the UCS.

Approximately 13 data channels and 1 timing channel are being employed on the experiment, including 5 temperature measurements, 5 pressure measurements, and 3 channels devoted to determining the velocity of the movable piston. Although the piston itself has not been instrumented, the viewing chamber through which the piston moves has been equipped with three displacement transducers positioned along its axial length to permit time-of-flight measurements on the piston. A block diagram of the electronics system for the

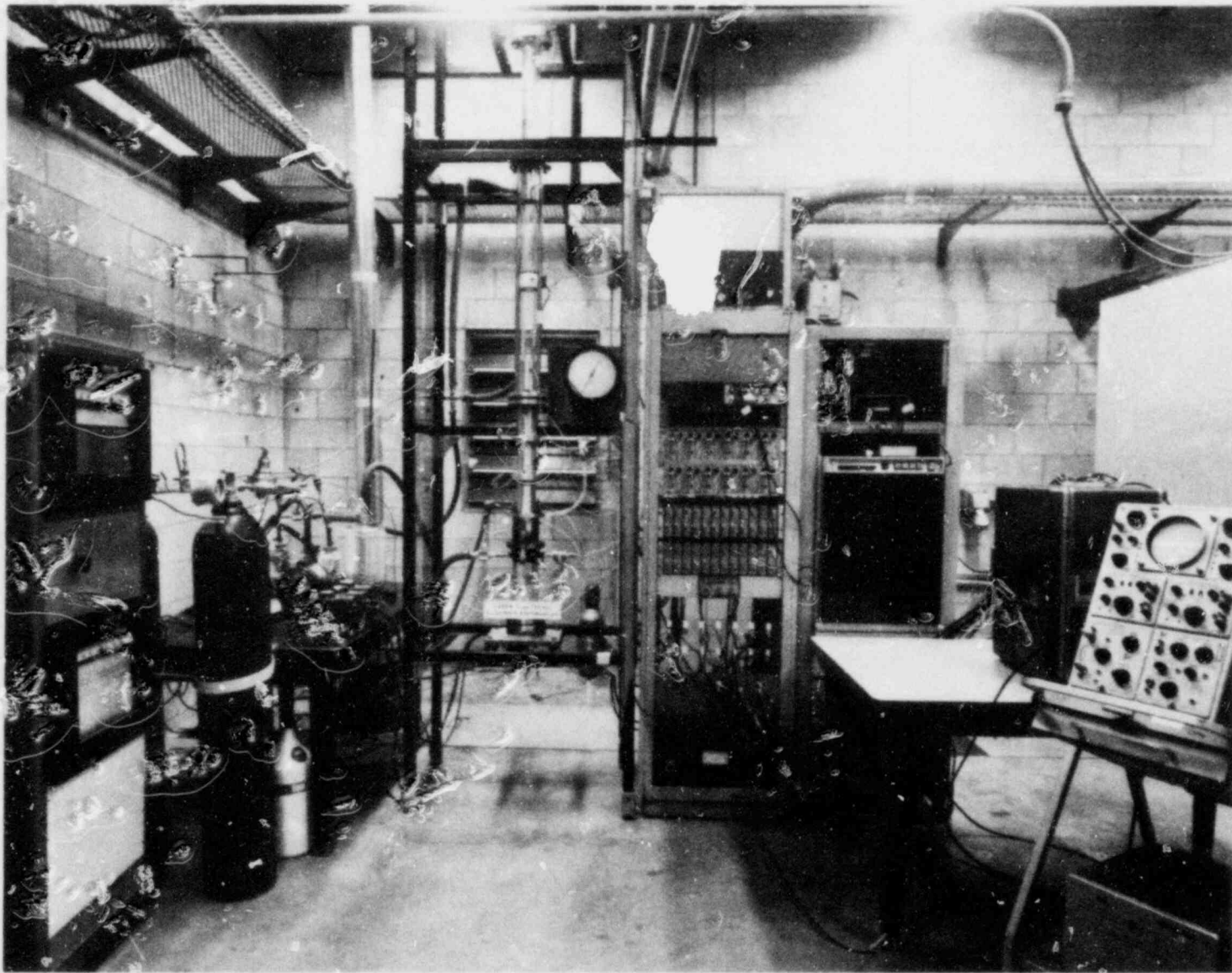


Fig. 2. Overview of the USD experimental apparatus.

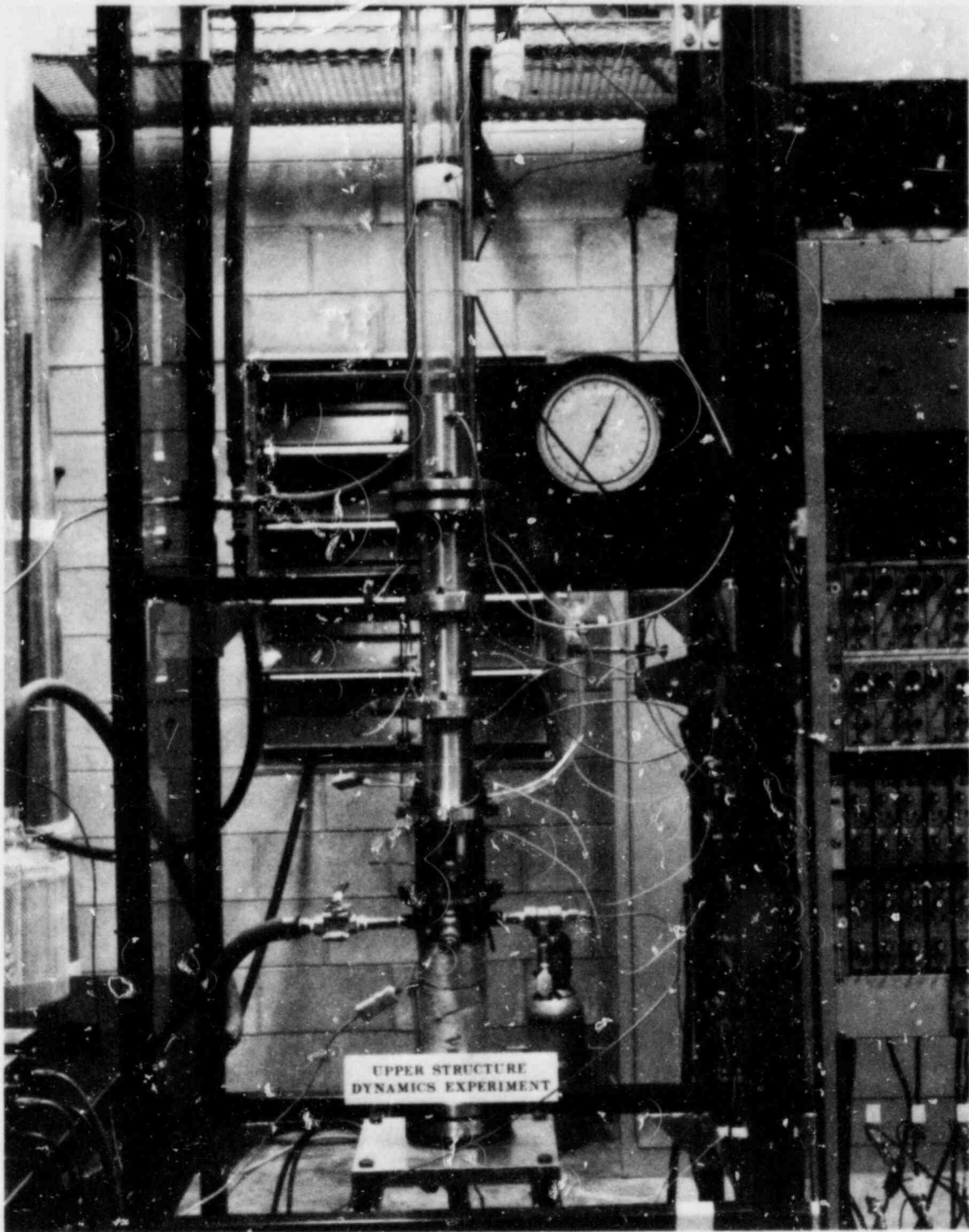


Fig. 3. USD experimental hardware showing sections A, B, C1 and D2.

USD experiment is shown in Fig. 4, with more detailed views of the scaled 217-pin subassembly shown in Figs. 5 and 6.

IV. EXPERIMENTAL PROCEDURE

Before each USD test, the pressure transducers on the core, spacers, and UCS portions of the experiment are calibrated by assembling the system without a rupture disk in place and by balancing each strain-gauge-based transducer at atmospheric pressure. The system then is pressurized with helium gas, and signal levels are recorded over the range of pressures expected to occur during the test. These levels later serve as the insert calibration signals for the pre- and posttest insert calibrations. For the helium and propanol tests described in this report, the maximum core pressures are 1.1 MPa (150 psig). Pressure transducer calibration signals of ~40 mV are used for these pressures.

After a measured amount of simulant has been introduced into the core, the six 250-W, clam-shell heaters are turned on and remain on until just before the breaking of the rupture disk. During this heat-up period, the UCS and view chamber are first evacuated to a pressure of ~50 μ m mercury, and then pressurized with helium gas to a pressure of ~20 mm mercury. The purpose of the low-pressure helium gas in the UCS is to simulate the presence of sodium vapor.

With propanol as the fuel (UO_2) simulant, it takes approximately 15 min for the core pressure to rise from atmospheric pressure to 1.1 MPa (150 psig). At approximately 5 min before the desired pressure is reached, the frequency modulated tape deck is turned on, and calibration voltages corresponding to zero and full-scale temperature and pressure readings are inserted through the amplifiers and are recorded on tape. For the pressure channels, the outputs as measured above serve as the insert calibration voltages; whereas, for the temperature channels, a tabulated output for chromel-alumel is used. All reference temperature junctions are located in an insulated box positioned nearby with the temperature provided by a Consolidated Ohmic Devices model JR114 reference junction.

Amplifier gains for the pressure and temperature channels are adjusted to produce a $\pm\sqrt{2}$ volt signal output, and the voltage control oscillator for each tape track is adjusted so that its band edge (40% frequency deviation) corresponds to this voltage. The three tracks used to record the outputs from

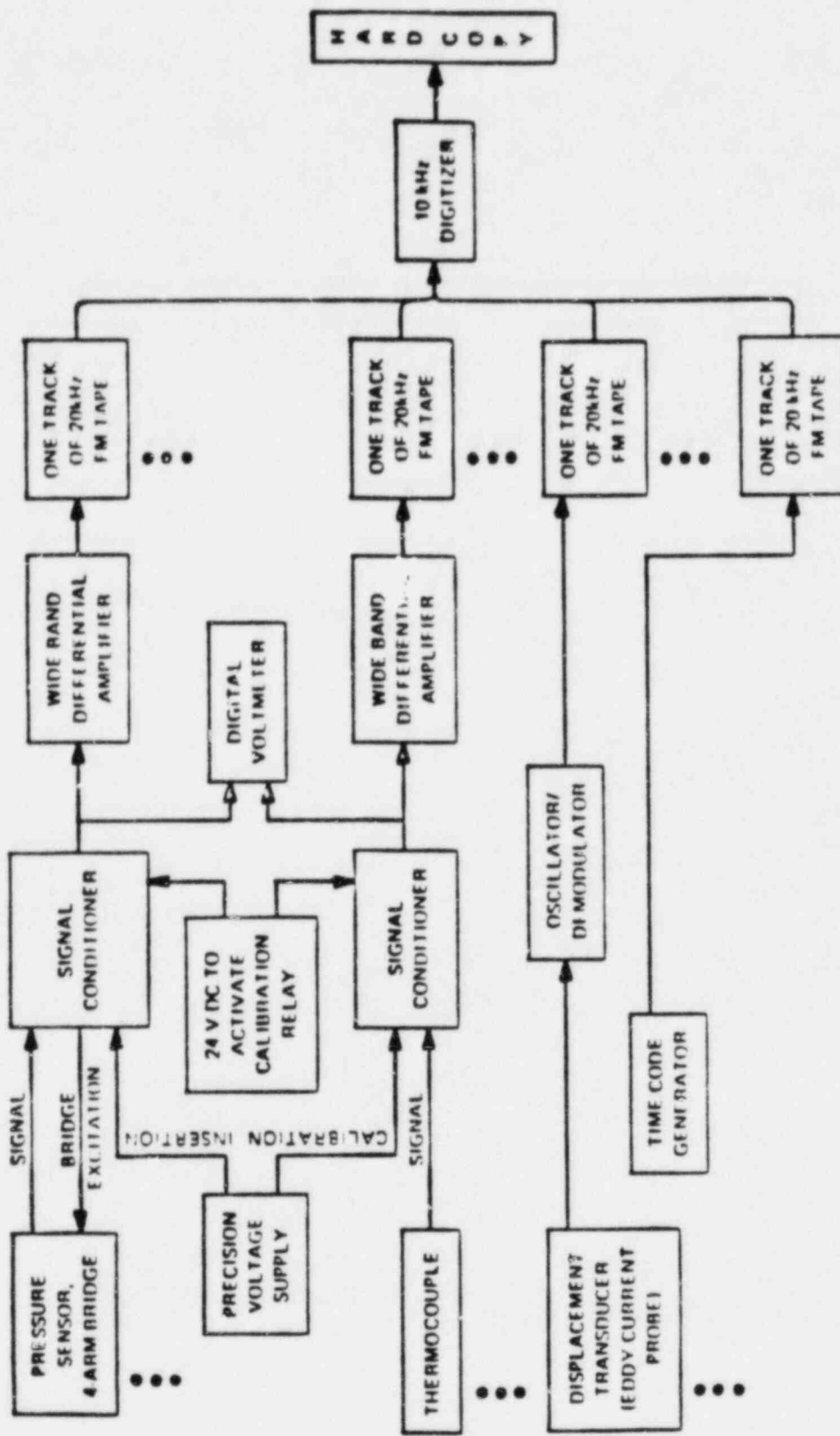


Fig. 4. Block diagram of electronics for the USD experiment.



Fig. 5. The test section C2, a 1:2,5 scaled-down CRBR upper core structure subassembly with 217 wire-wrapped, stainless steel pins. The picture shows the test section before assembly.

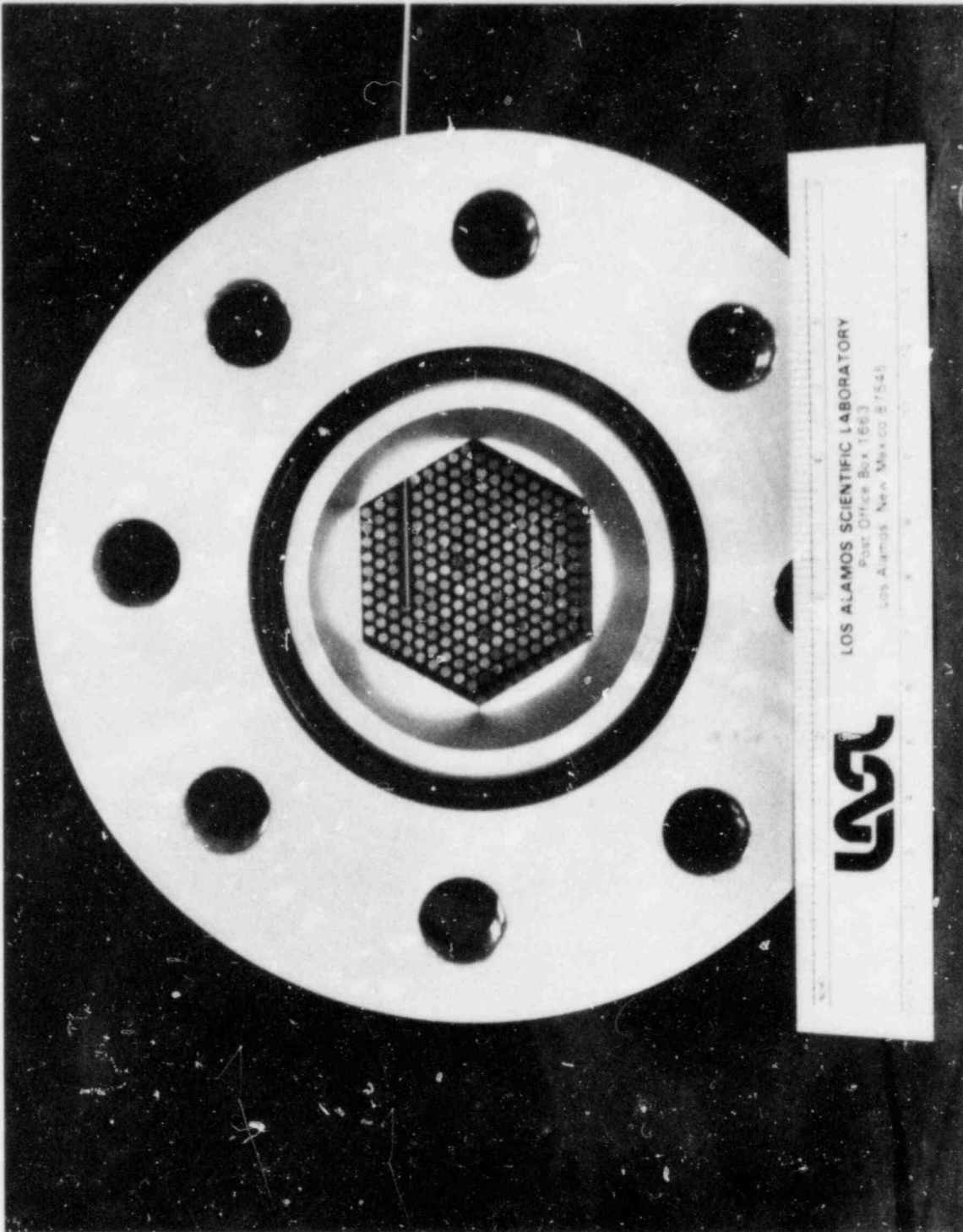


Fig. 6. The test section C2 after assembly.

the displacement transducers are adjusted to record a signal that varies between -10 and -15 Vdc. A time code is recorded on the last remaining channel. The center frequency used in these tests is 108 kHz, providing a signal recording bandwidth of 20 kHz at a tape speed of 150 cm/s. After each test, data from each tape channel are played back on an oscillograph for a "quick-look" and then are digitized and stored on the mass storage system at the Los Alamos Central Computing Facility. A software package then is used to recall the experimental results and/or SIMMER-II predictions for comparison.

The results presented in this report were obtained with a scaled subassembly made up of a hexagonal, wire-wrapped, 217-pin array as well as an equivalent-flow-area UCS structure consisting of a 7-hole array with each hole 1.27 cm in diameter. A 19-hole array with each hole 0.77 cm in diameter also was used, as was a relatively short (15-cm) transparent section that was placed between the spacer and the UCS for the tests involving high-speed photography. Table IV presents a test matrix that studied the effects of these four different UCS geometries. The test matrix was performed with propanol and helium as the simulant materials for uranium dioxide and sodium vapor, respectively.

Before the rupture-disk opening mechanism was available, two tests were performed where high-pressure helium was allowed to expand into the seven-hole array. No propanol was present so that SIMMER calculations could be tested using only a perfect gas as the expanding fluid.

Film speeds of 4000 and 8000 frames/s were used for tests 14 and 17, respectively. During the time of interest (0-40 ms), the fluid flow through the transparent section below the UCS consisted mainly of a vapor-entrained mist. Although an upper limit to the size of these fine droplets can be estimated with high-speed photography, direct measurement of the droplet size distribution was not feasible.

TABLE IV
USD EXPERIMENT TEST MATRIX

<u>Test No.</u>	<u>UCS Geometry^a</u>	<u>Initial Pressure [MPa]</u>	<u>Initial Propanol Volume (ml)</u>	<u>High-Speed Photography</u>
12	7	1.17	559	No
13	7	1.10	559	No
14	7A	1.07	559	Yes
15	217	1.10	559	No
16	19	1.10	559	No
17	7A	1.07	319	Yes
18	217	1.10	559	No
19	19	1.10	319	No
20	217	1.10	319	No

^aLEGEND

- 7: 7-hole, equivalent-area UCS; scaling requires that each hole be 1.27 cm in diam.
- 7A: Same as above, with a transparent section placed between the rupture disk and the 7-hole UCS.
- 217: Scaled, 217-pin assembly.
- 19: 19-hole, equivalent area UCS; scaling requires that each hole be 0.77 cm in diam.

V. ANALYSIS

A. Introduction

An off-the-shelf version of the SIMMER-II Code was used to perform calculations for the USD experiment. The code, which can treat two dimensions in an r - z geometry, was employed only as a one-dimensional description. The reasons for this simplification are:

1. no data are available from the experiment that specify a radial distribution,
2. the radius-to-length ratio of the experiment is small, and
3. the experimental mock-up simulates only one prototypic subassembly (SIMMER analyses usually use one radial zone for each subassembly row of the prototypic configuration).

A simple condensation and evaporation model was used, which does not account for the influence of non-condensable gases.

A major feature of the experiment is the moving piston, which is designed qualitatively to model the motion of the lower end of the sodium pool. The moving piston in effect represents a moving, rigid-wall boundary condition. A correction set is available, which can treat this feature.¹⁵ A balance of forces is calculated at the interface, the two forces being that of the inertia of an input mass and that of the driving pressure at the interface. No provision is made for frictional forces. SIMMER-II needs a pin structure for the piston track that consists of a very small volume fraction of can wall surrounding a large non-flow volume. In tracking the piston interface through the balance of forces, the code artificially disrupts the can wall, adding the non-flow volume to the flow volume and, thus, opening the channels.

B. Helium Tests

To validate the equipment and instrumentation, two tests (tests 10 and 11) were performed with pure helium expanding into a seven-hole array. The initial helium pressure in the core was 1.45×10^6 Pa for test 10 and 1.49×10^6 Pa for test 11. The response of the pressure transducers to the transient during the first two milliseconds was identical, with small deviations in frequency response and absolute value appearing later. The maximum distinguishable deviation was 0.2 ms. The middle UCS pressure of test 10 was inconsistent with the other transducers because the rubber cap was stripped off the transducer

head. The other above-core transducers had a maximum late time deviation of 2×10^4 Pa. This error is 2% of the maximum reading. We expect this degree of consistency during transients when the temperatures of the transducers do not change.

SIMMER calculations were performed for test 10 using an additional correction set to describe the dissipation of the mechanical energy to thermal energy. The off-the-shelf SIMMER version could calculate a nonadiabatic isentropic expansion; but the experiment revealed that the expansion was nonisentropic, probably because of substantial dissipation caused by turbulence or heat transfer to the wall materials. The dissipation term in SIMMER was changed so that dissipation energy flowed only into the gas phase. We believe that this is correct for present applications because, in the normal co-current flow of liquid and gas phases, the Reynolds number is always higher in the gas. Also, dissipation energy was not allowed to be added directly to the solid field because the energy has to be transported first through the wall interface.

Test 10 reveals a transient that can be described by a polytropic expansion with an exponent of ~ 1.27 . The dissipation energy added to the gas field is a function of the friction factor at the walls multiplied by the square of the gas velocities. Because the code does not provide for a local description of turbulent dissipation inside a pure fluid cell, we found it necessary to add a multiplier on the dissipation function. A factor of 4 produced reasonable agreement between calculation and experiment.

Figures 7 through 10 show the pressure histories of the lower base, the spacer, the lower UCS, and of the upper UCS, respectively. The piston displacement from its initial position is plotted in Fig. 11. The pressure plots reveal excellent agreement in time response and absolute values. The piston mass had to be increased (from 513 to 680 g) to take into account approximately the friction through the piston guide tube. Generally, the piston mass is adjusted in a broad range to match the measured time of flight. This is done to ensure a reasonably good upper boundary condition.

An important parameter for the description of heat transfer to walls in SIMMER is the structure-side heat-transfer coefficient, which describes the conduction of energy from the wall interface to the point of the reference wall temperature. It can be estimated as a function of the wall thickness that

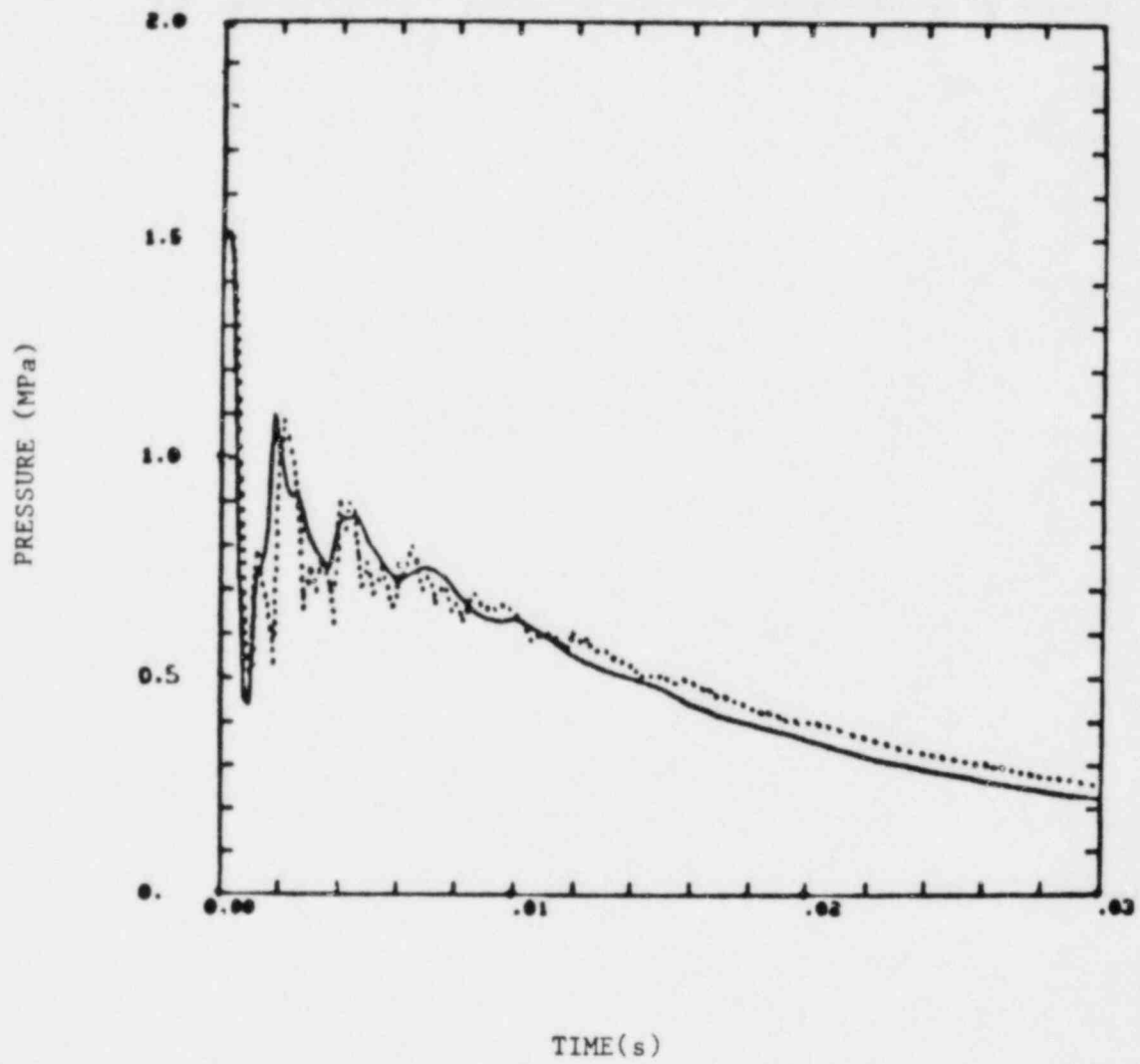


Fig. 7. Test 10, lower base pressure.

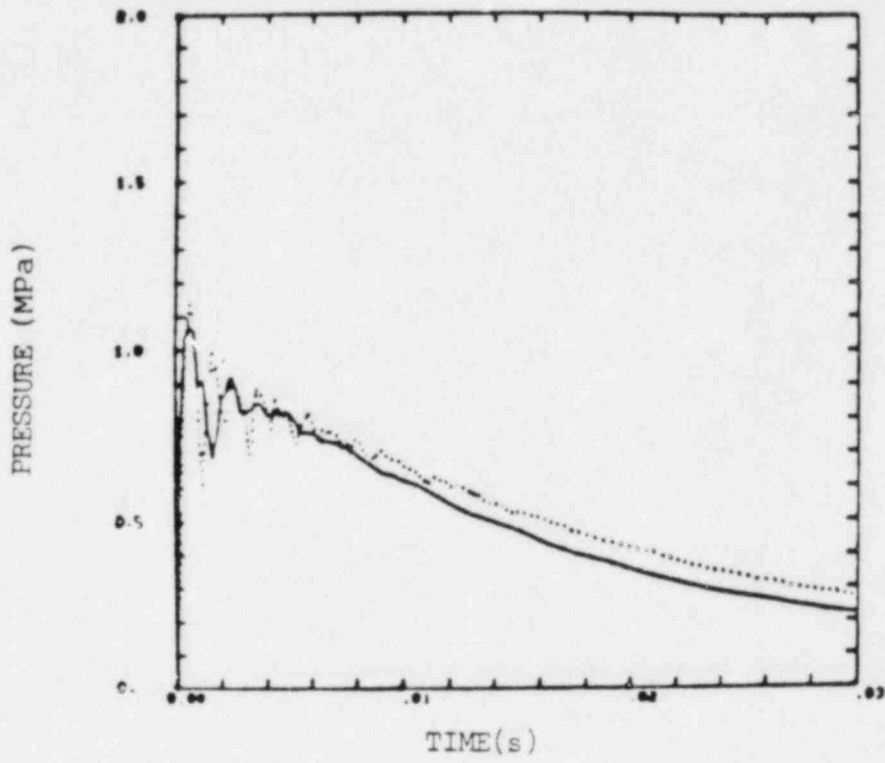


Fig. 8. Test 10, spacer pressure.

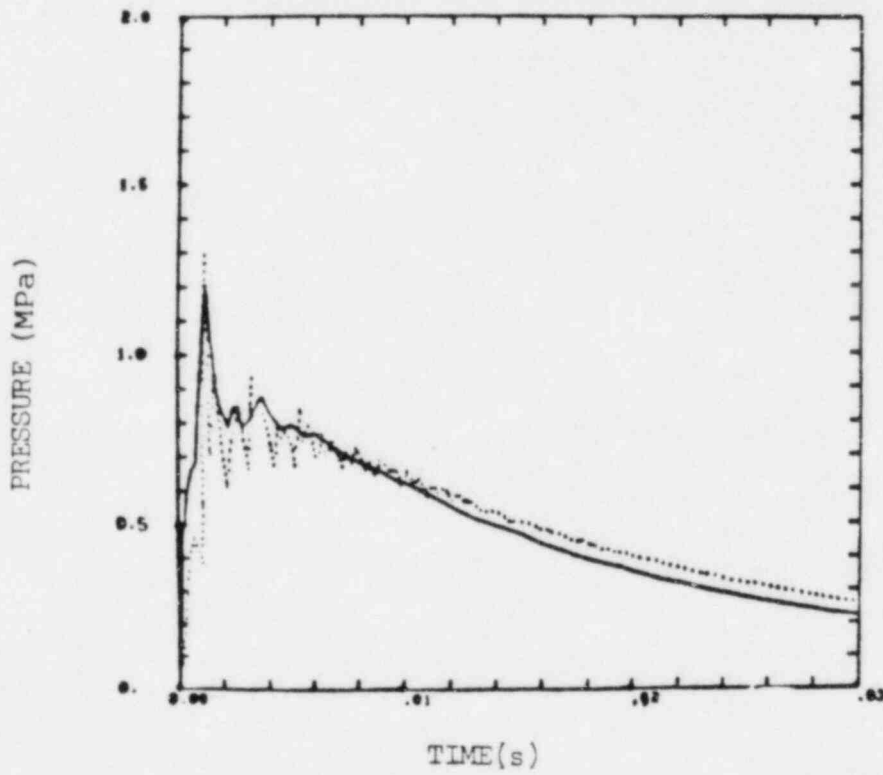


Fig. 9. Test 10, lower UCS pressure.

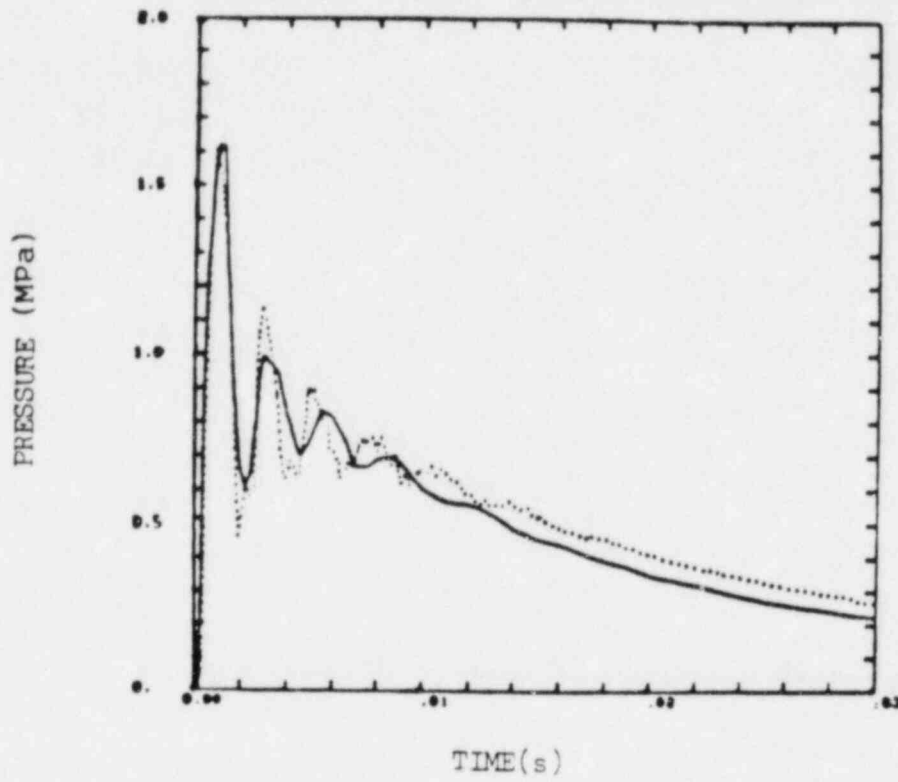


Fig. 10. Test 10, upper UCS pressure.

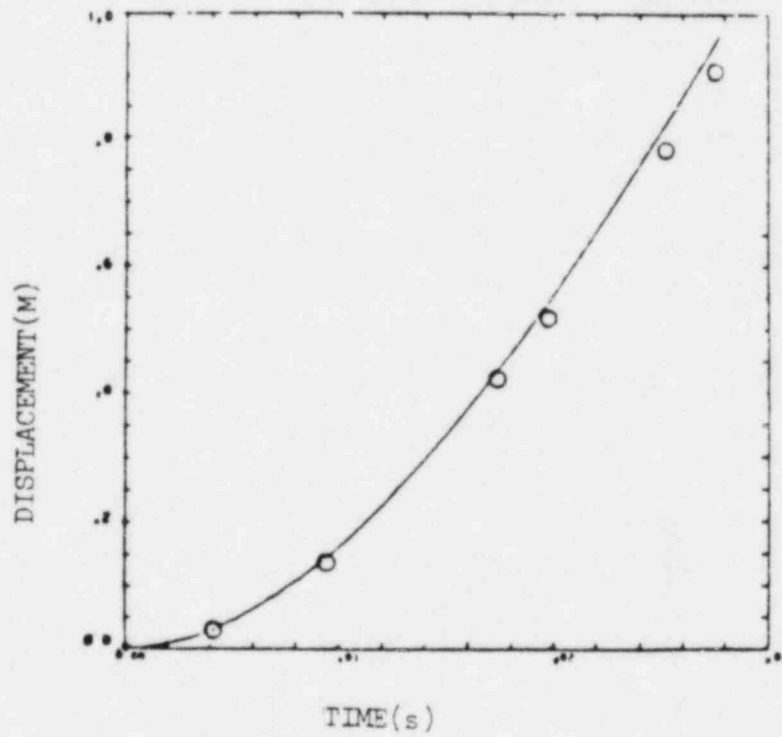


Fig. 11. Test 10, piston displacement.

changes temperature change during the anticipated transient. The larger this parameter, the more energy that can be exchanged with the wall. The wall of the UCS primarily will be heat sink, the magnitude of which will be given by the structure-side heat-transfer coefficient. For the helium test, the gas expansion yields a temperature decrease, causing energy to flow from the wall into the gas. This effect is significant at late times ($\gtrsim 30$ ms), whereas the dissipation significantly increases the gas temperature between 2 and 10 ms. A substantial temperature difference between wall and gas is present after ~ 10 ms. The magnitude of the inside-wall heat-transfer coefficient depends on the transient condition at the wall surface. It is not possible, strictly speaking, to assign a constant coefficient by estimating heat penetration depths. Nevertheless, the coefficient is chosen to be 900 W/cm K for test 10, which is rather low for a wall of aluminum. It can be argued that, at late times, the dissipation inside the gas is overestimated so that the heat transfer from the wall has to be underestimated to keep the proper balance.

An important consideration is to ensure that the pressure transducers, sealed with a rubber cap, measure the proper pressure transients. SIMMER gas dynamics were verified using analytical solutions to simple one-dimensional problems.* It is known, therefore, that wave propagations and frequency responses of the closed system will be calculated well by SIMMER. The good agreement between experimental and predicted frequencies suggests that the pressure transducers are not overly affected by thermal effects. The fact that the SIMMER amplitude decrease is greater than that observed in the experiment probably is due to the numerical differencing method of the code, which diffuses peaks more than can be expected on physical grounds alone.

C. Propanol Tests

Eight successful propanol tests have been performed in this test program, all of which are included in Table IV. The unsuccessful test 15 was not calculated because the pin structure broke loose and moved against the piston. This experiment was repeated in test 18 with a newly constructed clamping ring for the 217-pin bundle. Figures 12 through 14 show calculated pressure traces

*These data were supplied by P. J. Blewett, Los Alamos National Laboratory Group Q-8.

with a moving piston, with the piston stuck in its lowest position, and with the piston stuck in its highest position, respectively -- with initial conditions simulating test 12. Figures 15 through 67 show the results of the propanol tests. The solid lines always show the experimental results, whereas the broken lines show results of SIMMER calculations. The experimental signals of the piston displacement are sets of six points in the diagrams.

The seven-hole array UCS was used four times. In tests 12 and 13, the same inventories of liquid propanol and slightly different initial pressures were used. In test 12 (see Figs. 12 through 20), the rupture-disk-breaking mechanism was not used. Instead, the rupture disk broke by itself at a pressure of 1.18×10^6 Pa. In test 13 (see Figs. 21 through 26), the rupture-disk-breaking mechanism was activated at a pressure of 1.11×10^6 Pa. The signal from the lowermost pressure transducer, which reads the lower base pressure, shows considerable oscillations caused by the frequencies introduced into the liquid fluid/rigid wall system when the activator piston is stopped. To reduce the amplitude of these oscillations, further tests were performed with a more flexible stopping mechanism. In addition, the analog signal is filtered for convenient reading.

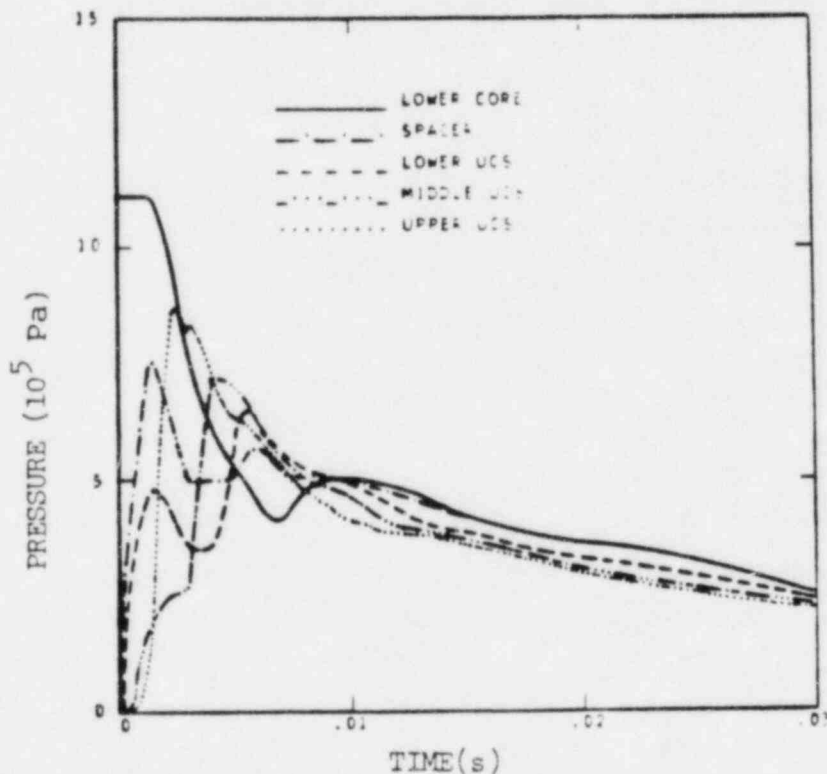


Fig. 12. Test 12, moving piston.

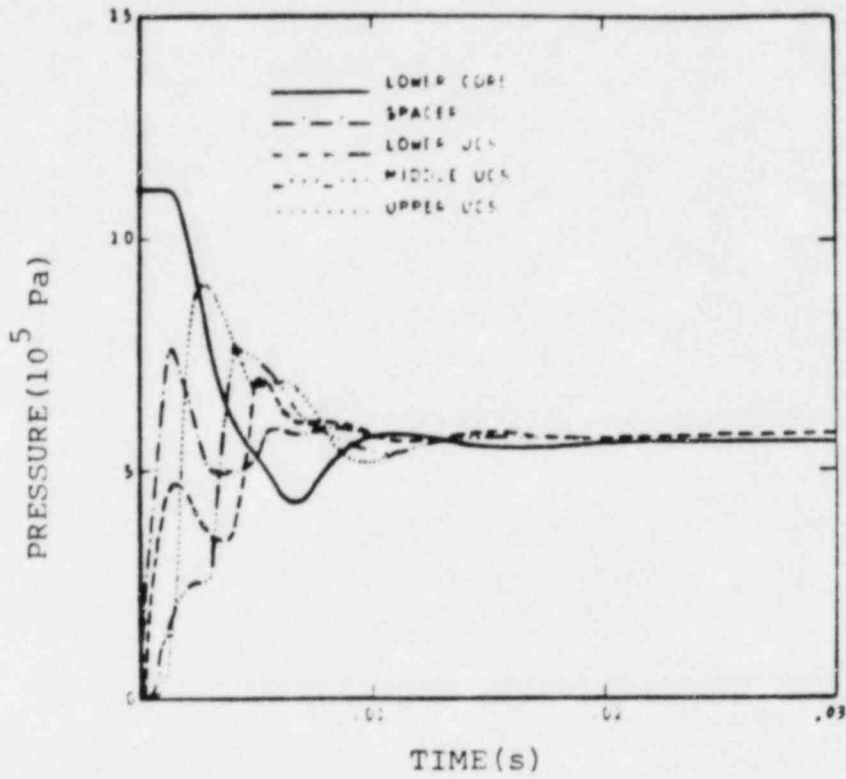


Fig. 13. Test 12, piston stuck in lowest position.

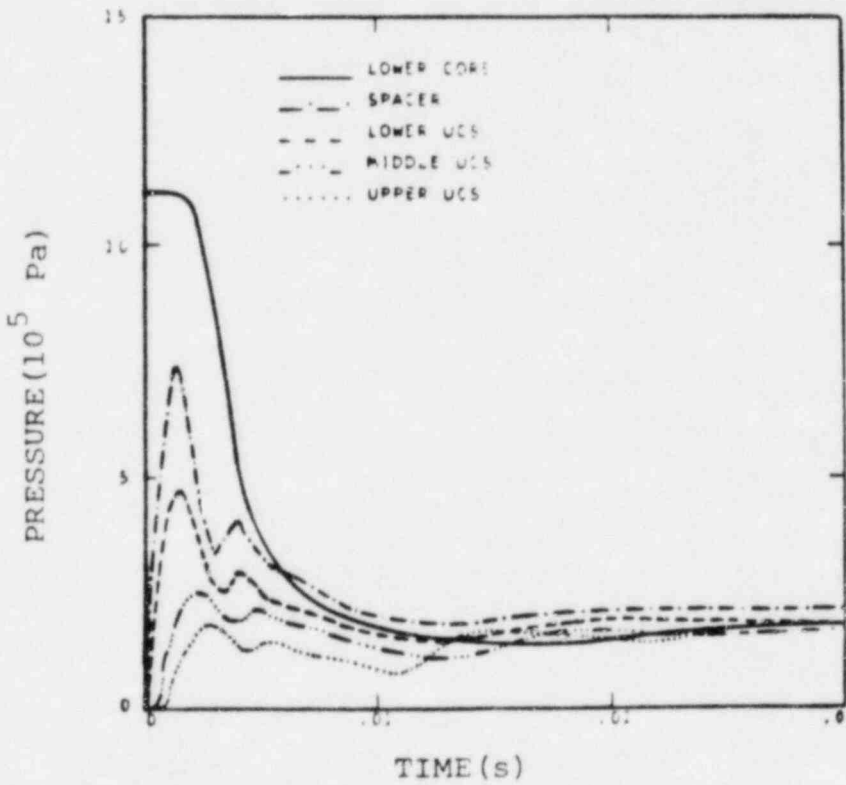


Fig. 14. Test 12, piston stuck in highest position.

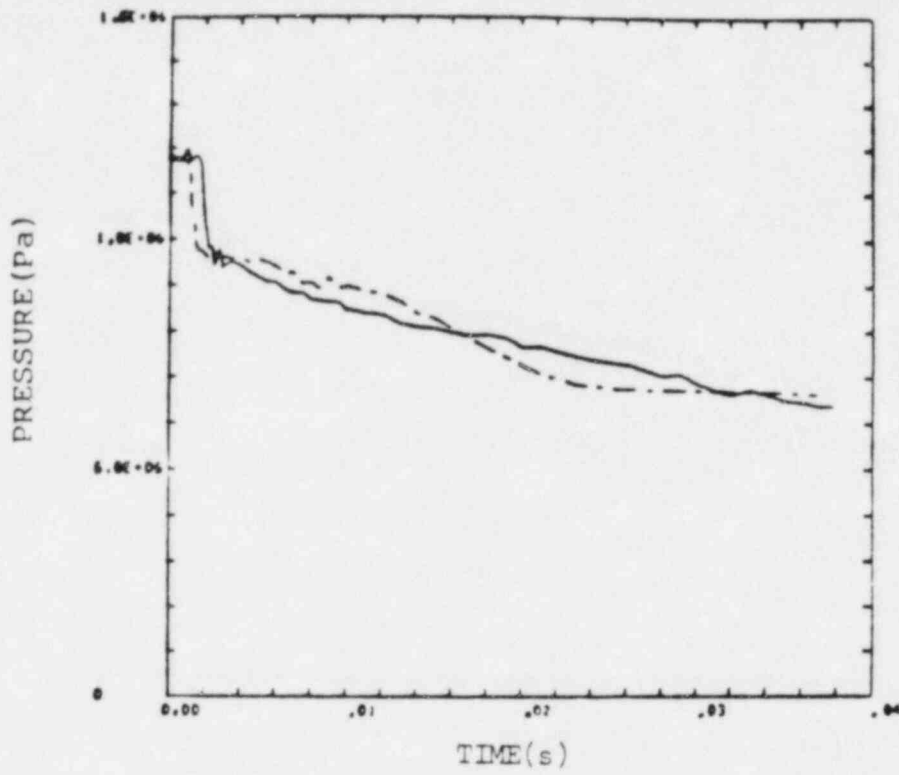


Fig. 15. Test 12, lower base pressure.

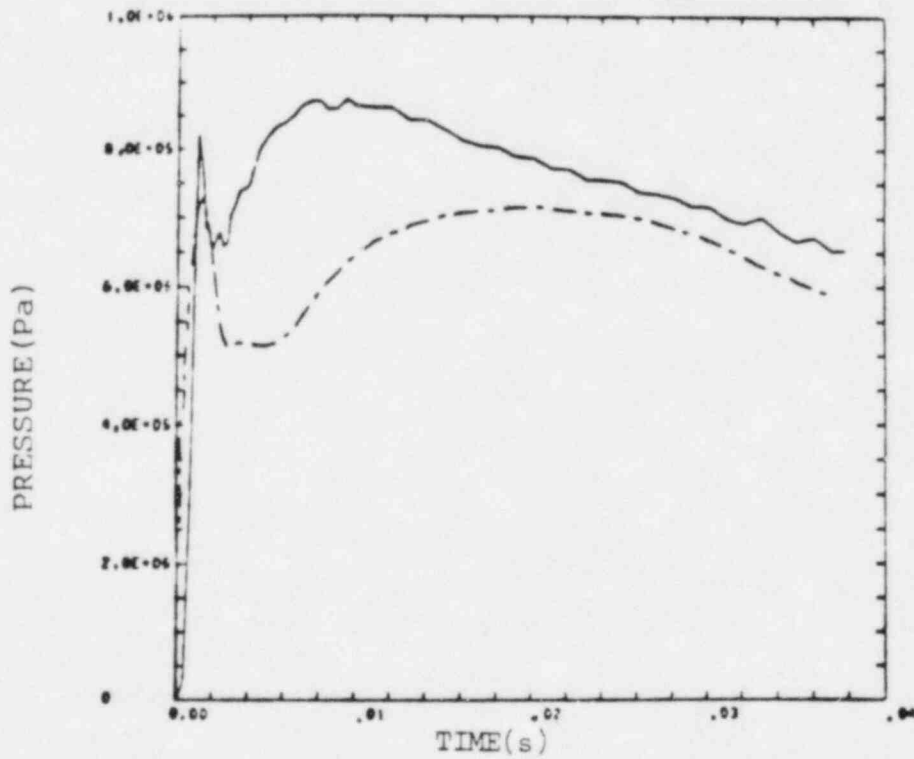


Fig. 16. Test 12, spacer pressure.

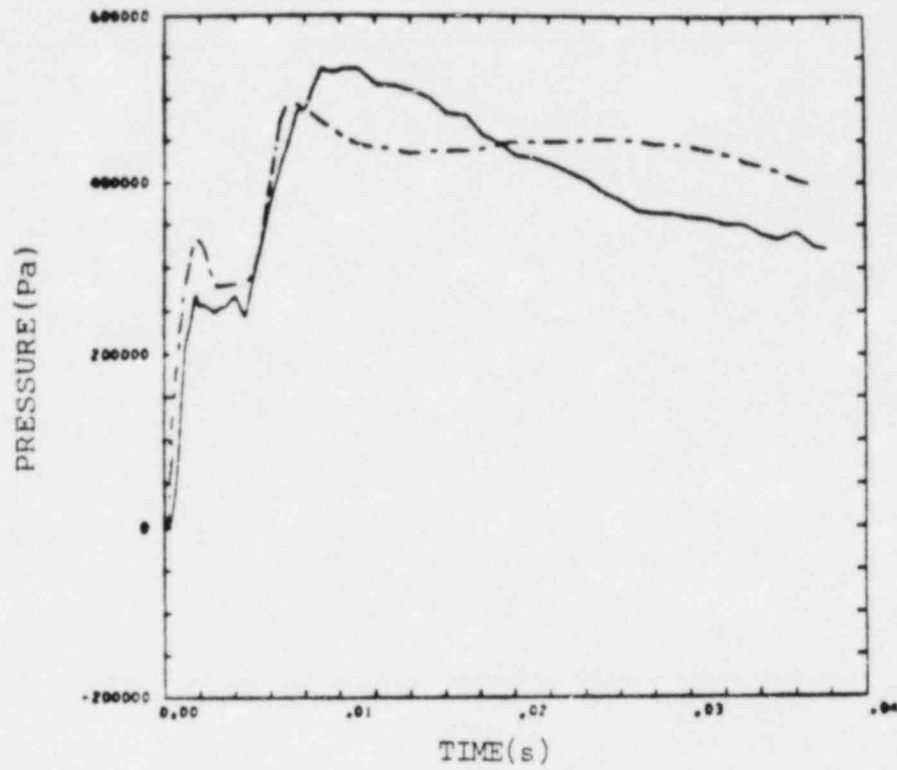


Fig. 17. Test 12, lower UCS pressure.

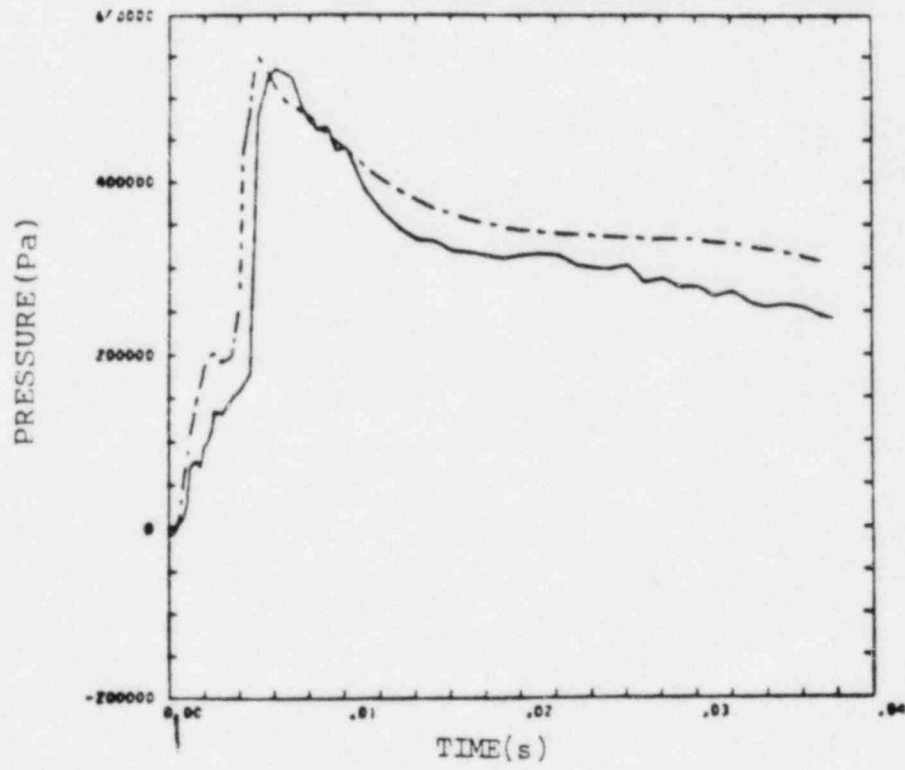


Fig. 18. Test 12, middle UCS pressure.

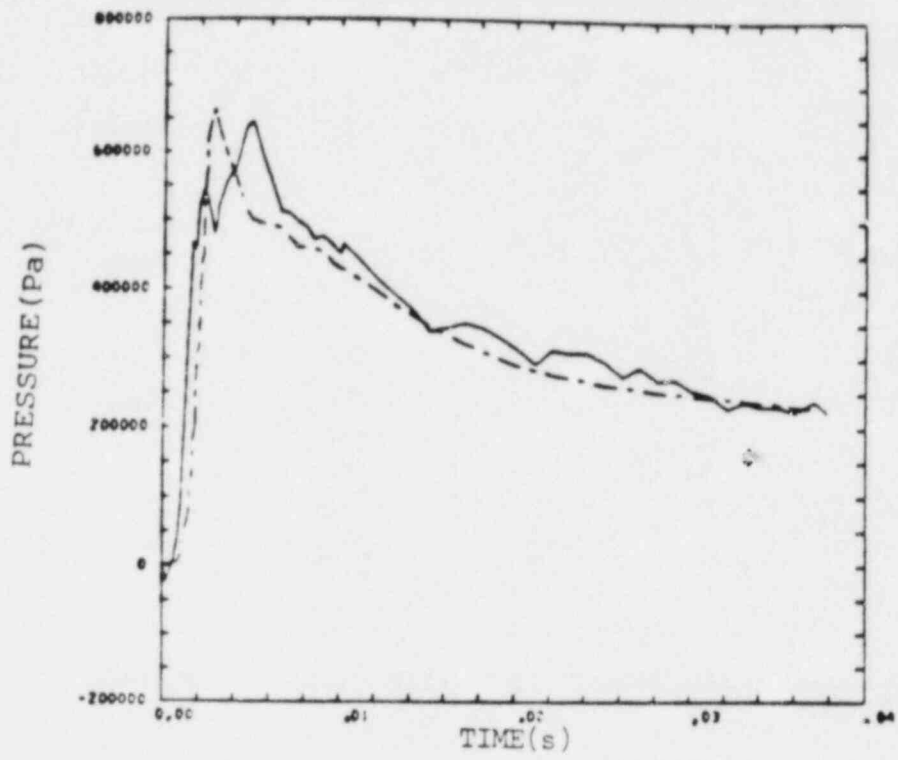


Fig. 19. Test 12, upper UCS pressure.

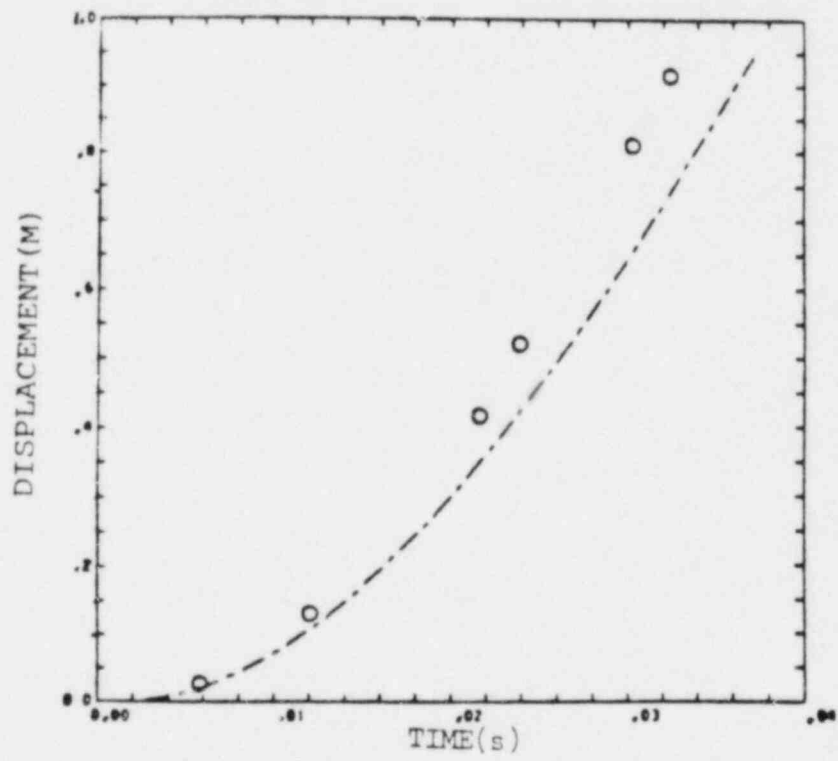


Fig. 20. Test 12, piston displacement.

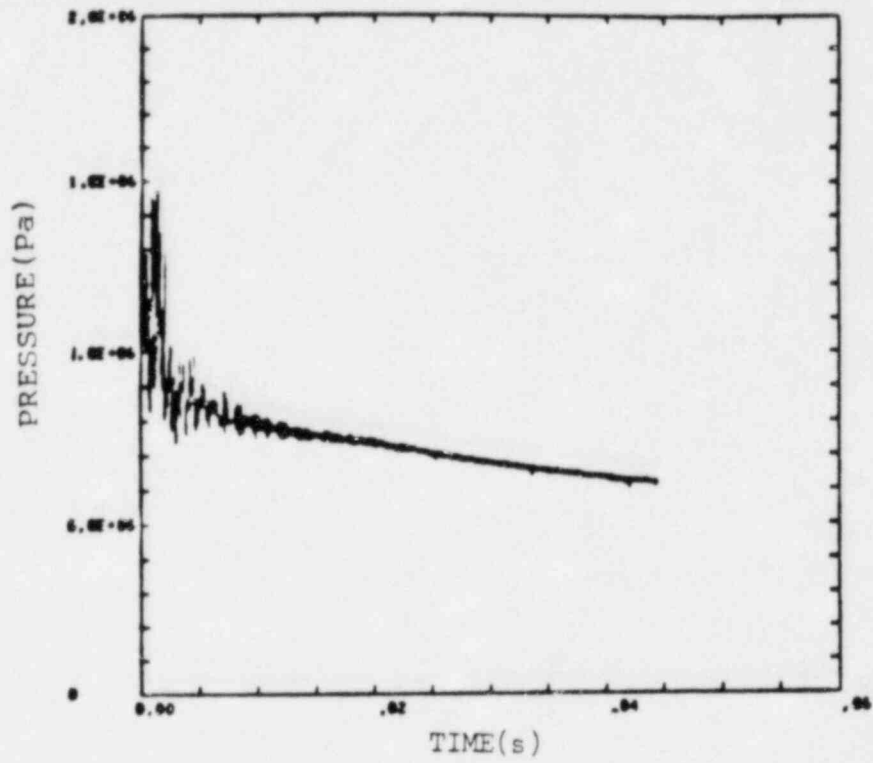


Fig. 21. Test 13, lower base pressure.

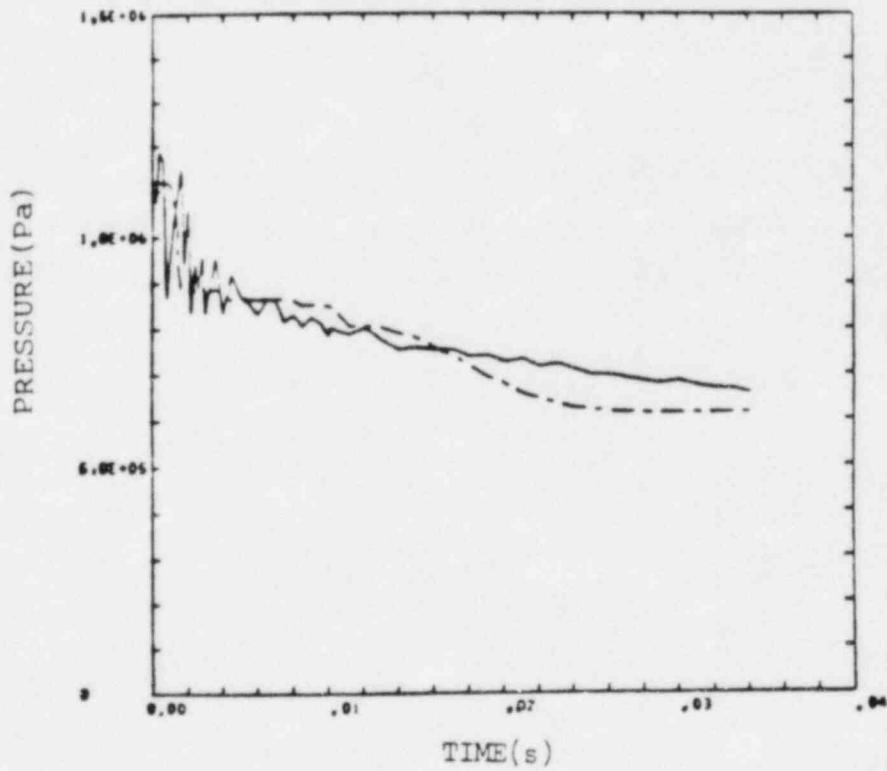


Fig. 22. Test 13, lower base pressure.

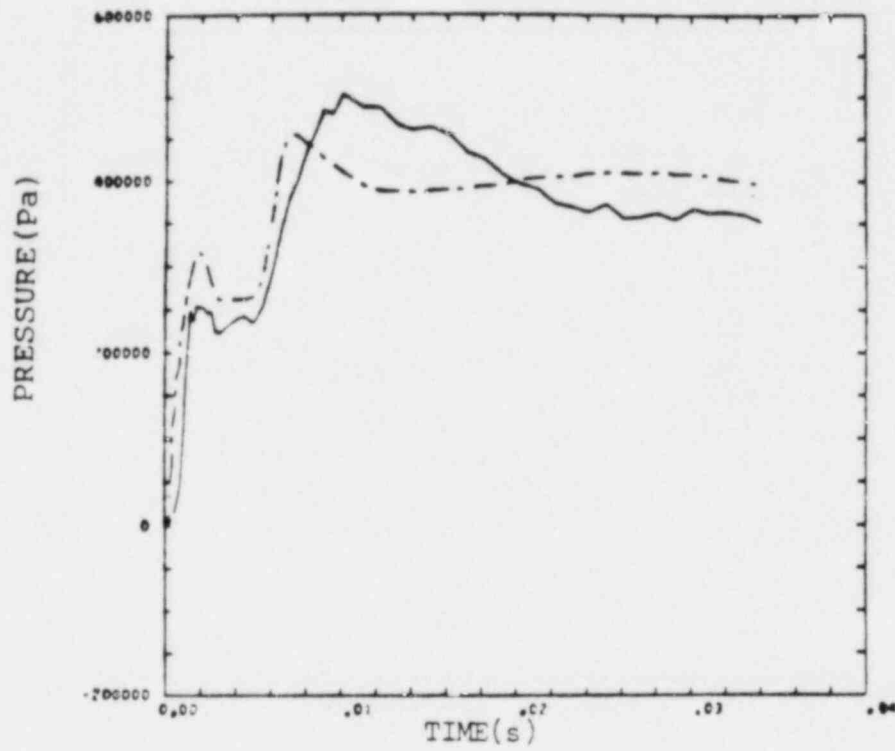


Fig. 23. Test 13, lower UCS pressure.

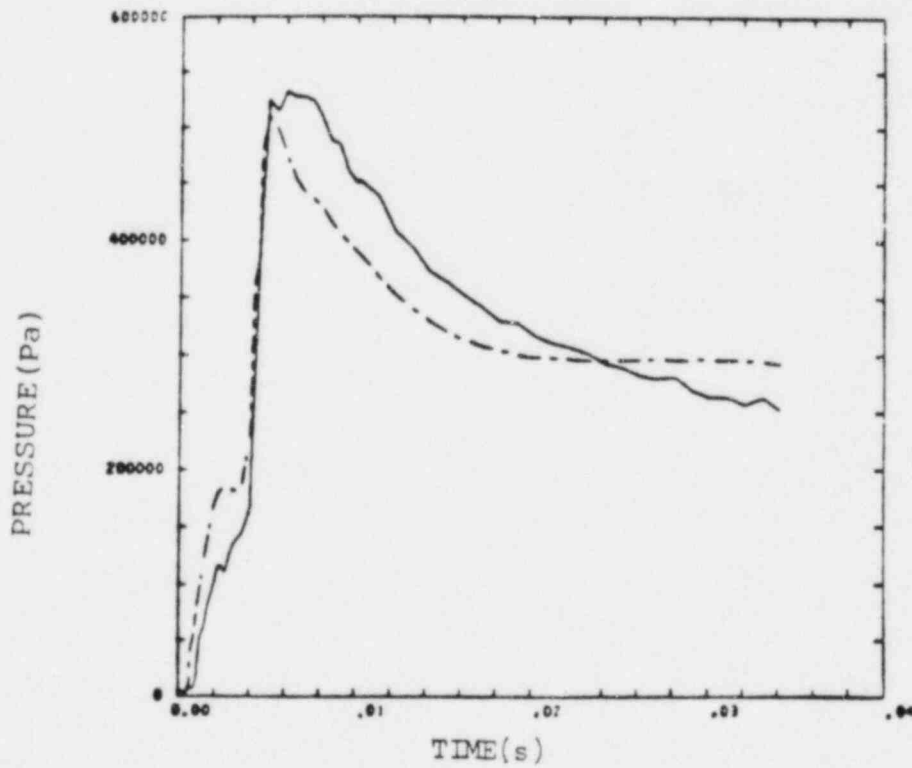


Fig. 24. Test 13, middle UCS pressure.

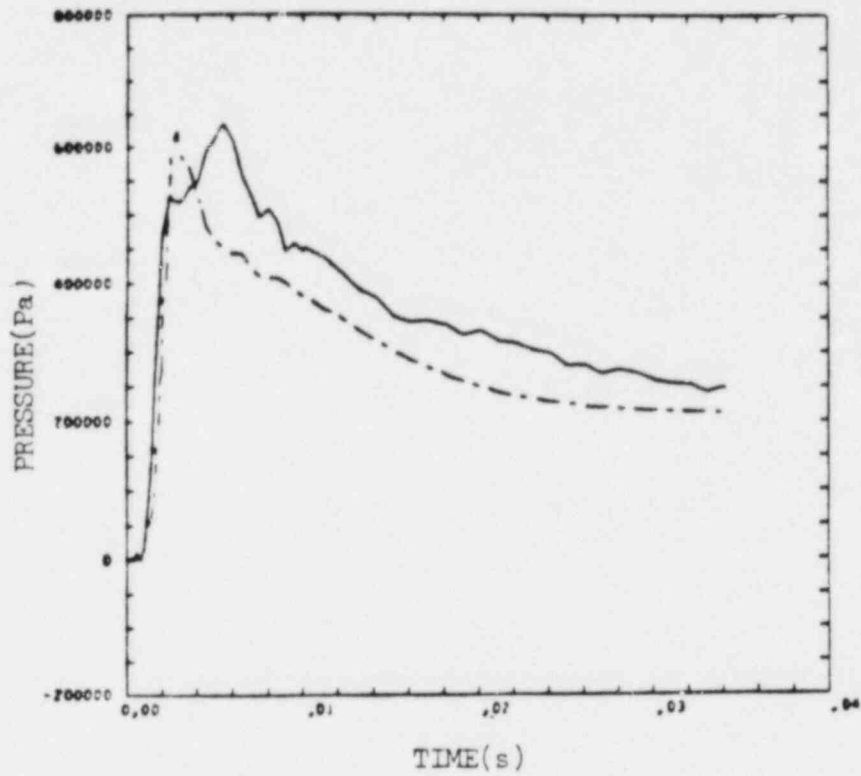


Fig. 25. Test 13, upper UCS pressure.

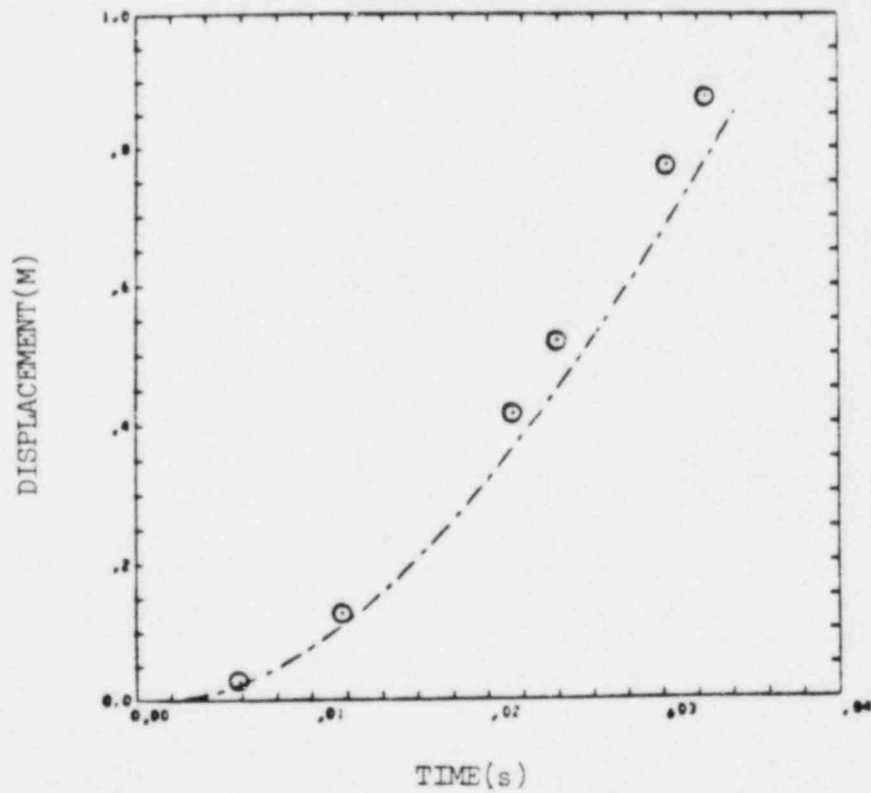


Fig. 26. Test 13, piston displacement.

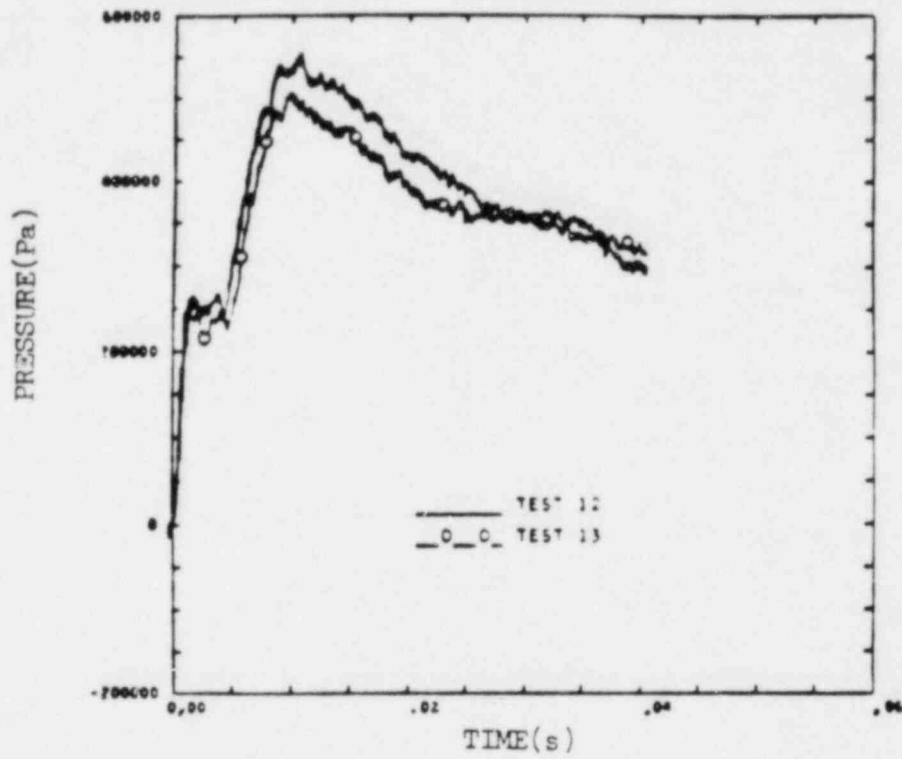


Fig. 27. Test 12-Test 13, lower UCS pressure.

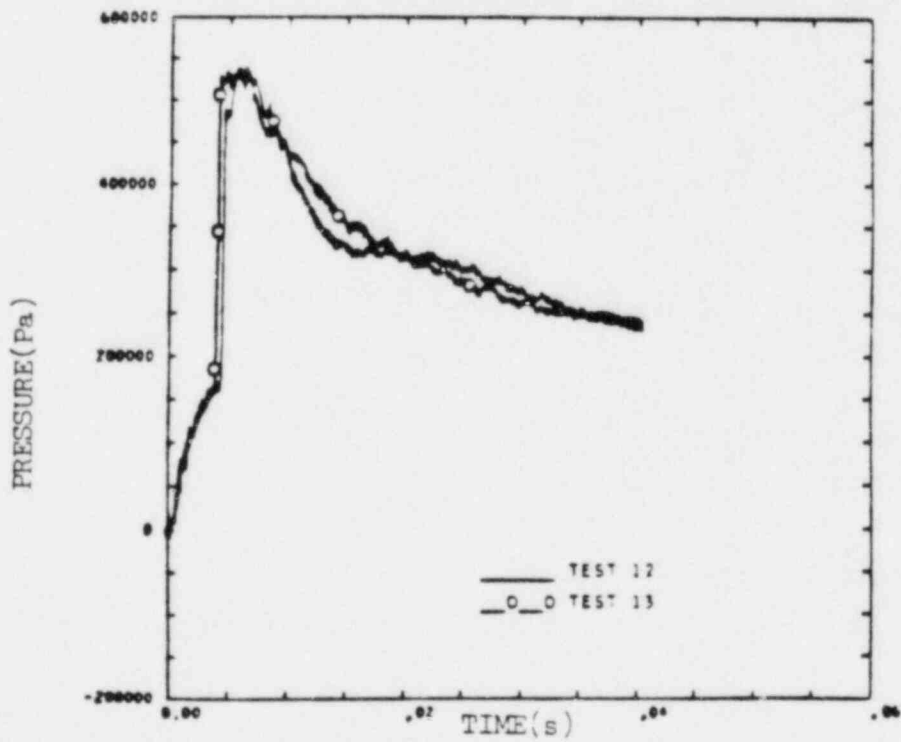


Fig. 28. Test 12-Test 13, middle UCS pressure.

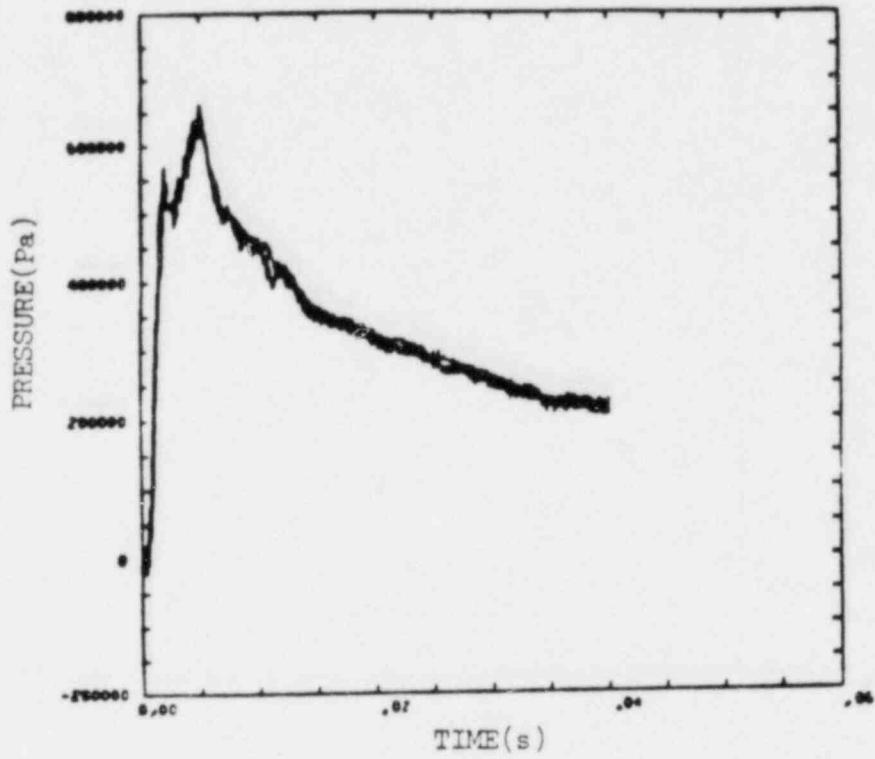


Fig. 29. Test 12-Test 13, upper UCS pressure.

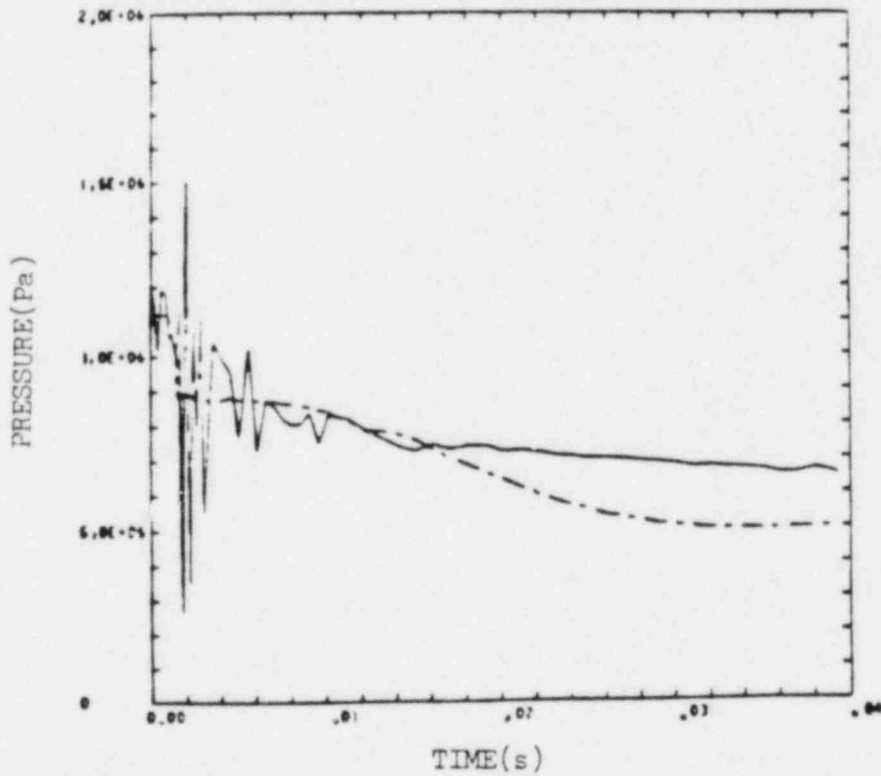


Fig. 30. Test 14, lower base pressure.

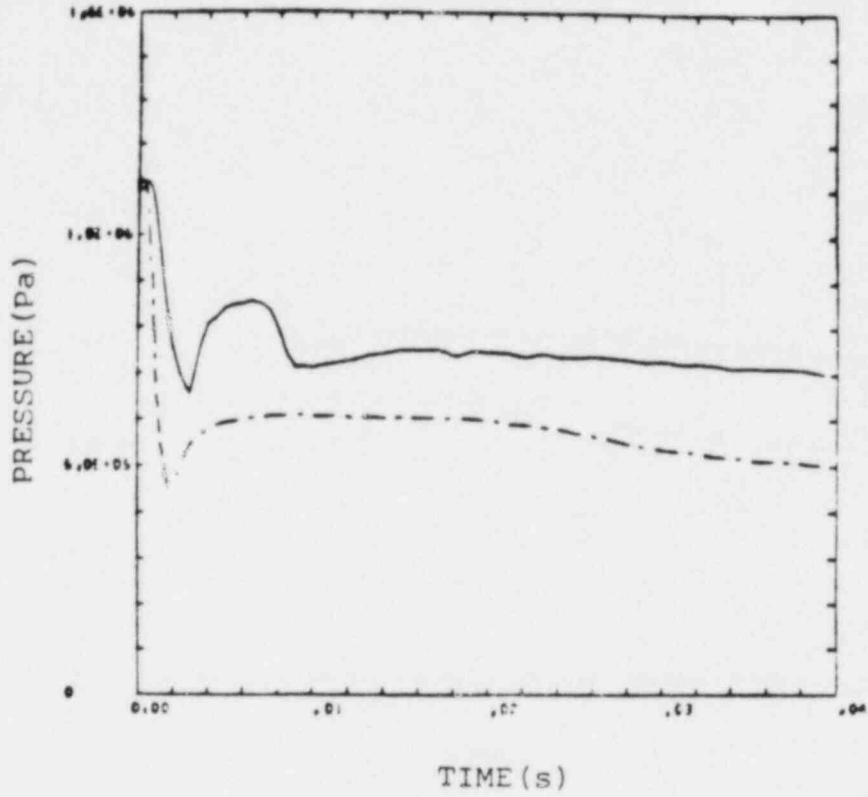


Fig. 31. Test 14, upper base pressure.

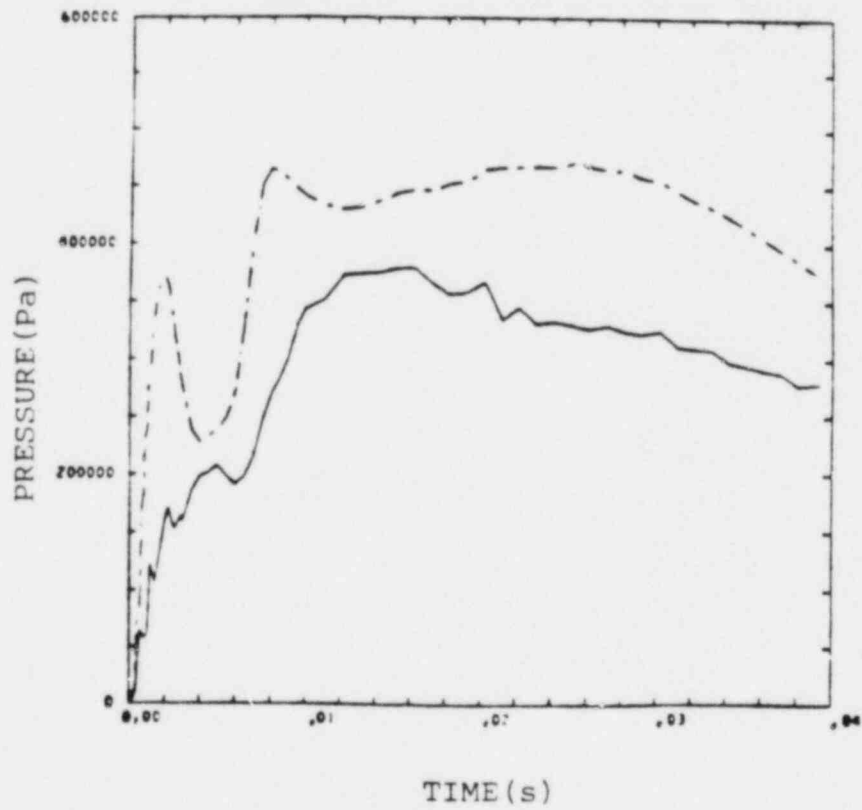


Fig. 32. Test 14, lower UCS pressure.

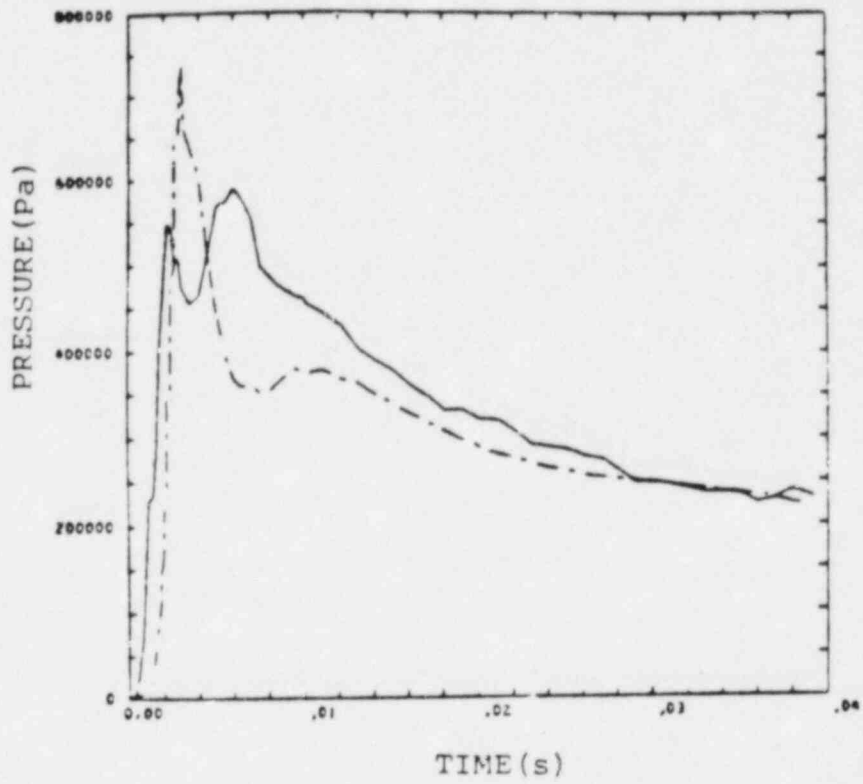


Fig. 33. Test 14, upper UCS pressure.

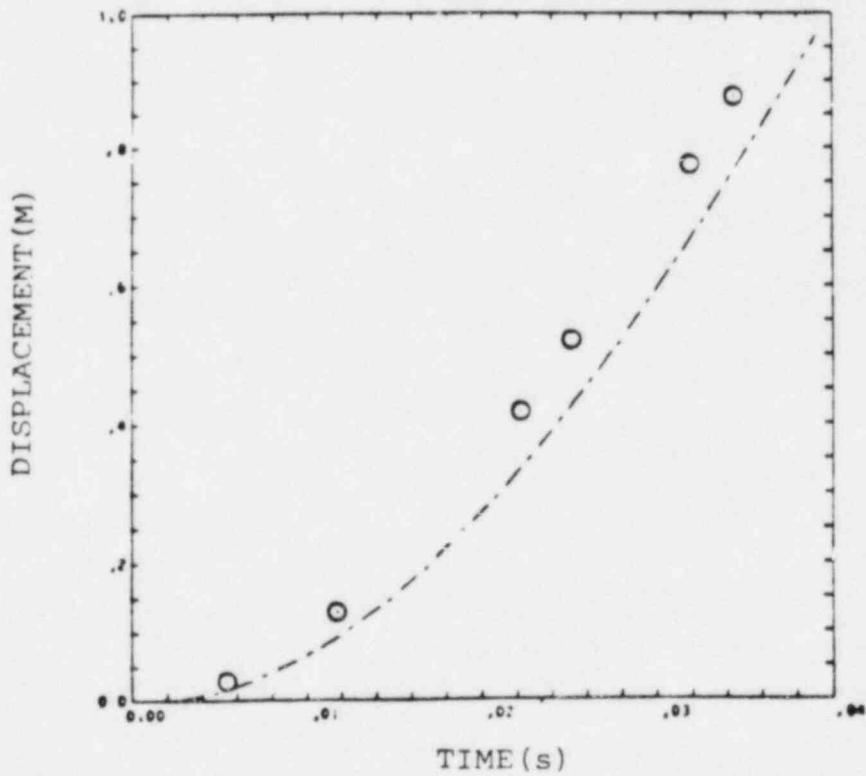


Fig. 34. Test 14, piston displacement.

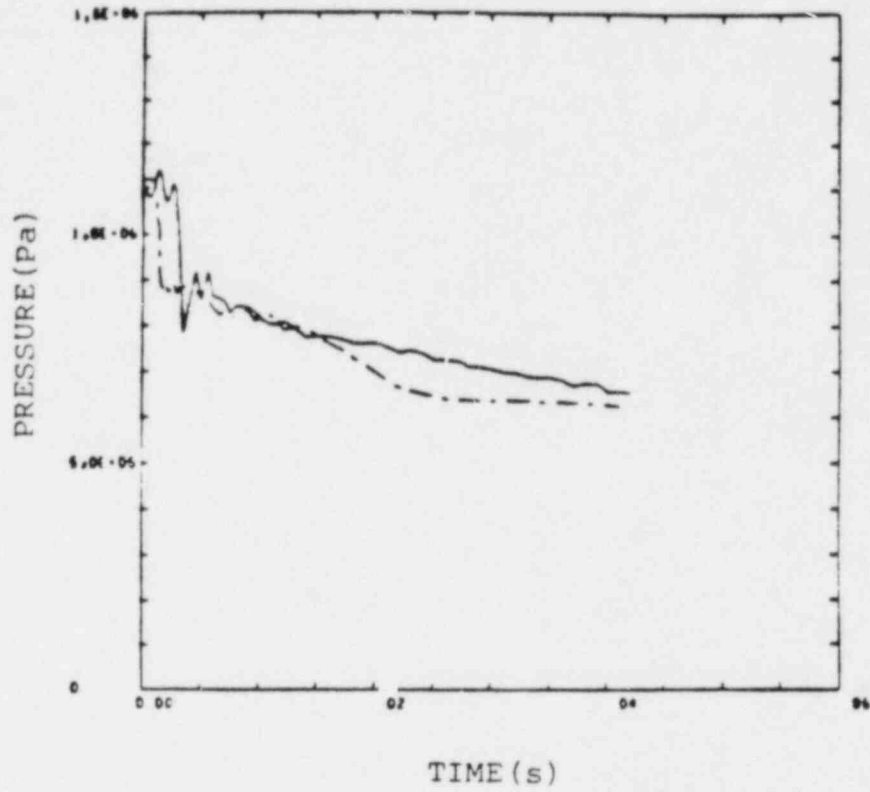


Fig. 35. Test 16, lower base pressure.

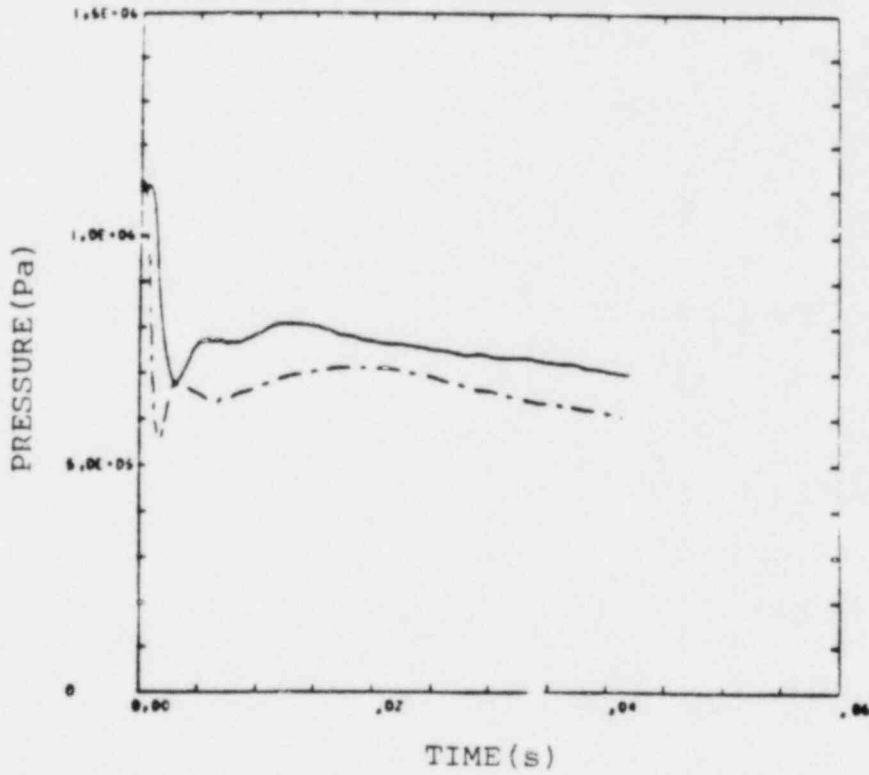


Fig. 36. Test 16, upper base pressure.

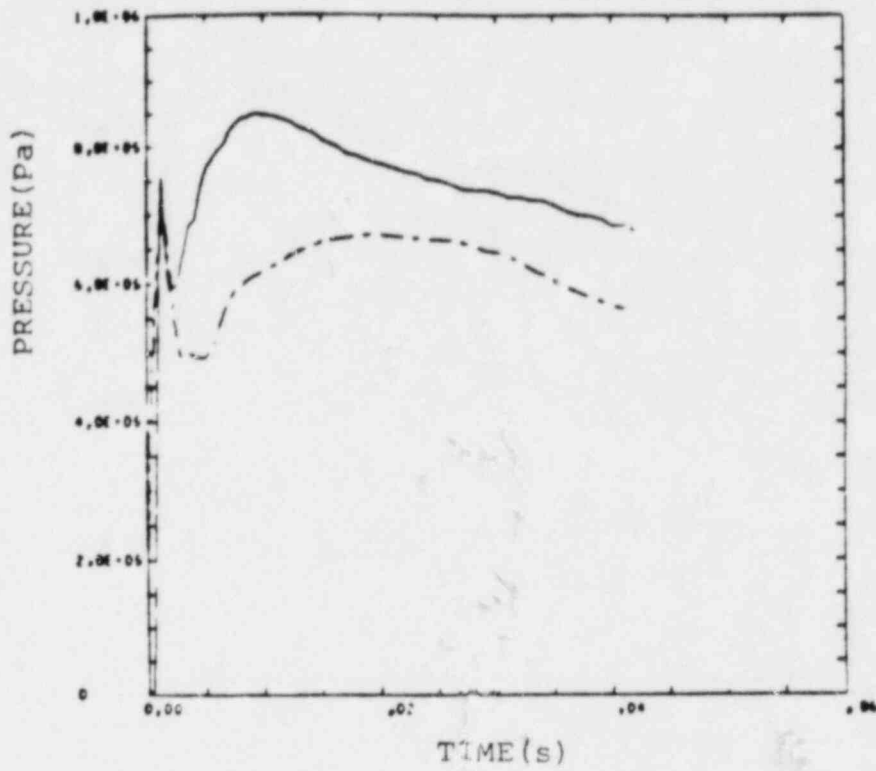


Fig. 37. Test 16, spacer pressure.

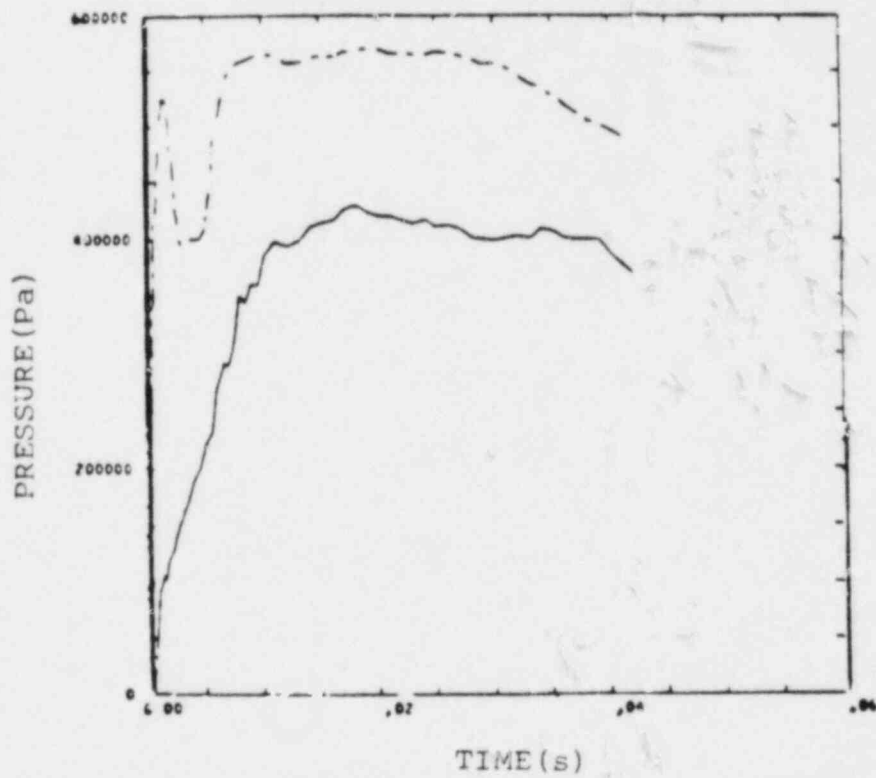


Fig. 38. Test 16, lower UCS pressure.

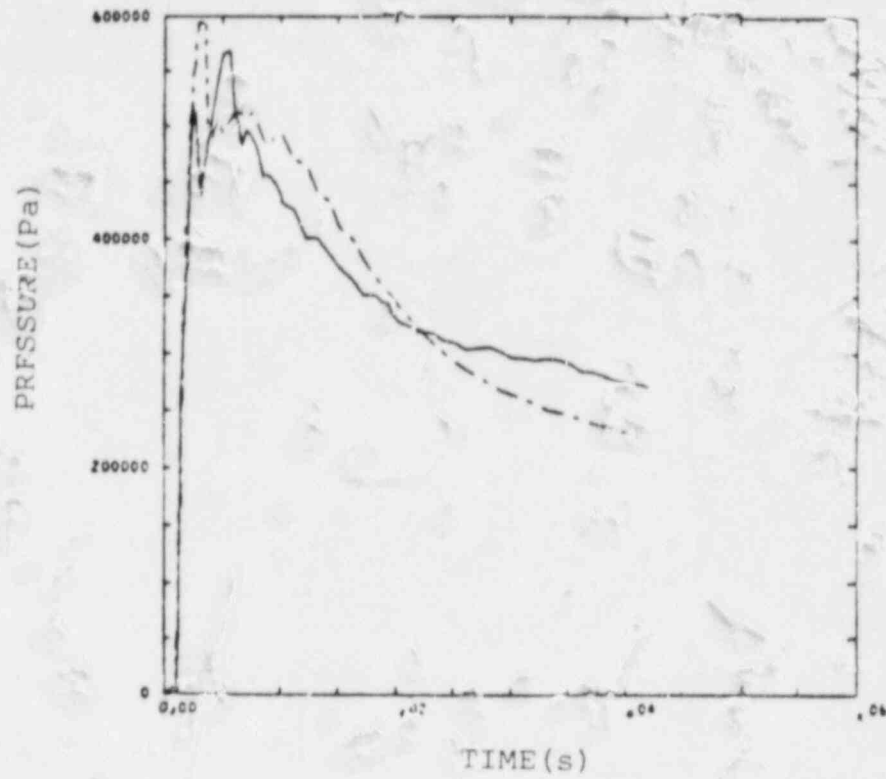


Fig. 39. Test 16, Upper UCS pressure.

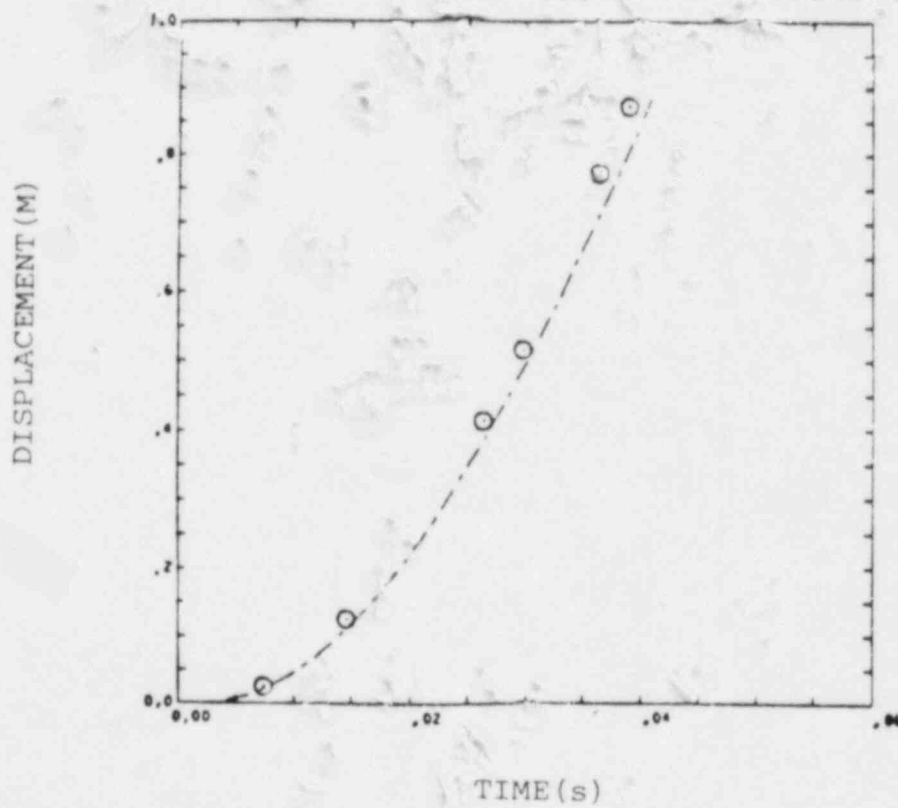


Fig. 40. Test 16, piston displacement.

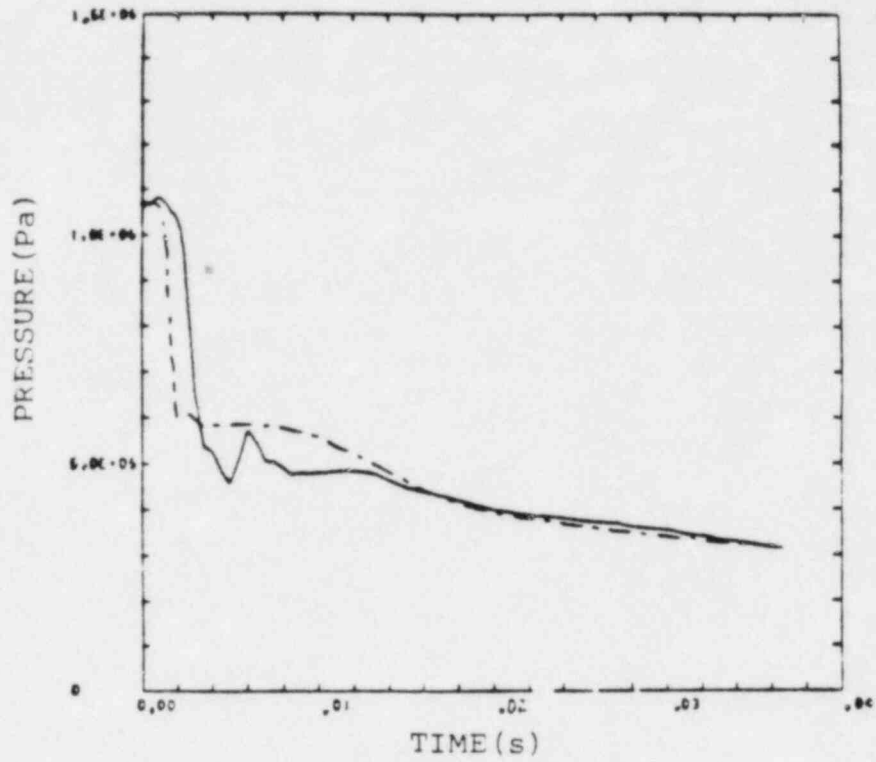


Fig. 41. Test 17, lower base pressure.

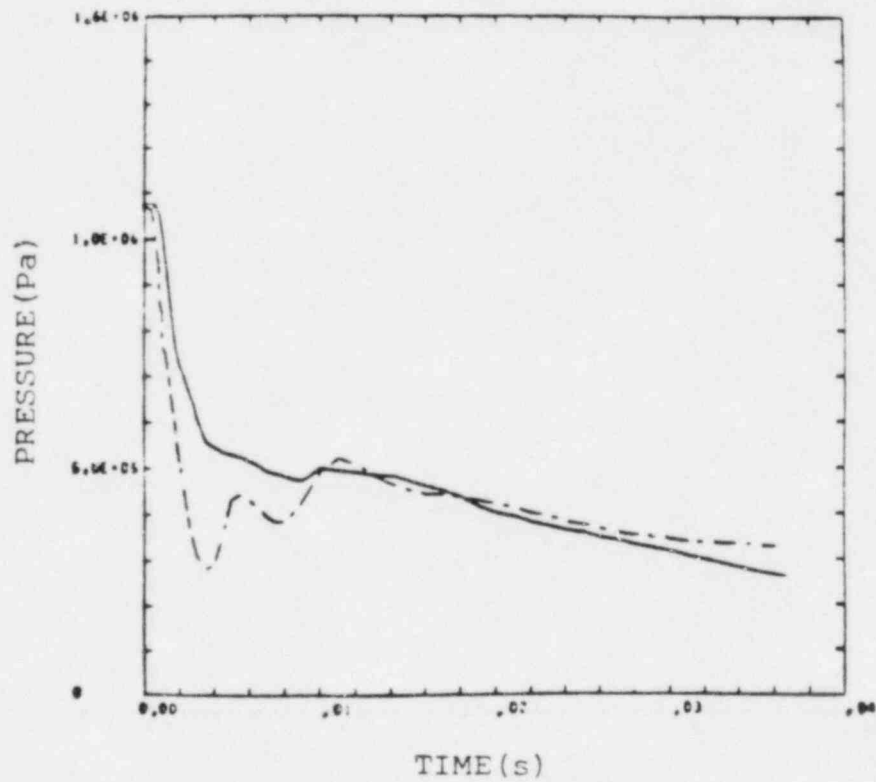


Fig. 42. Test 17, upper base pressure.

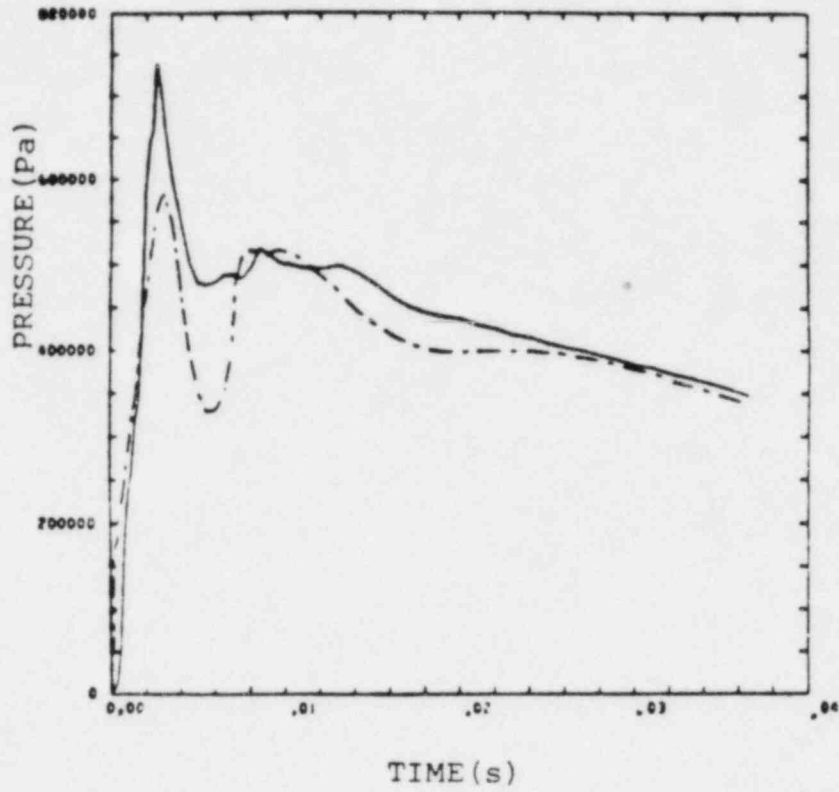


Fig. 43. Test 17, spacer pressure.

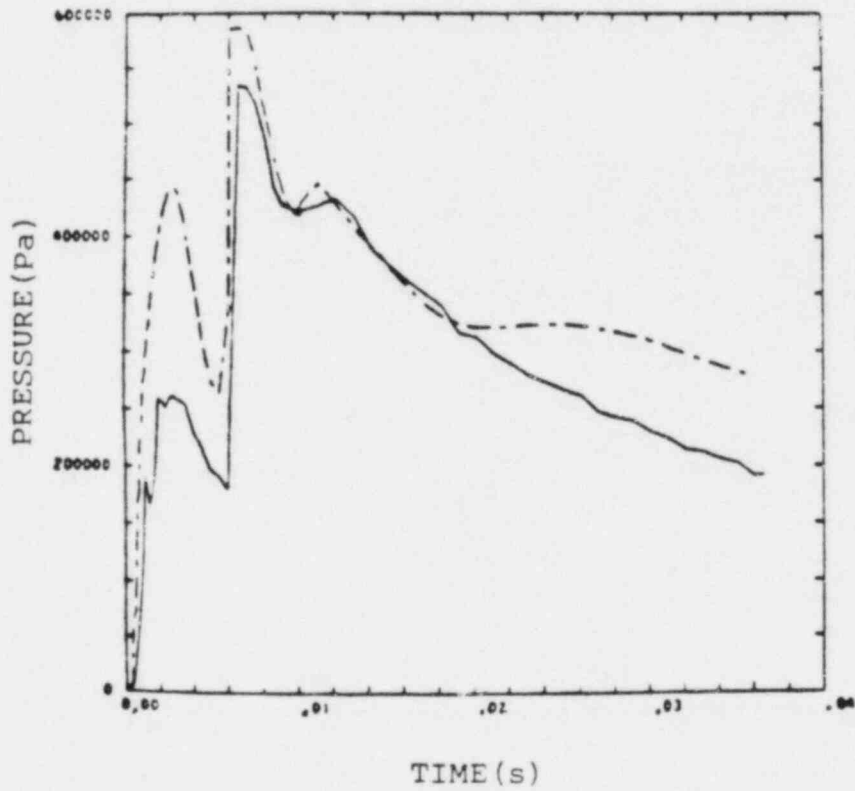


Fig. 44. Test 17, lower UCS pressure.

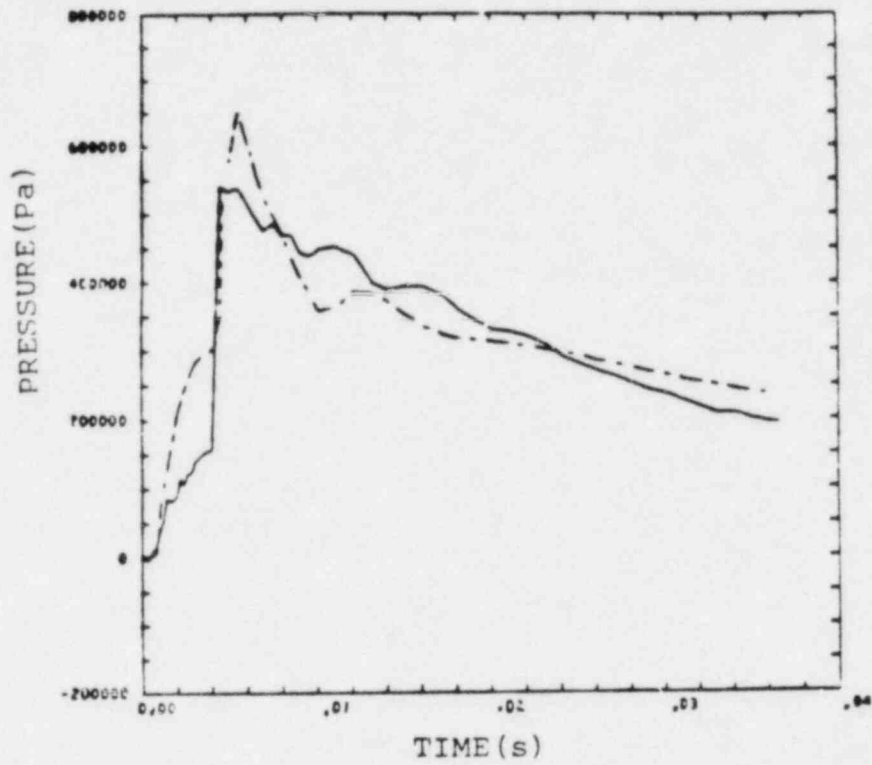


Fig. 45. Test 17, middle UCS pressure.

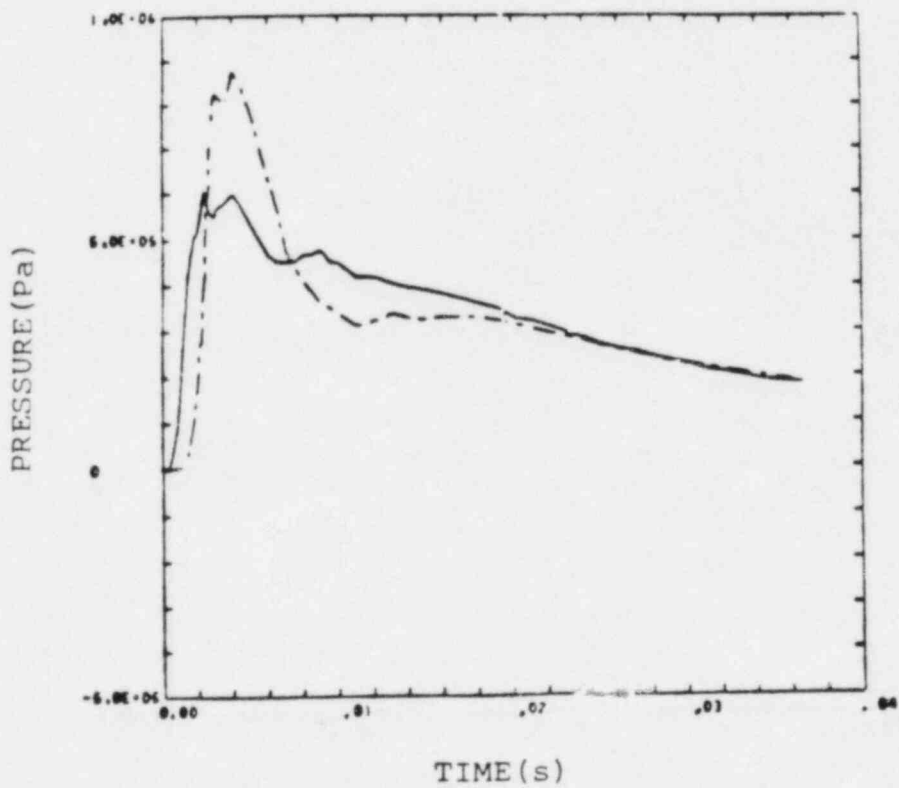


Fig. 46. Test 17, upper UCS pressure.

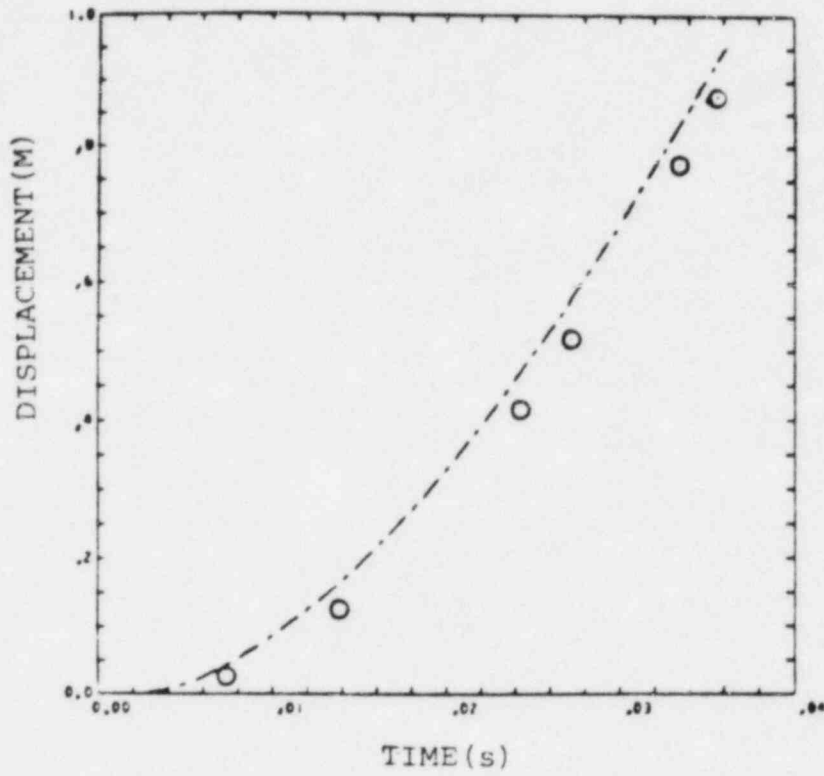


Fig. 47. Test 17, piston displacement.

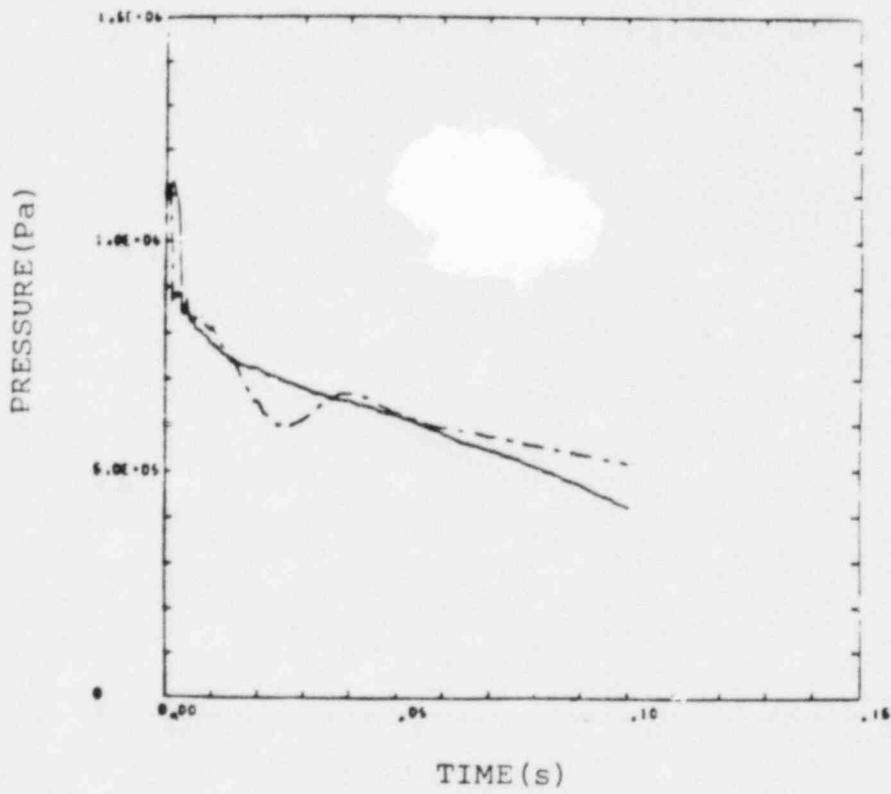


Fig. 48. Test 18, lower base pressure.

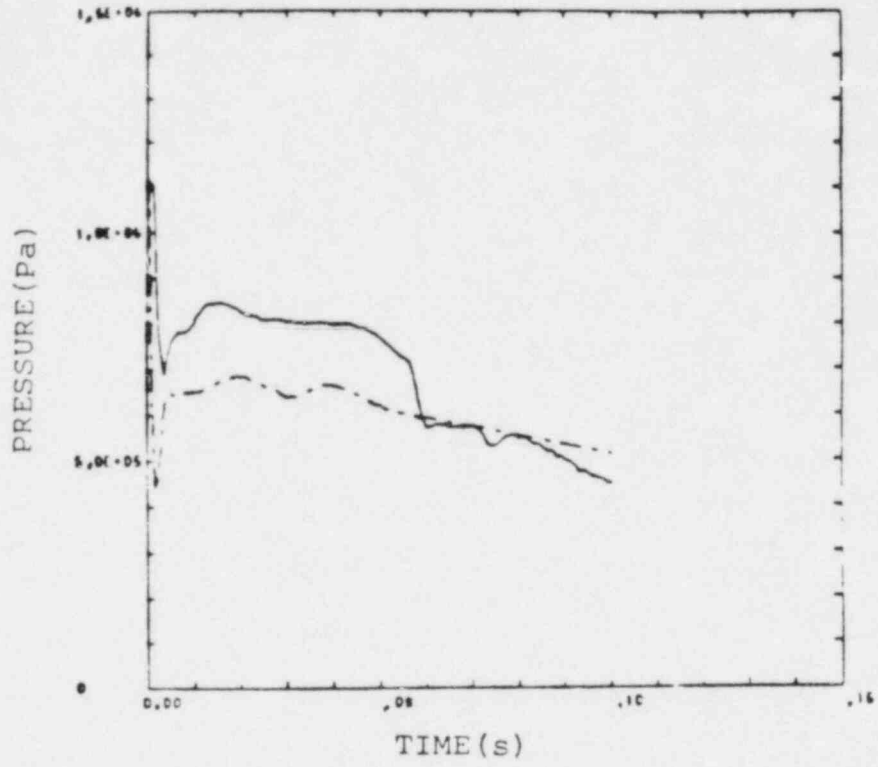


Fig. 49. Test 18, upper base pressure.

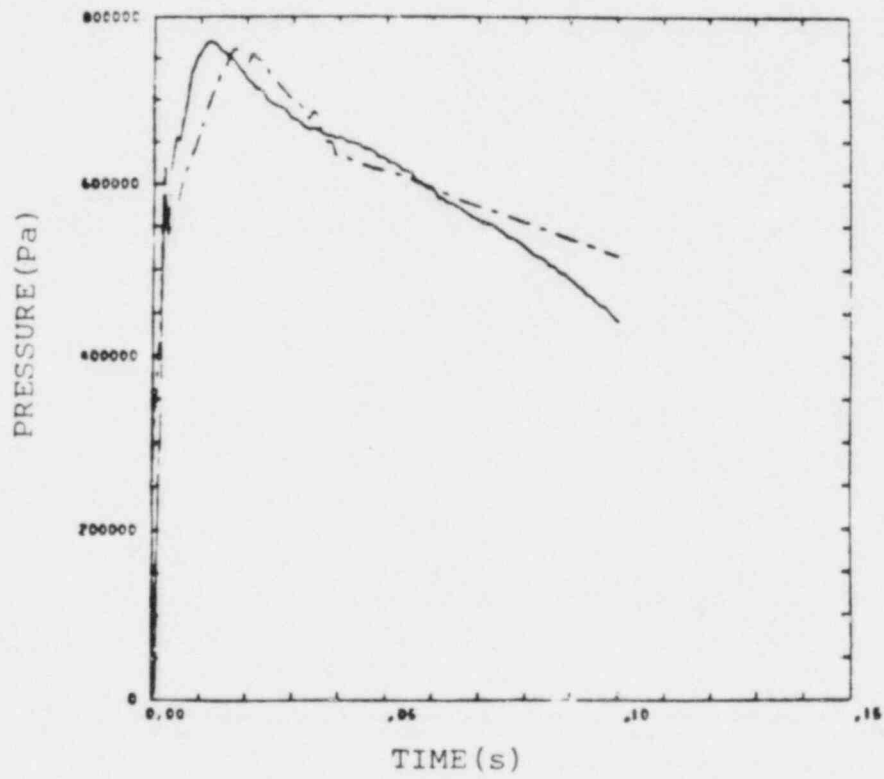


Fig. 50. Test 18, spacer pressure.

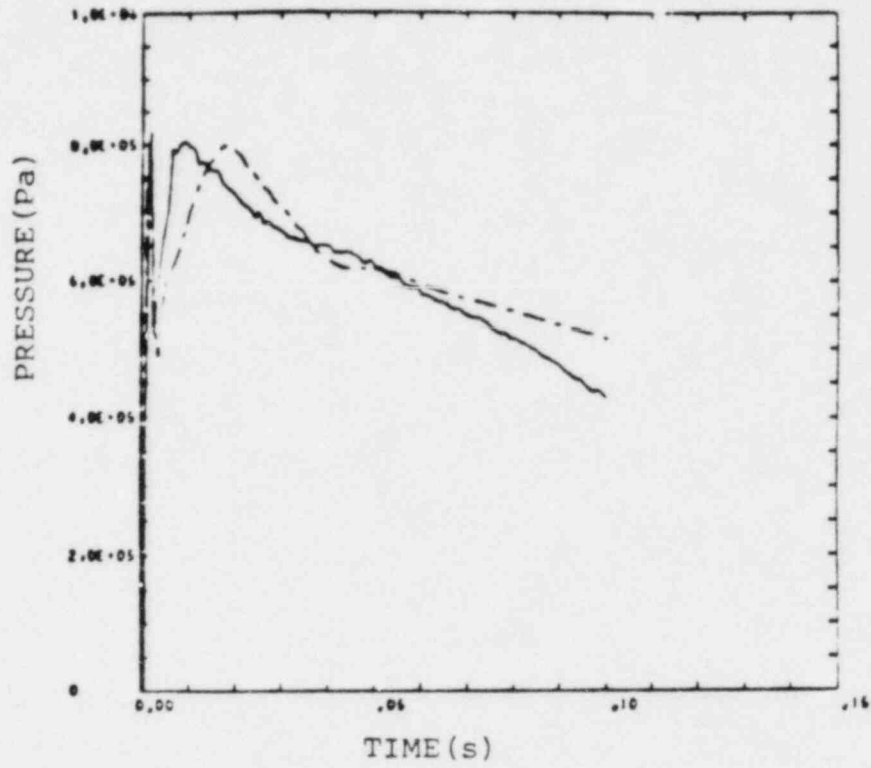


Fig. 51. Test 18, lower UCS pressure.

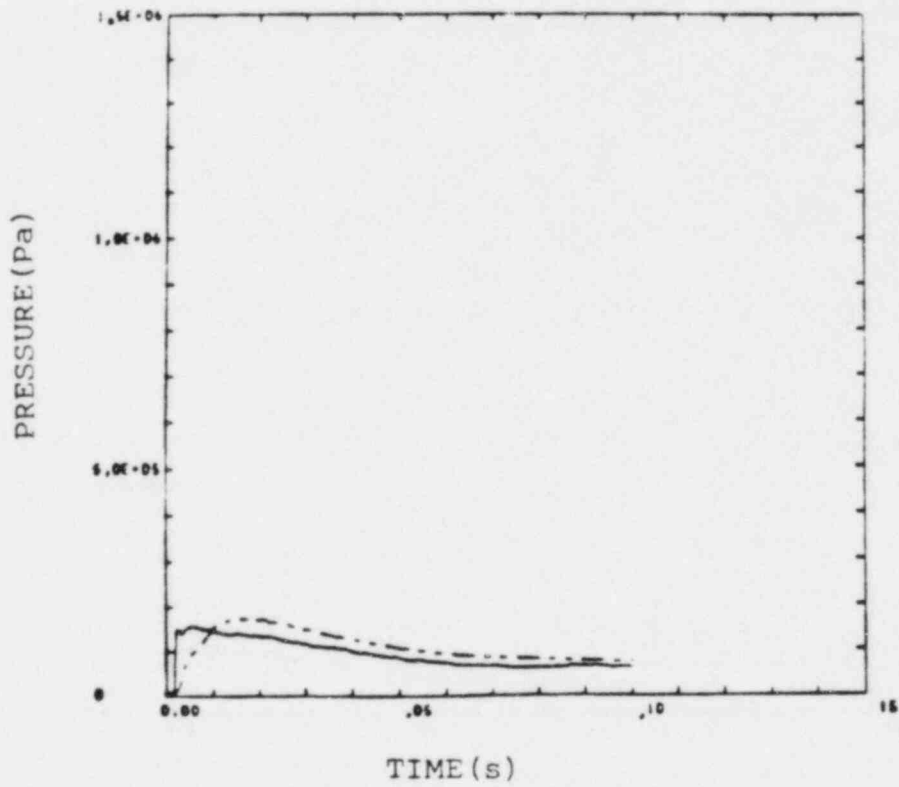


Fig. 52. Test 18, upper UCS pressure.

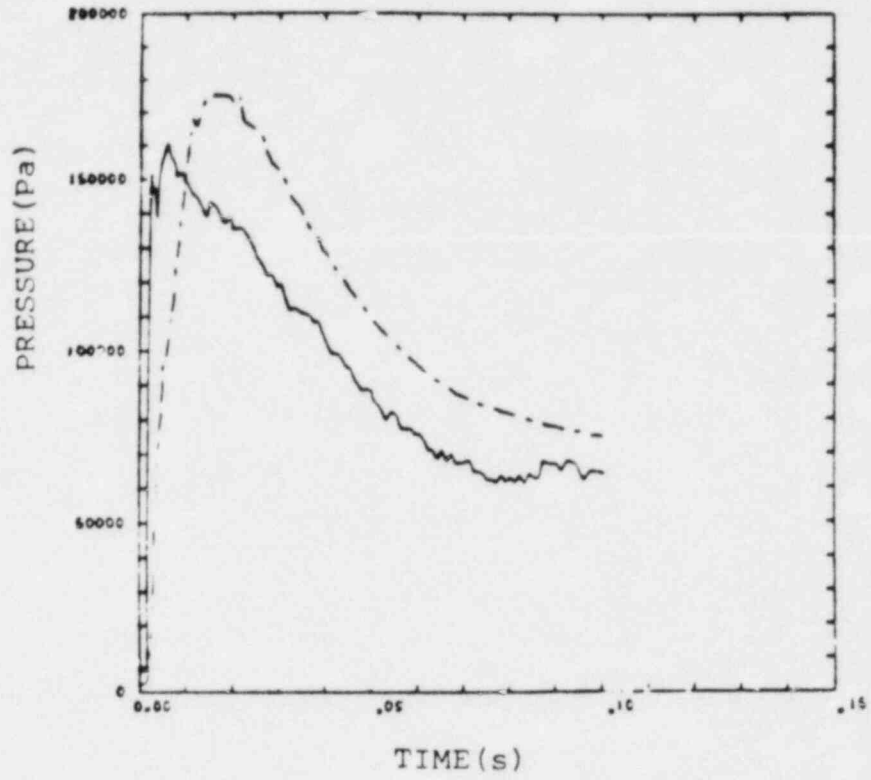


Fig. 53. Test 18, upper UCS pressure.

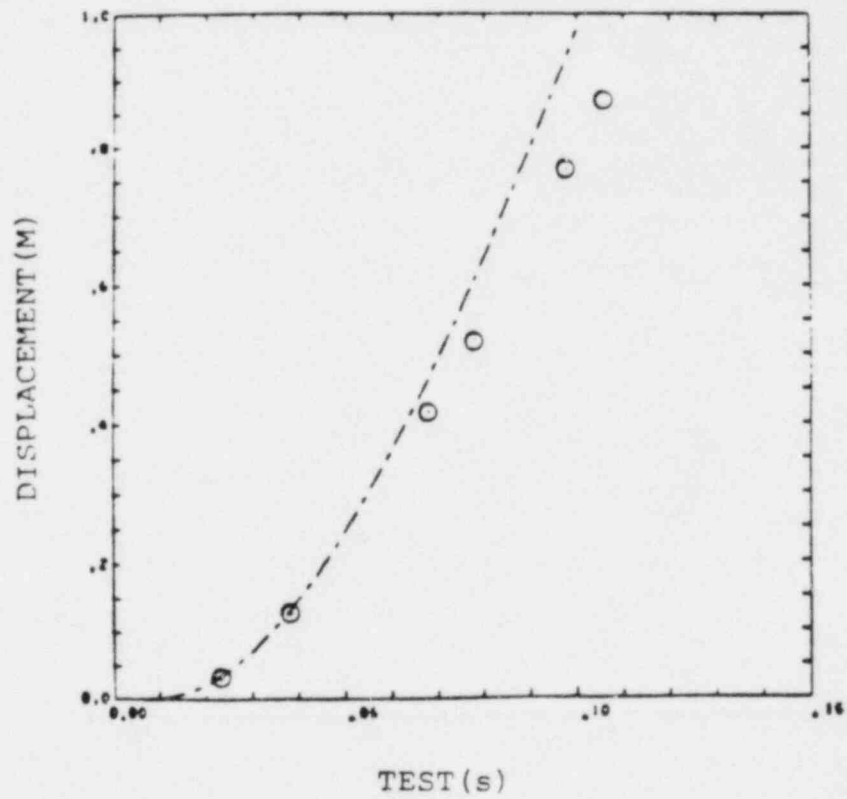


Fig. 54. Test 18, piston displacement.

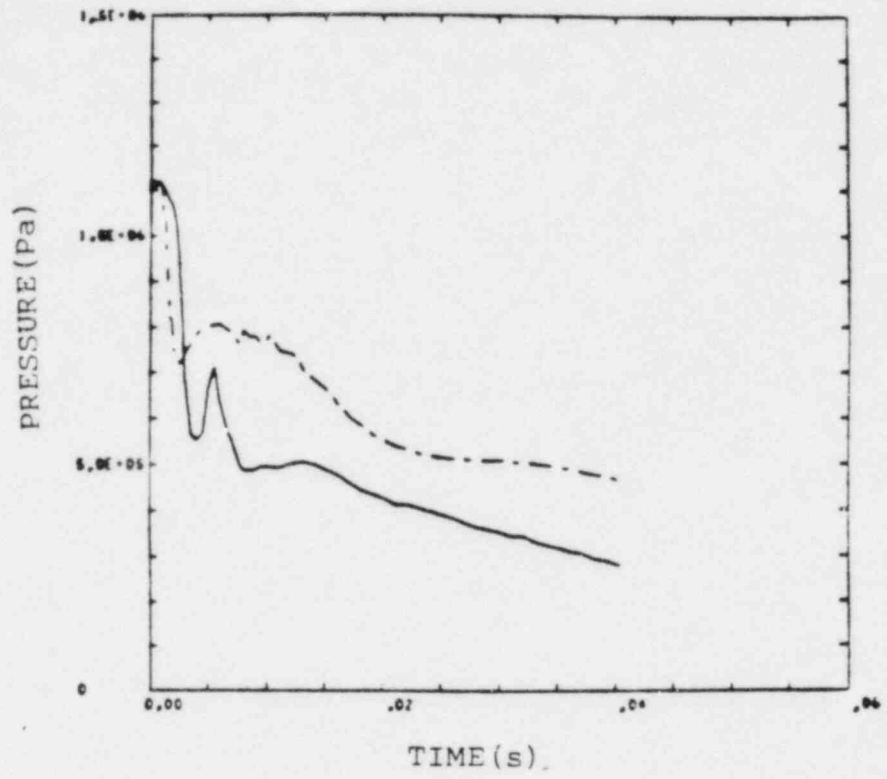


Fig. 55. Test 19, lower base pressure.

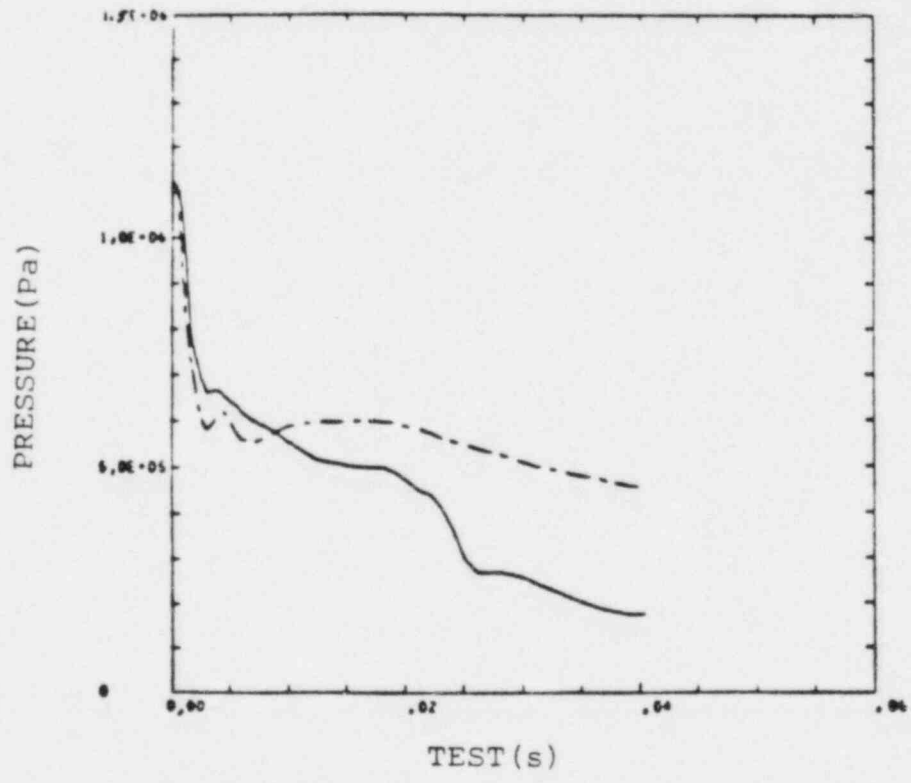


Fig. 56. Test 19, upper base pressure.

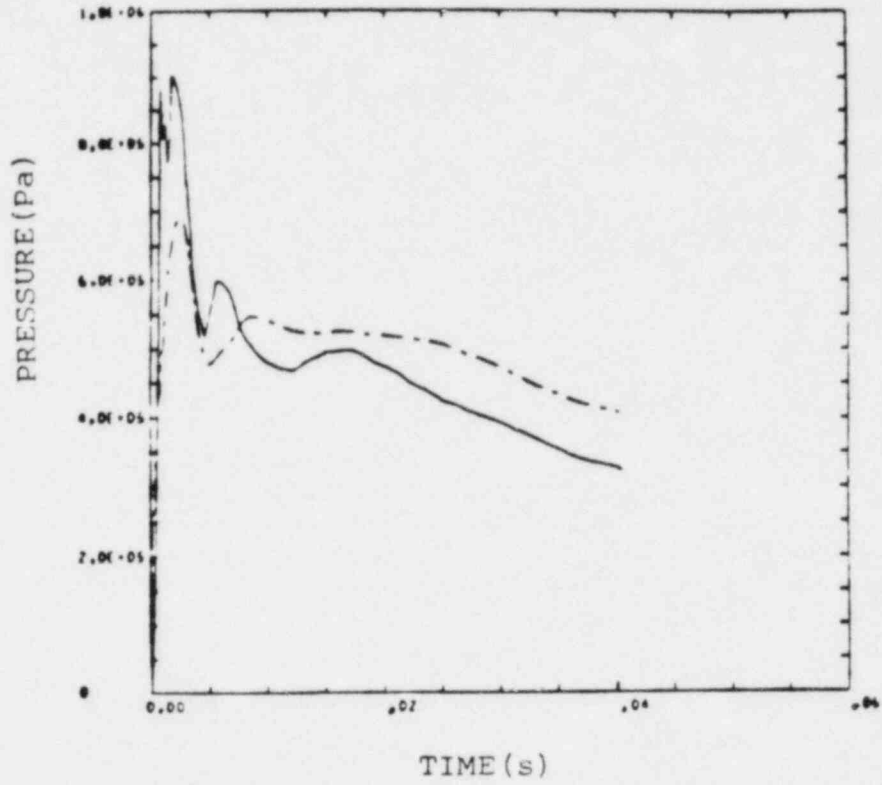


Fig. 57. Test 19, spacer pressure.

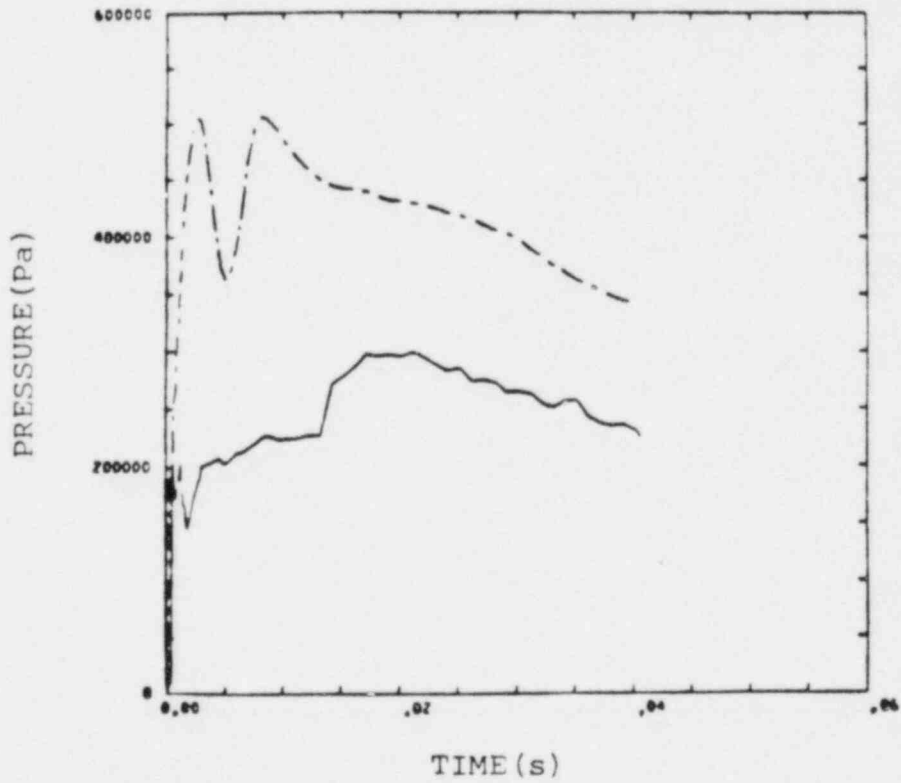


Fig. 58. Test 19, lower UCS pressure.

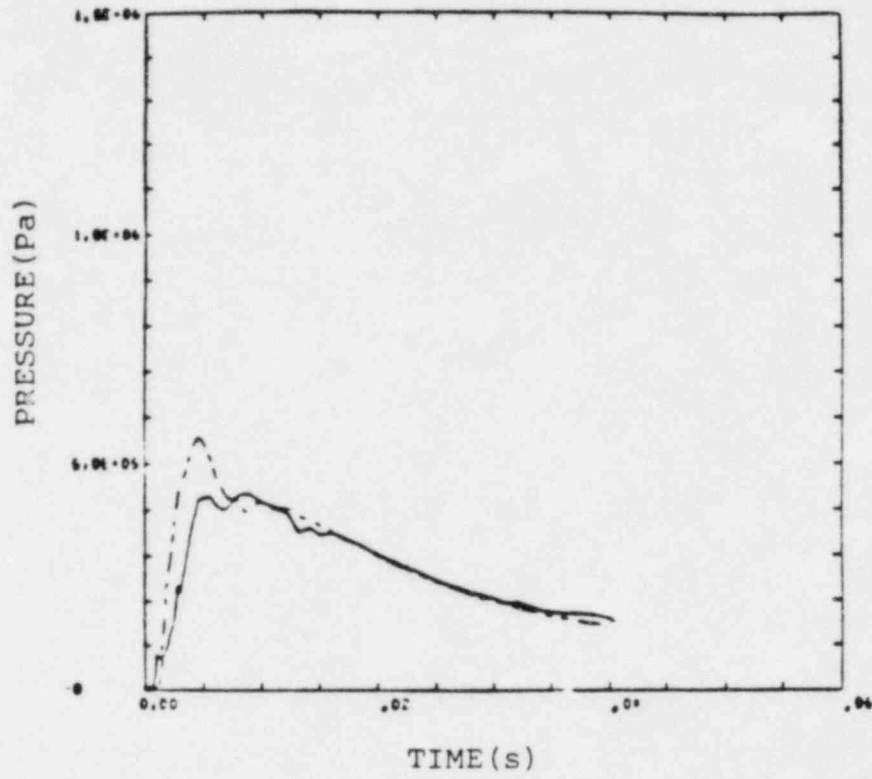


Fig. 59. Test 19, upper UCS pressure.

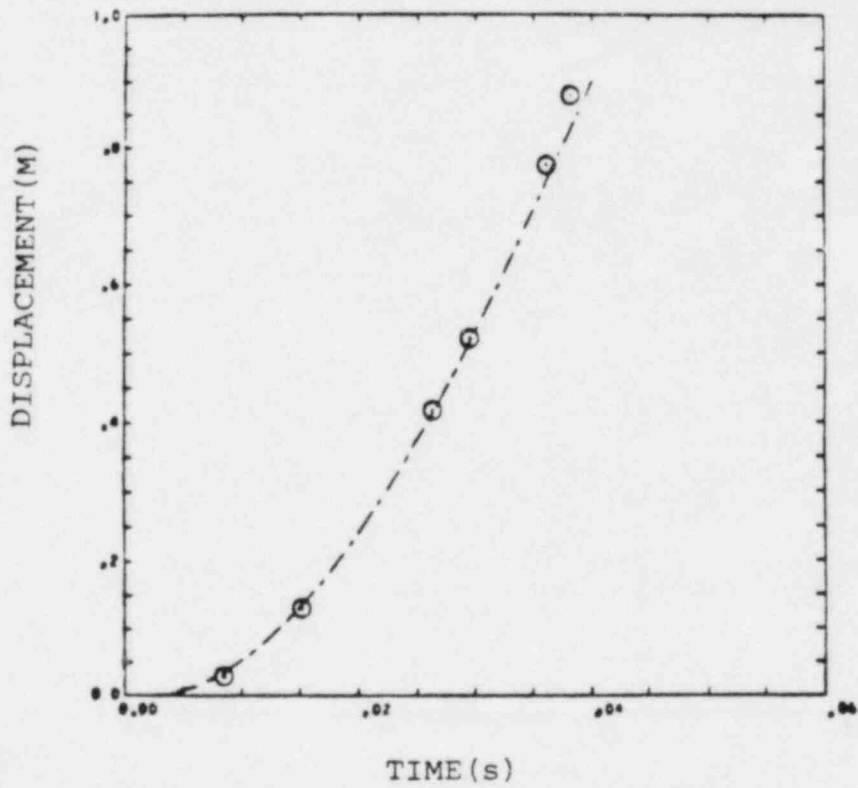


Fig. 60. Test 19, piston displacement.

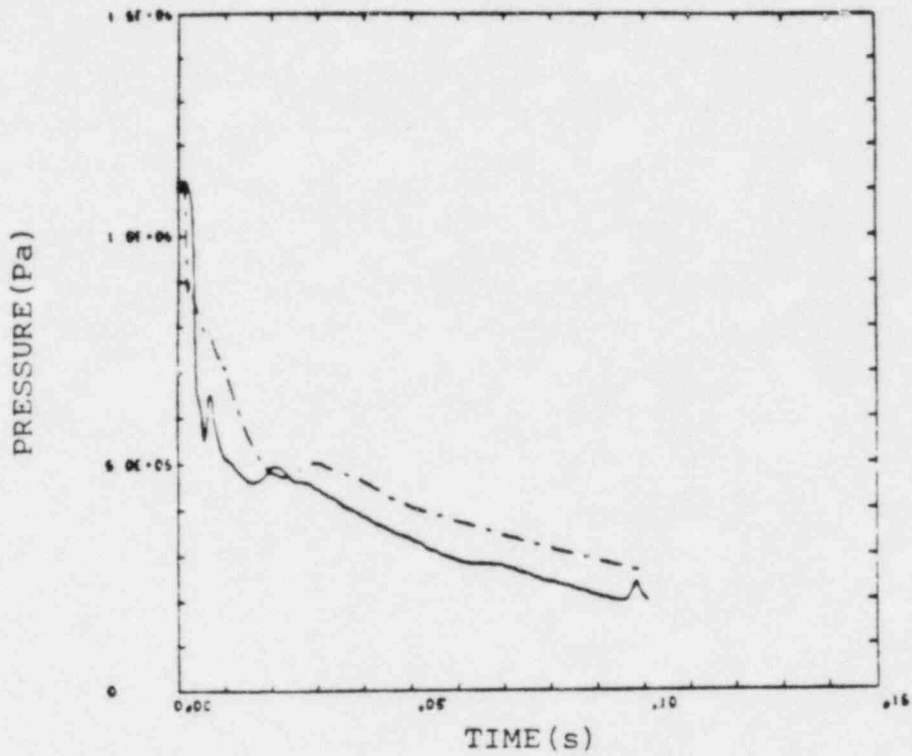


Fig. 61. Test 20, lower base pressure.

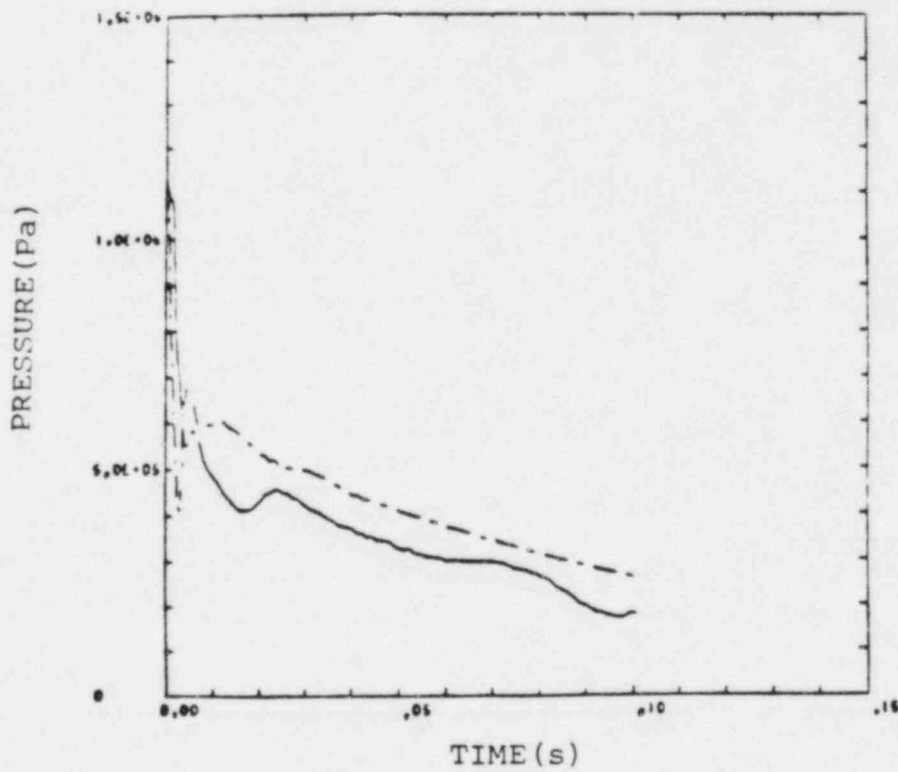


Fig. 62. Test 20, upper base pressure.

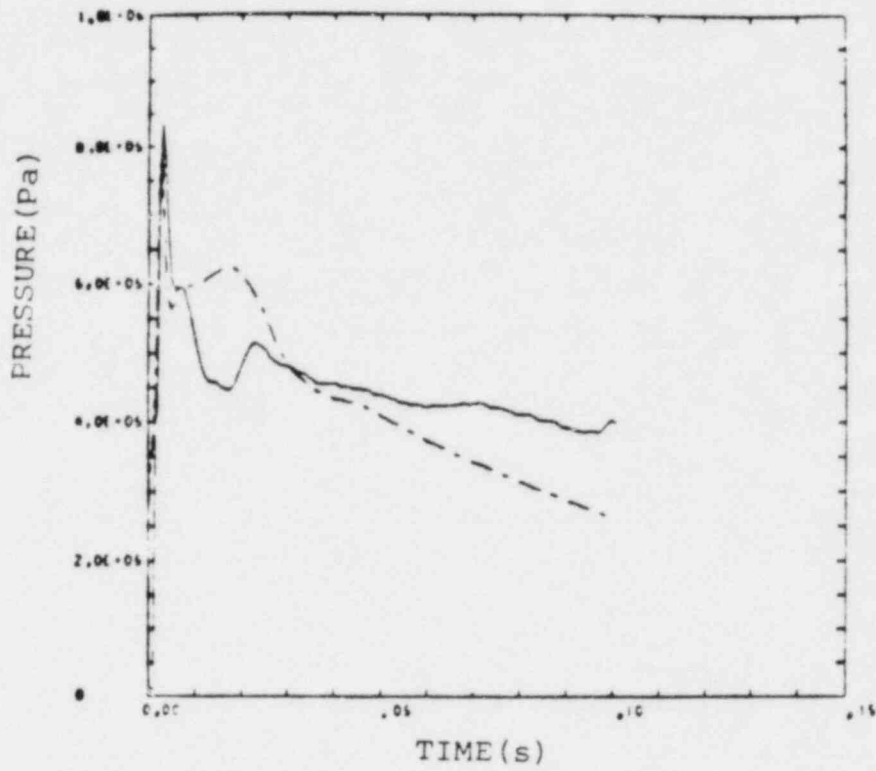


Fig. 63. Test 20, spacer pressure.

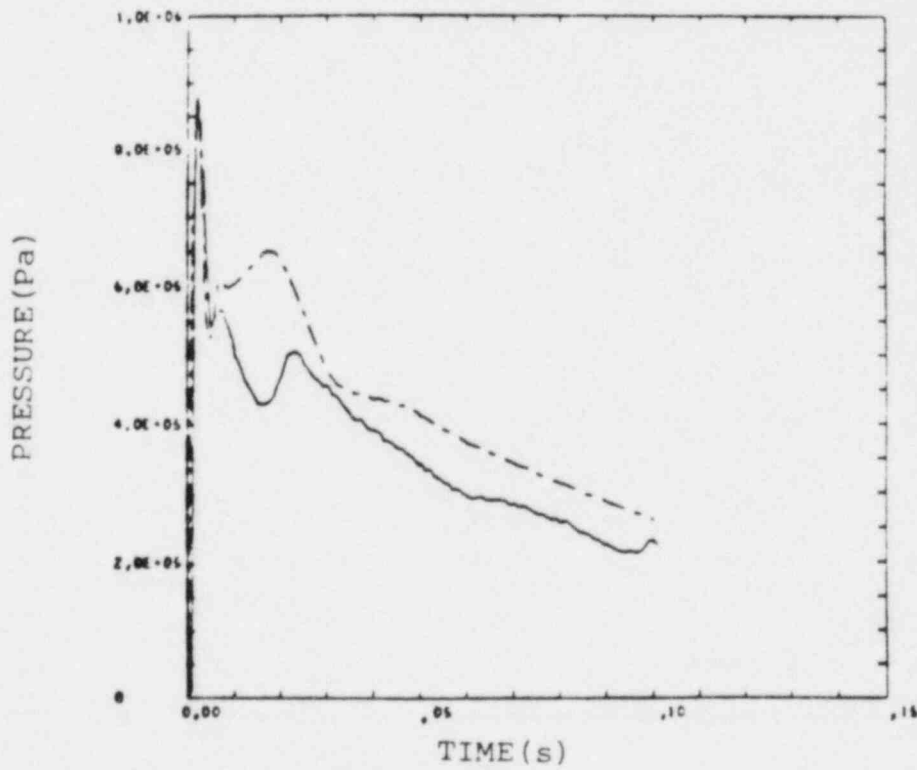


Fig. 64. Test 20, lower UCS pressure.

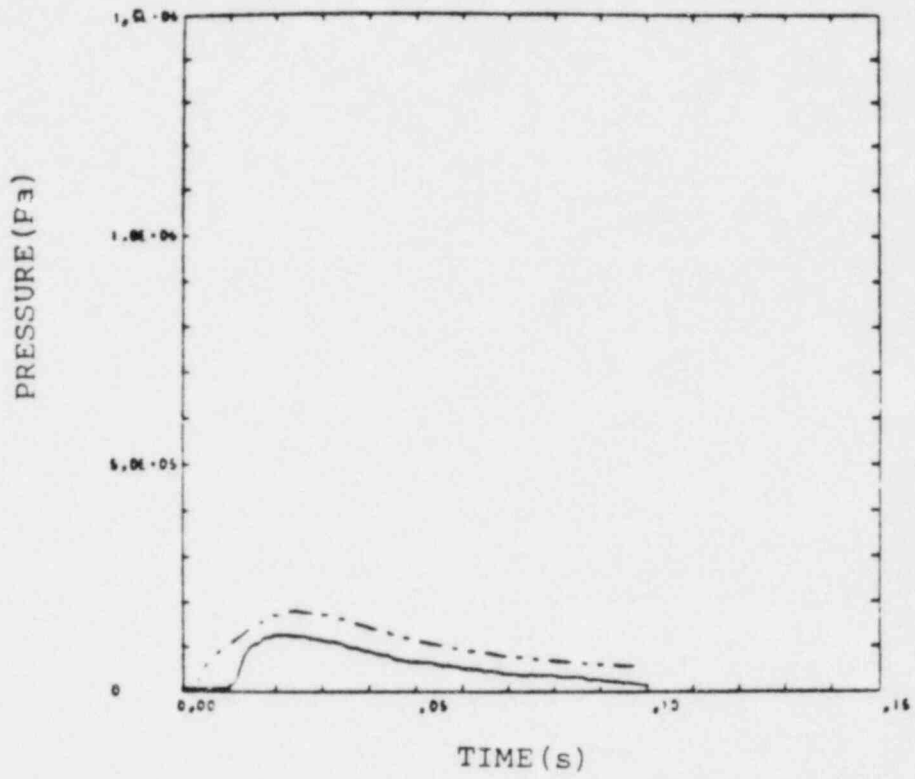


Fig. 65. Test 20, upper UCS pressure.

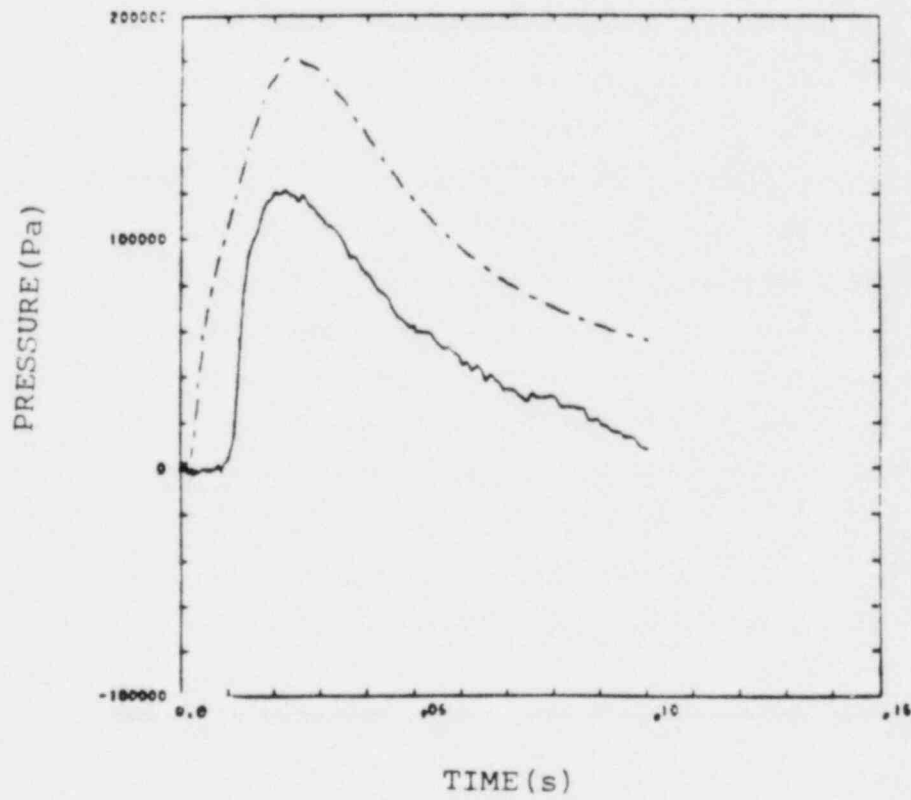


Fig. 66. Test 20, upper UCS pressure.

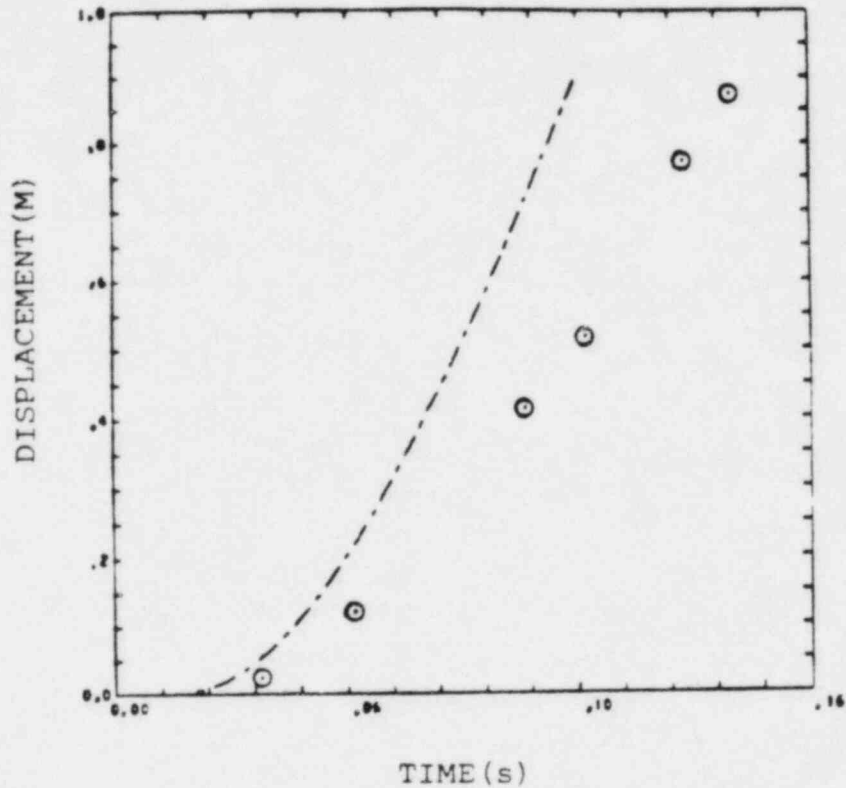


Fig. 67. Test 20, piston displacement.

Figure 22 shows the comparison of the lower base pressure transducer for test 13 processed by a 500 Hz, low-pass filter and the SIMMER calculation. Figure 21 shows the original pressure transducer readings with its strong oscillations. All other transducers indicate a clear signal. Both tests 12 and 13 give very similar pressure histories for the three UCS transducers (see Figs. 27 through 29). The lower UCS pressure in Fig. 27 is higher for test 12 between 5 and 30 ms, whereas both other transducers monitor nearly the same absolute values. The agreement is excellent for the upper UCS pressure (see Fig. 29). In both tests, the first pressure ramps are simultaneous. The second steep ramp, shown in Fig. 28, is delayed slightly for test 12. Time zero is determined by selection of an appropriate point of the digitized data. The spacer pressure transducer is closest to the rupture disk. Shortly after the opening, it reads a very strong pressure increase. The beginning of this pressure ramp can be identified with an accuracy of 0.5 ms. It defines the time zero for all tests presented here. For the UCS pressures, the base line (zero pressure) can be identified as the pretest steady-state value because this is only 3×10^3 Pa.

The input parameters for SIMMER calculations of tests 12 and 13 are the same except for the piston mass, which is 680 g for test 12 and 580 g for test 13. Figure 12 shows SIMMER calculations for the five mesh cells adjacent to the related pressure transducers. It shows that, after a vigorous transient flow during the first 10 ms, the pressure drops steadily according to the displacement of the piston. The first 10 ms are affected strongly by the reflection of the initial pressure pulse off the rigid interface of the piston. To consider the effect of the rigid interface, Figs. 13 and 14 show SIMMER calculations with the piston artificially fixed in the lowest and highest position (the highest position being at the downstream end of the test tube). Figures 12 and 13 are very similar for the first 10 ms because, for the moving piston, the displacement length is small. Figure 14 shows how differently the pressure wave reflection looks if the rigid interface is moved to the downstream end of the tube. This is especially true for the downstream pressure transducers. The pressures, shown in Fig. 12, gradually converge toward the residual level of Fig. 14. Differences occur mainly because of larger surfaces for the Fig. 14 calculations and, hence, a larger amount of energy transferred to the walls.

Analysis of the flashing source experiment, has shown deficiencies in SIMMER's simple evaporation/condensation model. The uniform droplet size and the constant Weber number criterion pose a limit on accuracy. Flashing starts with a pressure reduction in the liquid that travels from the top interface to the bottom. During this period, properties are continuously changing -- a situation that cannot be modeled accurately by the code. The simple evaporation/condensation model requires a uniform description within one parameter region, but the related physical phenomena change dramatically in time and space. The lower pressure transducer reveals a sharp decrease once the first density wave has passed (see Fig. 15). However, the pressure drop does not exceed 2×10^5 Pa because the pressure is also a function of the amount of propanol evaporated. This rapid pressure drop is an indication of nonequilibrium flashing. The nonequilibrium condition is due to the limited surface area available for evaporation. The larger the bubbles, the smaller the surface area, and the larger the degree of nonequilibrium. SIMMER, in addition to calculating droplet/bubble size using a Weber number, needs as input a maximum and a minimum droplet/bubble size. For the whole test series,

the maximum droplet/bubble size in the core was 10^{-3} m and the minimum was 3×10^{-5} m. The core liquid is defined initially so that a volume fraction was occupied by vapor and noncondensable gas. The vapor fraction, together with the bubble size, define the number of initial bubbles in the system. They are analogous to nucleation sites. The void fraction was varied frequently because neither the number of nucleation sites nor the effect of the vigorous transient during the first milliseconds is known. The larger the void fraction the longer it takes for the lower base pressure to recognize a pressure drop. This is caused by the drastic drop of the sound velocity in a two-phase medium as the vapor volume fraction increases. Thus, void fraction and bubble size govern both the response times and the instantaneous pressure drop. If the vapor fraction is large, the pressure drop can overshoot. This phenomenon has been observed in some upper base pressure records of the USD experiment (see Figs. 31 and 36).

As already noted for the helium tests, the turbulence is rather vigorous and three-dimensional disturbances have to be anticipated. The code cannot model sub-node turbulent-exchange processes. For the seven-hole and nineteen-hole arrays, a violent expansion leads to considerable nonuniformity over a cross section, enhanced dissipation and, above all, throttling (caused by fast-growing equilibrium with the downstream movement of the flashing liquid). A rather simple method has been chosen to adjust the SIMMER data to the experiment. Although the hydraulic diameter is invariable because of fixed geometry, it can be altered to increase friction and heat transfer. At the start of these calculations, this was the only parameter available for changing the friction term in the momentum equation separately in each parameter region. The hydraulic diameter can act as a multiplier because its inverse value is multiplied with the friction factor to yield the appropriate term in the momentum equation. For most times, the Reynolds number is high and the SIMMER friction factor is independent of the Reynolds number because it is fixed at its minimum of fully turbulent flow. Later, the code was changed to incorporate friction multipliers, which can be defined separately for each parameter region.

As the flow passes through the spacer region, condensation likely occurs at the walls. The spacer wall temperature is higher than room temperature because heat is conducted up through the walls from the core. For the whole

test series, the spacer wall temperature is 380 K. With the initial wall temperatures fixed, the condensation can be enhanced by increasing the inside-wall heat-transfer coefficient (see helium tests). Figure 16 shows the spacer pressure of test 12. In test 13, the transducer failed and no data can be reported. The calculation of spacer pressure reveals the highest discrepancy of the whole test because of the rather poor modeling of the fine structure of the flashing source. Downstream (see Figs. 17 through 19) code results are more consistent with the transducer readings.

From high-speed pictures taken during tests 14 and 17, the flashing appears complete at of the lower UCS pressure transducer. This could explain the poorly predicted spacer pressures, as much of the flashing process can be assumed to occur in and near the spacer. Recent results indicate that a model for variable liquid densities increases the spacer pressure accuracies. With the old model, however, there is no indication that the net result of the flashing process is calculated incorrectly. The upper UCS pressures in Fig. 19 agree very well. The deviations shown in Fig. 25 are partly a function of the lower piston mass of test 13, leading to an earlier expansion. There is no need to readjust the parameters of test 13 because the discrepancies shown in Fig. 25 are quite irrelevant. The average deviation for late times is 0.6×10^5 Pa. The time deviation also is at or below the anticipated value of 0.5 ms.

Test 17 (see Figs. 41 through 47) is the first transient with a low propanol core inventory. Instead of 559 cm^3 , 319 cm^3 of liquid propanol at room temperature was added to the system before closing and heating it. The instantaneous pressure drop caused by nonequilibrium flashing is larger for the small-inventory cases. The pressure decreases to 5.5×10^5 Pa.

Table V shows a comparison of the instantaneous pressure drop in tests 13 through 22. It shows that, for a given inventory, the drop is virtually independent of the kind of test section into which the fluid can expand. Tests 21 and 22 have been added although no SIMMER data are available for those experiments. The tests were divided into two groups, the high- and the low-inventory groups. Test 21 was a blowdown into an open 5-in. tube. The tube had virtually an infinite length. Only the instantaneous pressure drop was recorded for this test.

TABLE V

PRESSURE DROP AND IMPACT TIME RESULTS

<u>Test</u>	<u>Bundle</u>	<u>Initial Pressure (10⁵ Pa)</u>	<u>Pressure After Instantaneous Pressure Drop (10⁵ Pa)</u>	<u>Impact Time at 0.98 m (ms)</u>
13	7	11.2	9.0	35
14	7A	10.6	8.9	37
16	19	11.2	9.2	41
18	217	11.2	8.7	117
21	None	11.1	8.4	None
17	7A	10.6	5.6	38
19	19	11.2	6.7	40
20	217	11.2	5.7	144
22	7	11.0	6.5	35

For test 17, the same droplet limits were taken as for the high inventory cases, but initial conditions were chosen so that a substantially lower vapor fraction was achieved in the liquid propanol pool. As stated for Fig. 15, the decrease in void fraction increases the sound velocity in the liquid so that the code calculates a faster response of the lower base pressure. The response time of the upper base pressure (see Fig. 42) was no direct check for the validity of the code because the pressure transducer was placed at the end of a tube where the quality of the vapor was unknown. Figure 42 again reveals that the dissipational phenomena are not modeled to full satisfaction. However, the reflection waves in Fig. 43 are not smeared nor are they dissipated when penetrating into the UCS, which is obvious in Fig. 44. In Fig. 43, the peak at 3 ms is initiated by the step reduction in flow area at the lower UCS ending. These reflection phenomena are very well identified by the code. The reflection of the wave from the piston interface is recorded at 7 ms in Fig. 44, at 5 ms in Fig. 45, and at 2 ms in Fig. 46.

Test 18 (see Figs. 48 through 54) is the first successful test with the 217-pin bundle. The most obvious result is listed in Table V in the column "impact time." The figures in this column are used only inconsistently to give a qualitative picture because the mass of the piston is changed inconsistently in the code to yield the observed piston motion. Nevertheless, the impact time increases substantially from both the 7-hole and 19-hole bundles to the 217-pin bundle. The time scale is stretched, and rate-controlled phenomena will be more effective during longer periods. The second obvious point is the reduction in the upper UCS pressure, which is partly a function of those rate-controlled effects. To make this more visible, Fig. 52 is plotted on the same scale as Fig. 48.

Liquid films can be formed at the UCS wall, especially through condensation of hot propanol vapor at the cold walls. These films also can be formed under prototypic conditions.¹⁶ The condensation is a function of the balance of the heat fluxes into the wall and into the fluid at the wall/fluid interface. Although not considered in SIMMER, two dimensionless groups are important. The Fourier number is used in conjunction with transient heat conduction. Its prototypic value in a steel wall at 1400 K is 16000; for the steel pins in the experiment with a surface temperature of 290 K, it yields 1900. Thus, heat conduction is overemphasized in the experiment, but the scaled-down wall temperature is relatively high compared to prototypic conditions. The second dimensionless group is the ratio of fluid to wall heat conductivity. For prototypic uranium dioxide-vapor/steel, it yields 0.12; for propyl alcohol/steel, 0.012. More important, though, is that, with liquid films at the wall, energy will be transported first into the film and then, by different parameters, to the wall. Here, scaling of droplet entrainment from the film also might be important. Entrainment inception is proportional to the volumetric fluid flux, to the viscosity, to the inverse surface tension, and to the square root of the vapor-liquid density ratio. Proper modeling of the inception requires velocities reduced in scale from prototypic values by 34%. The basic scaling analysis yields 66% of the prototypic value, so entrainment can be overemphasized slightly.

The discrepancies of experimental and code results in Fig. 53 are not that substantial; this is because the pressure transducers of 15×10^5 Pa nominal pressure are not optimal for levels approaching 1.5×10^5 Pa, and because we

believe that an error of $\pm 7 \times 10^4$ Pa is reasonable. The selection of pressure transducers will be better adjusted to future experimental needs. In Fig. 49, the upper base pressure transducer did not work consistently because the rubber cap was partly stripped off its sensitive periphery. Thus, an incorrect signal resulted during the first 50 ms.

The calculation of test 19 (see Figs. 55 through 60) revealed substantial difficulties in predicting the near-core pressure histories. The vapor fraction of the liquid core section had to be reduced to increase the nonequilibrium pressure drop in the core. Recent analyses show that a new SIMMER model with variable liquid densities helps to decrease errors. Obviously, modeling deficiencies arise with the discontinuous specification of parameter regions, while fixed droplet conditions prevail inside a given region for a limited time only. As bubbles and droplets develop, they move into different places and are subject to different conditions. Furthermore, SIMMER neglects the fact that many kinds and sizes of bubbles and droplets coexist in the same area. SIMMER only takes a representative diameter and partly adjusts differences by lumped parameters. Test 20 (see Figs. 61 through 67) employed a 217-pin bundle with a low inventory of 319 cm^3 liquid propanol. Figure 61 shows that SIMMER first calculates an instantaneous lower base pressure drop (of $9 \times 10^5 \text{ Pa}$) similar to that shown in Fig. 48. The steep pressure gradient continues, however, and apparently some vapor is being produced already. The experiment exhibits no discontinuous inception of this phenomenon. For the upper base pressure (see Fig. 62), there is much better agreement for the steep pressure drop. The undershoot is a little bit too large, and late time pressures are greater for the SIMMER calculations. This continues up to the lower UCS pressure (see Fig. 64). Starting from this abnormally high pressure level, the upper UCS pressure (see Figs. 65 and 66) is always too high, although there has been a substantial pressure drop along the length of the UCS. The difference between experiment and calculation is about 5×10^4 Pa, as for test 18. The piston displacement (see Fig. 67) diverges considerably because the calculated upper UCS pressure is built up very fast, whereas there is a time lag in the experiment. In the calculation, there is too much propanol entering the UCS between 2 and 5 ms. The deviation is obvious in Fig. 63. Table VI shows the major SIMMER input parameters used for the propanol tests. As stated above, the droplet limits were held constant

TABLE VI

MAIN PARAMETER VARIATIONS OF THE PROPANOL TESTS

Test II	Bundle, see Table IV	Inventory (cm ³)	Initial core pressure (10 ⁵ Pa)	Initial core liquid temperature (K)	Initial helium density in the core (kg/m ³)	Initial propanol density in the core (kg/m ³)	Vapor fraction in the liquid core region (%)	Minimum void fraction for two-phase flow (%)	Core hydraulic diam (mm)	Spacer hydraulic diam (mm)	UCS hydraulic diam (mm)	UCS inside-wall heat-transfer coefficient (10 ⁴ Wm ⁻² K ⁻¹)	Orifice coefficient at UCS entrance	Piston mass (kg)	Pin-bundle friction multiplier
12	7	559	11.8	452	0.19	623	1.1	0.2	5	0.5	13	2	0.5	0.7	--
13	7	559	11.2	448	0.17	623	1.1	0.2	5	0.5	13	2	0.5	0.6	--
14	7A	559	10.6	448	0.17	623	1.1	0.2	5	50	13	2	0.5	0.7	--
16	19	559	11.2	448	0.17	623	1.1	0.2	5	0.5	8	0.7	0.5	0.9	--
17	7A	319	10.6	433	0.16	629	0.38	0.2	50	50	13	0.5	0.5	0.7	--
18	217	559	11.2	448	0.7	625	1.1	0.01	50	50	1	2	1	1.4	2
19	19	319	11.2	448	0.17	631	0.14	0.1	5	0.5	8	1.1	0.5	0.8	--
20	217	319	11.2	448	0.17	611	0.26	0.01	50	50	1	4	0	1.4	2

The following parameters are constant for the whole test series:

Spacer wall heat-transfer coefficient = $7.3 \times 10^4 \text{ Wm}^{-2} \text{ K}^{-1}$

Pin-bundle wall heat-transfer coefficient = $1.3 \times 10^4 \text{ Wm}^{-2} \text{ K}^{-1}$

Core minimum bubble/droplet diameter = $3 \times 10^{-2} \text{ mm}$

Core maximum bubble/droplet diameter = 1 mm

Spacer, minimum bubble/droplet diameter = $5 \times 10^{-4} \text{ mm}$

Spacer, maximum bubble/droplet diameter = 10^{-2} mm

UCS minimum bubble/droplet diameter = $5 \times 10^{-4} \text{ mm}$

UCS maximum bubble/droplet diameter = 10^{-2} mm

throughout the test series. The critical Weber number was 15 all the time. Although there were no friction multipliers available for the first tests, they were added for the 217-pin bundles. Limited only to the UCS, the friction factor was multiplied by this after its evaluation through SIMMER correlations. Table VI shows that, to choke the flow near the core, the hydraulic diameter had to be changed in an inconsistent manner. As stated above, the friction term is indirectly proportional to the hydraulic diameter. The hydraulic diameters of the UCS are true values. By specifying the helium density, the liquid temperature, and the liquid propanol density in the core, the vapor in the core and the initial core pressure are fixed. The core vapor fraction had to be decreased for the low inventory cases. The maximum void fraction is 79% because 21% was used for the wall volume fraction. The minimum void fraction for two-phase flow specifies that, below this value, SIMMER will anticipate single-phase conditions. This has an influence in that single-phase sound velocities, which are input parameters, then are used to calculate the variation of pressure with density. This not only increases the sound velocity but also limits the effect of coexisting vapor on the pressure. The orifice coefficient had virtually no effect on the results when using the listed values. The pressure drop across the orifice is formed by the orifice coefficient multiplied by the dynamic pressure of the flow.

An important parameter is the inside-wall heat-transfer coefficient, which is listed in Table VI for the UCS. If this value is large, heat easily can be transported from the wall/fluid interface into the wall. Hence, by increasing this parameter, the rate of condensation can be enhanced. A vigorous condensation process leads to lower local pressures and also decreases the UCS outlet pressures. For the 217-pin bundle of test 20, a high parameter value was necessary. The condensation processes could not be quantified consistently because of insufficient experiments. However, even with the crude phase-change models available in SIMMER, results are good enough to give a conservative estimate of the resultant pressures.

The piston mass is varied to achieve the appropriate upper boundary conditions. As stated above, no information was available about the friction forces; therefore, the piston mass had to be increased if it was to be slowed.

Figure 68 shows the upper UCS pressures of three tests as a function of the volume displaced by the piston during its travel up to the downstream end of the test section. The maximum piston displacement is 0.98 m with a displacement volume of 1900 cm^3 . Only the upper UCS pressure is recorded because it is the signal closest to the piston interface. Both SIMMER and test values are recorded. At the beginning of the transient, all pressures read $3 \times 10^3 \text{ Pa}$. Displacement data below 5 cm^3 are not reliable enough to justify any record. The pressures quickly reach high values after the first bulk of propanol has penetrated to the upper UCS. The pressures decrease during the expansion of the piston into the low-pressure ($3 \times 10^3 \text{ Pa}$) end of the test section. Curves are listed for test 12 with a 7-hole bundle and large hydraulic diameter and for tests 18 and 20 with the 217-pin bundle and small hydraulic diameter. The flow area in the UCS is always the same. For the 217-pin bundles, a substantial pressure reduction again is observed. For these tests, the pressures remain at a rather constant level for a long period. Quasi-steady-state conditions prevail most of the time so that the fluid continuously fills the volume that is opened by the receding piston. As stated above, there are greater relative differences between experimental and analytical results for tests 18 and 20. The absolute differences are comparable.

The integral over the pressure as a function of displacement volume yields the displacement work, which is transferred into mechanical work of the piston. Figure 69 shows both energies as a function of the displacement volume. Again, only tests 12, 18, and 20 are referred to. The displacement work is calculated using the pressure data of Fig. 68, and the kinetic energy of the piston is equivalent to half of the piston mass times the square of its velocity. As there are two pressure curves shown in Fig. 68, one using experimental and one using SIMMER data, there are two kinetic energy curves in Fig. 69 as well. Figure 69 shows that the final kinetic energy of test 12 (that is, the energy at the time of an anticipated slug impact of the sodium pool upon the vessel head) is about an order of magnitude higher than for the tests with the 217-pin bundle. The relative errors again are rather low for test 12. The SIMMER results are omitted for test 20 because they are similar to those of test 18. Figure 69 indicates that there might be substantial deviations from the logarithmic energy build-up for pin bundles. Further tests will improve the

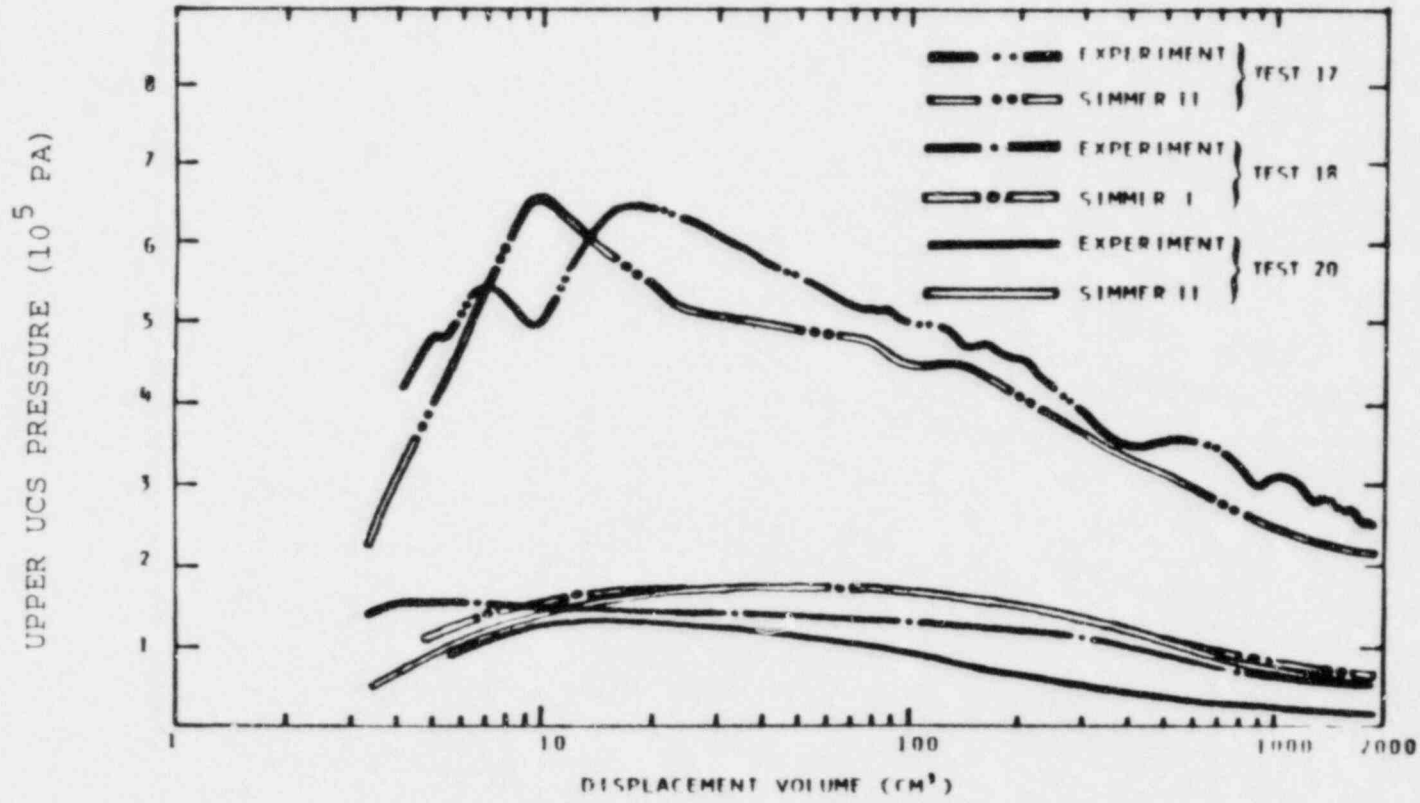


Fig. 68. Upper UCS pressure as a function of piston displacement volume.

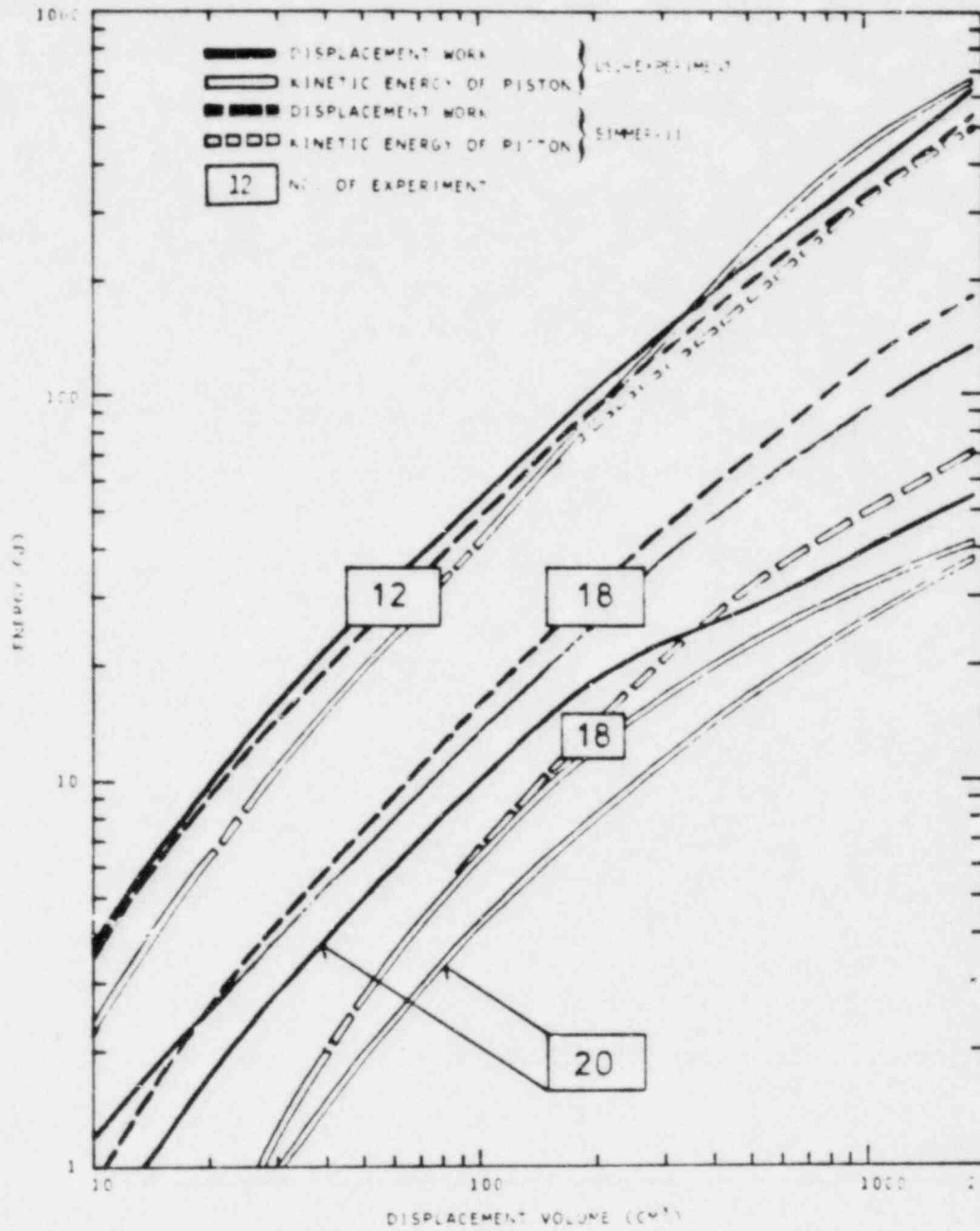


Fig. 69. USD energy-volume relationships.

accuracy of the experimental results so that we will have a confident data base for the work potential using a pin-bundle UCS.

VI. CONCLUSIONS

The motion pictures of tests 14 and 17 revealed that it is probable that most of the flashing had been completed before reaching the UCS. Recently, we have shown that the rupture disk opens even if the gas volume on top of the liquid propanol is small. Hence, substantially more flashing can be achieved within the pin structure. In the present test series, SIMMER lacks accuracy for modeling near-core flashing. This is evidenced by

1. too rough a droplet/bubble model with only one representative size,
2. lack of a dissipation model of sub-node, three-dimensional transient fluid flow, and
3. our inability to change parameter regions with time and space to adjust the parameters valid in these regions.

The modeling will apparently be improved by variable liquid densities in the code, by regionwise friction-factor and heat-transfer multipliers, and a separation of droplet size effects on momentum and energy equations. The modeling of the flow inside the UCS needs improvement owing to the lack of

1. a second liquid velocity field that can track liquid films sticking to the wall,
2. at least a two-node model inside the wall that can cope with a transient heat-up of the structures, and
3. an entrainment model that could be incorporated with a second liquid velocity field.

Thus to improve the accuracy of the calculations, some models need to be improved. However, with an extended experimental program, the present SIMMER version can yield reasonable results providing that input parameters are adjusted properly. The present test series shows that

1. SIMMER-II calculations usually were within the band of uncertainty that is imposed by the signal pick-up, acquisition, and recording systems;

2. the adjustment of SIMMER parameters could be performed consistently for nearly all cases;
3. the identification of inconsistent parameters could be related to singular deficiencies in modeling; and
4. the transients for the 217-pin bundle revealed conservative SIMMER results.

The simplicity of the present models makes it feasible to check most of the parameters for usefulness in prototypic calculations. SIMMER analyses of an extended experimental program can help generate an accurate data base for prototypic calculations. To this end, this report contributes the first step.

VII. ACKNOWLEDGEMENTS

The authors acknowledge the assistance of the following Los Alamos personnel: R. Rochester and G. Gray, Group WX-7, for their help in constructing the rupture-disk breaking mechanism; R. Baca, Group Q-8, for his help in the design and fabrication of the experimental hardware; R. Christensen and J. Perea, Group WX-10, for their continuing assistance in data handling and recording; and S. L. Gray and A. B. Chavez for typing this report.

REFERENCES

1. J. E. Boudreau and J. F. Jackson, "Recriticality Considerations in LMFBR Accidents," Proc. Fast Reactor Safety Meeting, CONF-740401 (Beverly Hills, California, April 2-4, 1974).
2. D. W. Ploeger and D. J. Cagliostro, "Development and Characterization of a Liquid-Vapor Bubble Source for Modeling HCDA Bubbles," Stanford Research Institute Technical Report 2, Project PVU-3929 (March 1977).
3. T. G. Theofanous and D. Christopher, "The Termination Phase of Core Disruptive Accidents in LMFBRs," School of Nuclear Engineering, Purdue University report PNE-78-126 (February 1978).
4. J. E. Boudreau and L. L. Smith, "Transport Processes in LMFBR Core Disruptive Accidents," INKA-CONF 294-003, 1978.
5. R. Fröhlich, P. Royl, P. Schmuck, R. Dusing, and M. Senglaub, "Analyse Schwerer Hypothetischer Storfälle für den SNR-300 Mark 1A Reaktorkern," KFK 2310, 1976.
6. W. R. Bohl, "Some Recriticality Studies with SIMMER-II," Proceedings of the Int. Meeting on Fast Reactor Safety Technology, (Seattle, Washington, August 19-23, 1979).

7. E. J. Chapyak and V. S. Starkovich, "The Role of Similitude in the Design of LMFBR Safety-Related Simulation Experiments," International Meeting on Fast Reactor Safety and Technology (Seattle, Washington, August 19-23, 1979).
8. A. J. Suo-Antilla, "Analysis of Postdisassembly Expansion Experiments," Proceedings of the Int. Meeting on Fast Reactor Safety Technology, (Seattle, Washington, August 19-23, 1979).
9. A. J. Suo-Antilla, "SIMMER Analysis of the Purdue-Omega Experiments," Los Alamos Scientific Laboratory document LA-UR-80-65.
10. J. F. Jackson and M. G. Stevenson, Compilers, "Nuclear Reactor Safety, January 1-March 31, 1978," Los Alamos Scientific Laboratory report LA-7278-PR (June 1978), p. 69.
11. J. F. Jackson and M. G. Stevenson, Compilers, "Nuclear Reactor Safety, January 1-March 31, 1978," Los Alamos Scientific Laboratory report LA-7278-PR (June 1978), p. 67.
12. J. F. Jackson and M. G. Stevenson, Compilers, "Nuclear Reactor Safety Progress Report, April 1-June 30, 1978," Los Alamos Scientific Laboratory report LA-7481-PR (October 1978), p. 58.
13. J. H. Scott, "Experimental Verification of SIMMER Computer Code," Los Alamos Scientific Laboratory document LASL-79-61 (July 1979).
14. C. R. Bell, R. D. Burns, and L. B. Luck, "Impact of SIMMER-II Model Uncertainties on Predicted Postdisassembly Dynamics," Los Alamos Scientific Laboratory report LA-8053-MS (October 1979).
15. C. R. Bell, "Modification of SIMMER-II for Material Tracking Into the Reactor Containment Building During Postdisassembly Expansion," (to be published).
16. D. Wilhelm, "A Brief Analysis of the Transient Flow at the Entrance of the Upper Core Structure During a Hypothetical Core Expansion," Los Alamos National Laboratory report LA-8806-MS (April 1981).

DISTRIBUTION

Nuclear Regulatory Commission, R7, Bethesda, Maryland	273
Technical Information Center, Oak Ridge, Tennessee	2
Los Alamos National Laboratory, Los Alamos, New Mexico	<u>50</u>
	325

120555078877 L ANR7
US NRC
ADM DIV OF TIDC
POLICY & PUBLICATIONS MGT BR
PDR NUREG COPY
LA 212
WASHINGTON DC 20555

Los Alamos